https://doi.org/10.5194/egusphere-2026-6926
Preprint. Discussion started: 20 November 2026
© Author(s) 2026. CC BY 4.0 License.

Successional stages of methane seep systems off central Chile: linking active sediment-hosted seepage with long-lived carbonate chemoherms

Tina Treude[1], Peter Linke[2], Volker Liebetrau[2†], Florian Scholz[3], Philip Steeb[2], Jacob Geersen[4], Mark Schmidt[2], Stefan Sommer[2], Lorenzo Rovelli[5], Lee Bryant[6], and Jan Scholten[7]

[1]University of California - Los Angeles, Earth, Planetary, and Space Science, Los Angeles, United States
[2]GEOMAR Helmholtz Centre for Ocean Research, Kiel, Germany
[3]Universität Hamburg, Department of Earth System Sciences, Hamburg, Germany
[4]Leibniz Institute for Baltic Sea Research Warnemünde, Rostock, Germany
[5]Federal Institute of Hydrology, Koblenz, Germany
[6]University of Bath, Climate Adaptation and Environment Research (CAER) Centre, Bath, UK
[7]Institute of Geosciences, Kiel University, Germany

Correspondence to: Tina Treude (ttreude@g.ucla.edu) and Peter Linke (plinke@geomar.de)
[†]Deceased

https://doi.org/10.5194/egusphere-2026-6926
Preprint. Discussion started: 20 November 2026
© Author(s) 2026. CC BY 4.0 License.



Abstract. Methane seeps along continental margins support chemosynthetic ecosystems and promote the formation of authigenic carbonates that provide persistent habitats for deep-sea organisms. These ecosystems evolve as methane supply, fluid pathways, and associated biogeochemical processes change over time. However, the relationships between seep development, methane cycling, carbonate formation, and benthic community succession remain poorly constrained. Here, we investigated the Concepción Methane Seep Area off the coast of central Chile to examine seep habitats representing different stages of ecosystem development. We combined seafloor observations, sediment and water-column geochemistry, measurements of microbial methane oxidation and sulfate reduction rates, benthic oxygen fluxes, and mineralogical, stable isotope, and uranium-thorium analyses of authigenic carbonates across five seep areas. The investigated habitats represented different stages of seep succession, ranging from young, sediment-dominated systems with sulfur-oxidizing bacterial mats to mature and senescent habitats characterized by extensive carbonate structures, declining chemosynthetic communities, and diverse non-chemosynthetic fauna. Chemosynthetic communities included sulfur-oxidizing bacterial mats, vesicomyid clams, and Lamellibrachid and frenulate tubeworms. Comparisons of methane oxidation and sulfate reduction rates revealed distinct relationships between microbial processes and benthic habitats. Methane oxidation beneath bacterial mats and clam fields was generally associated with sulfate reduction, consistent with sulfate-dependent anaerobic oxidation of methane (AOM). In contrast, methane oxidation in tubeworm-colonized sediments was largely decoupled from sulfate reduction, suggesting a greater contribution of aerobic methane oxidation. Methane-driven microbial activity varied substantially among habitats. Particularly striking was a dead clam field characterized by dense accumulations of predominantly empty shells, indicating the disappearance of a formerly established chemosymbiotic community. Despite the apparent loss of living clams, the underlying sediments exhibited the highest measured rates of AOM (up to 856 nmol cm^{-3} d^{-1}) and sulfate reduction (up to 1946 nmol cm^{-3} d^{-1}). This contrast suggests that the visible benthic community retain the ecological signature of past seep conditions rather than contemporary activity. One hypothetical explanation is a recent change in methane supply associated with tectonically induced modifications of subsurface fluid pathways, potentially linked to the 2010 Maule earthquake. Elevated methane concentrations immediately above several seep habitats further indicated that methane locally escaped the benthic microbial filter and entered the water column. Authigenic carbonates recorded prolonged and episodic seepage, with uranium-thorium ages ranging from approximately 5,000 to more than 100,000 years, although some samples yielding older ages showed evidence of open-system behavior. Carbonate abundance, morphology, and associated communities broadly reflected the inferred successional stages. However, localized evidence of active seepage persisted even within advanced senescent habitats, and no clearly extinct seep ecosystem was identified. These observations suggest that seep succession is not necessarily unidirectional, as changes in

https://doi.org/10.5194/egusphere-2026-6926
Preprint. Discussion started: 20 November 2026
© Author(s) 2026. CC BY 4.0 License.

subsurface fluid pathways may reactivate seepage and redirect ecosystem development. Beyond supporting chemosynthetic communities, seep-generated carbonate structures provide persistent hard substrates, refuges, and nursery habitats for diverse deep-sea organisms. Our findings demonstrate that Concepción methane seeps represent dynamic mosaics of different successional stages, shaped by the interplay of tectonically induced fluid flow, microbial processes, carbonate formation, and ecosystem development.

https://doi.org/10.5194/egusphere-2026-6926
Preprint. Discussion started: 20 November 2026
© Author(s) 2026. CC BY 4.0 License.

1. Introduction

Cold seeps are widespread features of continental margins worldwide, where fluids enriched in methane and other dissolved constituents migrate from the subsurface to the seafloor, sustaining unique chemosynthesis-based ecosystems and driving extensive biogeochemical transformations (Paull et al., 1984; Suess, 2010; Suess, 2014; Levin, 2005). A key process at methane seeps is the anaerobic oxidation of methane (AOM), mediated by consortia of anaerobic methanotrophic archaea (ANME) and sulfate-reducing bacteria, which couple methane oxidation to sulfate reduction (Boetius et al., 2000; Treude et al., 2003; Orphan et al., 2001; Knittel and Boetius, 2009). The produced hydrogen sulfide fuels chemosynthesis-based microbial and faunal communities (Sahling et al., 2002; Levin, 2005), while the released bicarbonate increases porewater alkalinity and promotes the precipitation of methane-derived authigenic carbonates (Greinert et al., 2001; Bohrmann et al., 1998; Peckmann et al., 2001; Luff and Wallmann, 2003). Over geological time scales, continued carbonate precipitation can give rise to extensive carbonate hardgrounds and chemoherm structures that archive the history of seep activity.

Along active continental margins, seep location and activity are mainly controlled by a complex interplay of tectonic faulting and fluid flow, with implications for biogeochemical cycling and benthic ecosystems (Suess, 2020). The Concepción Methane Seep Area (CMSA; ~36° S) lies within the Central Chilean accretionary forearc, a tectonically active segment where the Nazca Plate subducts beneath South America at ~6.6 cm yr^{-1} (Angermann et al., 1999). Its internal structure and seafloor geomorphology are shaped by a network of thrust and normal faults, submarine landslides, and canyon systems that transport Andean sediments toward the trench (Geersen et al., 2011; Melnick and Echtler, 2006; Völker et al., 2011). The faults create intraslope basins and facilitate fluid migration from deeper strata to the seafloor, promoting focused seepage.

Episodic deformation associated with major subduction earthquakes—such as the 1835 Concepcion, 1960 Valdivia, and 2010 Maule events—reactivated some of the faults in the marine fore arc, thereby governing transient fluid-flow processes (Geersen et al., 2016; Völker et al., 2011). Bottom-simulating reflector (BSR)–derived heat-flow data generally match conductive models; however, measured surface heat flow locally triples landward of the prism backstop, implying episodic upward flow of deeper-sourced fluids through the gas-hydrate stability zone (Grevemeyer et al., 2006). These anomalies have been interpreted as post-seismic pulses of fluid release following large underthrust earthquakes, temporarily disturbing the hydrate system. Direct evidence for the interplay between faulting and fluid flow came from observations after the 2010 Maule earthquake. Within the rupture area, new sites of active methane seepage were documented about seven months after the earthquake, while coulomb stress modeling suggests that underlying upper-plate faults have been reactivated during the earthquake, enabling the ascent of hydrocarbon-bearing fluids (Geersen et al., 2016). Repeated

https://doi.org/10.5194/egusphere-2026-6926
Preprint. Discussion started: 20 November 2026
© Author(s) 2026. CC BY 4.0 License.

reactivation of these faults by large subduction-zone earthquakes, which have a recurrence rate of 100-150 years in the area, likely governs the timing and spatial pattern of seepage along the central Chile margin.

High-resolution multibeam bathymetric and sidescan sonar surveys between ~600 and 1,000 m water depth revealed extensive areas of elevated acoustic backscatter, often associated with pockmarks, mounds, and ridges interpreted as sites of past or present seepage (Klaucke et al., 2012). Video sled and remotely operated vehicle (ROV) observations during the R/V SONNE cruise SO210 (ChiFlux) confirmed widespread authigenic carbonate pavements and chemoherm buildups (Linke, 2011; Treude et al., 2011).

The CMSA supports diverse chemosymbiotic communities typical of reducing habitats. Vesicomyid, lucinid, solemyid, and thyasirid bivalves dominate soft-sediment seeps, while siboglinid tubeworms (*Lamellibrachia* sp.) and epifaunal gastropods and polychaetes colonize carbonate surfaces (Sellanes et al., 2008; Quiroga and Sellanes, 2009). Several new species and genera have been described from this region, reflecting both endemism and faunal links to other Southeast Pacific seep provinces. These organisms rely on bacterial endosymbionts that oxidize methane or sulfide, coupling local biogeochemistry to primary production independent of photosynthesis.

Seep carbonates and surrounding sediments host over 100 megafaunal taxa, including numerous non-seep species that exploit the structural complexity and hard substrate provided by authigenic carbonates (Sellanes et al., 2008; Treude et al., 2011). Stable-isotope analyses reveal a mixed trophic system: while ~88 % of consumers derive most of their carbon from photosynthetic detritus, at least 22 taxa incorporate methane-derived carbon into their biomass (Zapata-Hernández et al., 2014). Methanotrophy and thiotrophy thus extend their influence beyond obligate symbionts to a wider array of deposit and suspension feeders. The coexistence of chemosynthetic and heterotrophic pathways highlights the strong coupling between seep processes and the productive upwelling ecosystem of central Chile.

The CMSA provides a unique opportunity to investigate the interplay between tectonic activity, fluid flow, methane cycling, carbonate formation, and benthic ecosystem development along an active continental margin. Here, we present extensive, interdisciplinary datasets collected within the CMSA during R/V SONNE cruise SO210 (21.09. - 01.11.2010), which reveal how the CMSA comprises seep systems at different stages of development, ranging from young, sediment-hosted seepage with sulfur-oxidizing bacterial mats to carbonate-dominated chemoherms characterized by diminished seepage and extensive colonization by background deep-sea fauna. We demonstrate that carbonate ages span from <5 ka to >100 ka, documenting long-lived and multi-phase seep activity, while sediment and water-column geochemistry reveal strong spatial variability in methane fluxes linked to focused fluid flow and seafloor

https://doi.org/10.5194/egusphere-2026-6926
Preprint. Discussion started: 20 November 2026
© Author(s) 2026. CC BY 4.0 License.

disturbance. Our results further suggest that episodic tectonic activity influences seep dynamics, promoting localized methane release, carbonate precipitation, and shifts in benthic community structure. Together, these findings establish the CMSA as a natural laboratory for studying the coupled evolution of tectonic processes, methane seepage, carbonate growth, and deep-sea ecosystems.

https://doi.org/10.5194/egusphere-2026-6926
Preprint. Discussion started: 20 November 2026
© Author(s) 2026. CC BY 4.0 License.

2. Materials and Methods

2.1 Study Areas

Based on historical data paired with data obtained during the SO201 expedition in Sept – October 2010 within the CMSA region (~36° S), we focused on five key study areas based on geophysical evidence for seepage activity, subsurface gas accumulations, and authigenic carbonate buildups (Fig. 1). These areas are referred to throughout this study as Box-1, Box-2, Box-3, Box-4, and Box-8, and are complemented by a CMSA reference site that showed no geophysical indications of seepage. In the following descriptions, these areas are characterized based on the information available prior to this study and from video surveys conducted during the SO210 expedition. Bathymetric and backscatter maps of the respective areas (excluding the reference site) are presented in Figs. 2 and 3, respectively.

All boxes are located within the Concepción–Constitución seismotectonic segment, that was ruptured during the 2010 Maule earthquake (Moreno et al., 2010), as well as during previous large subduction earthquakes, that are known to affect the study area every 100-150 years on historical timescales (Lomnitz, 2004). Along the entire margin segment, scarps and subtle slump features indicate gravitationally driven sediment transport and mass wasting processes that expose older sedimentary strata at the seafloor. The multiple slide systems may point towards a link between slope instability and fluid flow in the marine forearc (Völker et al., 2011; Völker et al., 2009).

Boxes 1, 2, 4 and 8 locate in the vicinity – but at different distances - to the seafloor outcrops of a large upper-plate normal fault system. The normal faults were possibly activated during the co-seismic phase of the 2010 Maule earthquake (Geersen et al., 2016), as well as during previous large subduction zone earthquakes. Upper plate faulting has created local accommodation space for slope sediments that cover the underlying framework rock of the upper plate.

Box-3 in contrast, is located adjacent to a series of thrust ridges that represent the surface outcrops of large upper plate splay faults. Lieser et al. (2014) suggested that the splay faults were activated by the 2010 Maule earthquake. Landward (eastwards) of the thrust ridges, a sediment filled slop basin has been documented based on seismic data (Geersen et al., 2011). The Box is located near the transition between the young, active accretionary prism and the Mesozoic framework rocks of the upper plate.

2.1.1 Box-1 (≈660–700 m water depth)

Regional sidescan sonar mosaics in Box-1 revealed extensive high-backscatter areas, hundreds of meters in width, forming irregular ridges and domes indicative of carbonate hardgrounds and chemoherms rather than soft sediments (Klaucke et al., 2012) (Fig. 3). Video surveys during the SO210 expedition showed extensive exposed carbonate hardgrounds with only a thin sediment veneer (Linke, 2011).

https://doi.org/10.5194/egusphere-2026-6926
Preprint. Discussion started: 20 November 2026
© Author(s) 2026. CC BY 4.0 License.

2.1.2 Box-2 (≈690–705 m water depth)

Sidescan sonar imagery in Box-2 revealed elongated to ellipsoidal high-backscatter patches embedded within a predominantly soft-sediment seafloor, suggesting the presence of shallow carbonates and/or gas-charged sediments (Fig. 3). Video surveys confirmed a largely sediment-covered habitat characterized by patchy sulfur-oxidizing bacterial mats, black patches of reduced sediment, and only minor carbonate exposures (Linke, 2011). The concentration of backscatter anomalies along basin margins is consistent with the regional distribution of cold seeps off central Chile, where seepage preferentially occurs at the edges of intraslope basins rather than on ridge crests (Klaucke et al., 2012).

2.1.3 Box-3 (≈900–1,010 m water depth)

Sidescan sonar, backscatter data, and video surveys reveal extensive exposures of layered authigenic carbonates forming high-backscatter ridges and hardgrounds (Fig. 3), while active seepage is restricted to localized patches of chemosynthetic communities associated with fractures and ridge crests (Linke, 2011). More broadly, the upper-slope seep belt (600–1,000 m water depth) contains far more carbonate outcrop than active seep habitats, suggesting that fluid flow was more widespread or intense in the past. Box-3 reflects this pattern, with extensive fossil chemoherms interspersed with relatively small areas of ongoing seep activity (Klaucke et al., 2012).

2.1.4 Box-4 (≈684–690 m water depth)

The seafloor backscatter in Box-4 is generally high, indicating the presence of a rough seafloor made of hard material with little to no sediment coverage (Fig. 3). Only towards the eastern edge of the box, reduced backscatter values suggest an increase in the thickness of the shallow sediments. Video surveys revealed crevasses, uplifted rims, and small scarps in the surficial sediments, indicating recent deformation, as well as dead clam fields adjacent to carbonate hardgrounds (Linke, 2011).

2.1.5 Box-8 (≈1,200–1,300 m water depth)

Box-8 is located on the deeper upper slope, downslope of the main carbonate-bearing seep belt of the central Chile forearc, where structural relief and fault-controlled focusing of fluid flow are less pronounced. Regional sidescan mosaics show laterally continuous low- to moderate-backscatter seafloor without elongated ridges, domes, or pinnacles, consistent with a sediment-covered seabed rather than exposed hardgrounds (Klaucke et al., 2012) (Fig. 3). Video surveys confirmed a predominantly soft-sediment habitat with localized reduced patches but no extensive authigenic carbonate pavements or blocks (Linke, 2011).

https://doi.org/10.5194/egusphere-2026-6926
Preprint. Discussion started: 20 November 2026
© Author(s) 2026. CC BY 4.0 License.

2.1.5 Reference Site (1008 m water depth)

To obtain sediment pore water profiles unaffected by methane seepage or tectonically induced fluid flow as comparable control data for the primary Box (1-4, 8) sites, a reference site was sampled using a gravity corer and multicorer. The reference cores were retrieved at a similar latitude and water depth (Table 1), though in an area of smooth seafloor topography, distant from major faults and with intermediate background backscatter intensity.

2.2 Observations, Data Collection, Sampling, and Analyses

Table 1 provides an overview of all instrument deployments and associated station information.

2.2.1 Ocean Floor Observation System (OFOS)

The Ocean Floor Observation System (OFOS) is a frame equipped with the following instruments: two video cameras, a digital still camera system with two remote flash heads (Ocean Imaging Systems), two Xenon lights (Oktopus), CTD (Conductivity-Temperature-Depth; RBR) and three red lasers (Oktopus). The frame was towed behind the SONNE vessel at a speed of about 0.5-0.8 knots (kn). The distance of about ~1.5 m to the seafloor was adjusted manually by the winch operator. For this purpose, a ground weight (20 cm wide) was suspended below the frame on a rope of 1.5 m length. Two laser pointers were used to scale the video and the still camera images. These were positioned in parallel and 50 cm apart, while a third laser pointed at an oblique angle, which became aligned with the other two lasers when the sled was 1.5 m away from the sea floor. The images were taken by remote control. For navigation, the ultra-short baseline (USBL)-based IXSEA POSIDONIA™ system was employed with an USBL beacon mounted on the vessel's hybrid coaxial/fiber-optical cable ~20 m above the frame. Navigation data were graphically displayed and seafloor observations recorded in the Ocean Floor Observation Protocol (OFOP; Huetten and Greinert (2008)).

2.2.2 Remotely Operated Vehicle (ROV)

ROV KIEL 6000 is a 6000-m-depth rated, electric work-class remotely operated vehicle (ROV) manufactured by Schilling Robotics LLC (Abegg and Linke, 2017). Tools installed as standard on the ROV include a high-definition television (HDTV) camera, two high-resolution and -zoom color cameras, one digital still camera and three black-and-white observation cameras. Crucially, the ROV KIEL 6000 system is also equipped with two manipulator arms: one is a seven-function, position-controlled manipulator (ORION type) and the other one is a five-function, rate-controlled manipulator (RIGMASTER type). Additional ROV-equipped tools include a SBE49 FastCAT CTD with a

https://doi.org/10.5194/egusphere-2026-6926
Preprint. Discussion started: 20 November 2026
© Author(s) 2026. CC BY 4.0 License.

DIGIQUARTZ depth sensor, a SIMRAD sonar system, a PNI TCM2-50 compass, a motion reference unit (MRU) containing a gyro compass, and an RDI Doppler velocity log (DVL). For navigation, the USBL-based IXSEA POSIDONIA^{TM} system was employed in combination with a graphic display program (OFOP; Huetten and Greinert (2008)).

A tool sled located in the lower-most part of the ROV is especially dedicated to storing the scientific payload (i.e., collected samples) during deployments. Located on the front of the tool sled are two sample trays which can be opened hydraulically. During the SO210 cruise, the portside sample tray was rigged for sampling push cores and hard rocks. Additionally, it contained two nets and two chisels. On the front plate of the drawer, two 5-L Niskin bottles were mounted for water sampling. The starboard drawer was equipped with a sample box with six compartments of different sizes. A novel SO210 addition was the integration of an underwater chainsaw (ICS Diamond Tools, Model 890F4) into the hydraulic cycle of the ROV (Suppl. Material 1, Fig. 1). The chainsaw was mounted so that it could be reached and operated by the ORION manipulator.

Video-based habitat analysis. High-definition (HD) video footage acquired by the ROV was analyzed separately for each Box to characterize seafloor habitats and associated fauna. Video analyses focused on three components: (1) substrate types, including soft sediment, hard sediment (carbonate plates), individual carbonate outcrops, and massive carbonate boulders; (2) major faunal groups, including vertebrates, crustaceans, molluscs, polychaetes, cnidarians, poriferans, echinoderms, bryozoans, tunicates, and foraminifera, as well as selected sub-groups (e.g., catsharks, squat lobsters, vesicomyid clams, siboglinid tubeworms, sea anemones, sea stars); and (3) sulfur-oxidizing bacterial mats.

For each HD video segment, an Excel-based dataset (Suppl. Material 2) was compiled to document the presence or absence (recorded as *1* or *null*, respectively) and relative abundance of substrates and organisms within each Box using a semi-quantitative scale (*1* = low, *2* = medium, *3* = high). For faunal observations, the occupied substrate was recorded (*1-4*) as: sediment (*1*), carbonate (*2*), other animals (*3*), or hovering above the seafloor (*4*; demersal). Additional contextual data, e.g., the identity of host organisms in cases of epibiosis, were recorded in a comments field.

The compiled HD Excel datasets were then used as structured input to ChatGPT (version 5.2) to generate Box-specific habitat descriptions based on the recorded abundances and substrate associations. These AI-generated descriptions were subsequently cross-checked against the original datasets and systematically revised by the authors to ensure accuracy, consistency, and appropriate scientific interpretation. This semi-quantitative approach was intended to minimize subjective bias and provide a consistent basis for comparing habitat characteristics, relative abundances, and substrate associations among the five Boxes, rather than to quantify absolute species abundances or conduct formal quantitative ecological analyses.

https://doi.org/10.5194/egusphere-2026-6926
Preprint. Discussion started: 20 November 2026
© Author(s) 2026. CC BY 4.0 License.

2.2.3 Ocean Elevator

The Ocean Elevator is a bespoke lander system built at GEOMAR, which serves as a carrier (from the vessel to the seafloor) for scientific instruments that are handled by the ROV at depth (Linke, 2011; Linke et al., 2015). During SO210, the Elevator was used for the first time to deploy a benthic flux chamber and two eddy correlation modules (ECM) in the vicinity of the CMSA sites. The lander and the ROV modules were equipped with acoustic beacons (Homer-ROV; Sonardyne International, Yateley, United Kingdom) for relocation. After its video-guided deployment with a launcher, the ROV unloaded the instruments from the elevator and deployed them at the specific Box study sites. At the end of the measurements, the ROV returned the instruments back to the Elevator and secured them to the platform via hooks and rubber bands. Following ROV recovery, the anchor weight of the Elevator was released by acoustic command, allowing it to float to the water surface and be recovered by the vessel.

2.2.4 BIGO-Type Lander and ROV-Operated Flux Chamber

In situ benthic fluxes of oxygen were determined with a Biogeochemical Observatory (BIGO) lander and an ROV-operated flux chamber. The BIGO contains two circular flux chambers (internal diameter 28.8 cm, area 651.4 cm^2) (Sommer et al., 2006). Upon placement on the sea floor using a video-controlled launching system, the flux chambers were flushed three times for 5 min every 55 min with surrounding water to establish ambient bottom-water conditions inside the chambers. Subsequently, the chambers were slowly (~ 30 cm h^{-1}) driven into the sediment. To remove solutes that might have been released from the sediment during chamber insertion, the chambers were again flushed for ~1 min following chamber insertion into the sediment. O_2 concentrations in each chamber and in the surrounding water were measured every 5 min throughout the deployment using optodes (Modell 3830, Aanderaa, Bergen, Norway). The total O_2 uptake rate (TOU) was calculated using the initial linear decrease of the O_2 concentration in the chamber with time (dCO_2/dt) and the enclosed water volume (V) and area (A) of the flux chamber (Eq. 1).

$$TOU = \frac{V}{A} * \frac{dCO_2}{dt} \quad (1)$$

The water volumes enclosed by benthic chamber 1 and chamber 2 were 14.982 and 15.878 L, respectively. At the end of the BIGO deployment, the sediments retrieved from the chambers were used for additional pore water analyses and microbiological studies.

In addition to the BIGO chambers, a single ROV-operated, benthic flux chamber (McGinnis et al., 2014) was deployed during ROV-8 dive in Box-4 (Table 1). This circular chamber was carefully

https://doi.org/10.5194/egusphere-2026-6926
Preprint. Discussion started: 20 November 2026
© Author(s) 2026. CC BY 4.0 License.

inserted into the sediment using the manipulator of the ROV. Like the BIGO, the ROV-operated chamber was flushed after its insertion into the sediment to remove any solutes that may have been released from the sediment during deployment. The TOU for this chamber was calculated as described above in Eq. 1. Corresponding area of the chamber was 283.5 cm^2 and the volume of the enclosed water body was 6.062 L. The O_2 concentrations in and outside of the flux chamber were measured using optical oxygen sensors (Model 3830, Aanderaa, Bergen, Norway).

2.2.5 Profiler Lander (PRFL)

In Box-2, in situ vertical O_2 and H_2S profiles across the sediment–water interface (SWI) were acquired along transects near sulfide-oxidizing microbial mats using the GEOMAR transecting Profiler Lander (PRFL) (McGinnis et al., 2014).The Profiler Lander was placed at the seabed using the video-controlled launching system (see BIGO, Section #2.2.4). The profiling unit of the Lander allowed the movement of a sensor array of 4 micro-sensors in mm-scale increments along the x- and the y-axes, which were 450 mm and 330 mm long, respectively; the vertical resolution (z-axis) was 100 µm. The microsensors used in this study where provided by Unisense (Denmark) and consisted of 2 x O_2 (Revsbech, 1989), 1 x H_2S (Jeroschewski et al., 1996) and 1 x pH, all with a tip diameter of ~ 50 µm. The microsensors were mounted into the array with a lateral spacing of 25 and their tips were visually aligned prior to the deployment.

The lander was also equipped with an optode (Aanderaa, Norway) mounted ~ 18 cm above the seafloor to record near-bottom time series of O_2 and temperature. A camera system (Ocean Imaging System; Massachusetts, United States) was used to obtain images of the sediment surface at 10-minute intervals to allow for more accurate interpretation of the micro-profiles in relation to specific features of seabed topography and benthic communities. Details on profiles acquisition, microsensors' calibration and diffusive oxygen uptake (DOU) calculation are provided in the Suppl. Material 1, Section 1.1.

The Profiler lander was deployed twice in BOX-2 (Table 1). Each deployment lasted slightly less than 48 h during which up to 27 high-resolution array profiles were performed over a length of approximately 45 cm. During the first Profiler deployment (PRFL-1), 21 sensor-array profiles were collected along a transect across a microbial mat-covered seep habitat. A second deployment (PRFL-2), conducted ~100 m away at the same water depth (~700 m), comprised 27 profiles across a sparsely mat-covered seep habitat.

2.2.6 Eddy Correlation Module (ECM)

In addition to chamber- and micro-sensor-based measurements of benthic O_2 fluxes (Sections 2.2.4 and 2.2.5), turbulence-based O_2 fluxes were measured in the benthic water using an Eddy Correlation Module

https://doi.org/10.5194/egusphere-2026-6926
Preprint. Discussion started: 20 November 2026
© Author(s) 2026. CC BY 4.0 License.

(ECM), which was deployed using the GEOMAR ROV Kiel 6000 at Box-2 and -4 at 705 and 689 m water depth, respectively. The ECM, which was identical to that in McGinnis et al. (2014), consisted of a lightweight stainless steel tripod frame mounting an acoustic Doppler velocimeter (ADV; Vector, Nortek A/S, Rud, Norway), a fast-response Clark-type O_2 microelectrode (provided by R. N. Glud, University of Southern Denmark; (Revsbech, 1989)), a fast-response temperature microsensor (FP07; ISW Wassermesstechnik, Fünfseen, Germany), custom-built (GEOMAR) amplifiers for amplification of the microsensor readings and relaying the signal to the ADV (McGinnis et al., 2011), and an external battery pressure housing to provide sufficient power to the amplifiers. The ADV recorded 3D flow velocities and microelectrode readings with a frequency of 64 Hz. The microsensors were mounted at ~60% angles from the ADV, which was mounted vertically with the measurement volume at 27 cm (Box-2) and 28 cm (Box-4) above the seafloor. For details of ECM data processing and estimation of the turbulence-based ECM O_2 fluxes, see Suppl. Material1, Section 1.2.

2.2.7 Paleo-Oceanography (POZ) Lander

Local benthic water-column hydrodynamics were monitored at CMSA Box-2 and -4 using the Paleo-Oceanography (POZ) lander (Flögel and Dullo, 2011). The low-profile POZ lander has a reduced cross-section and height that allows all mounted sensors to be placed close to the sediment, at ~50 cm above the seafloor. The POZ lander was deployed with the launcher and is equipped a CTD logger (XR-420 CT logger, RBR, Canada) with a Digiquartz high-precision pressure sensor (Paroscientific, Redmond, United States) and a 600 kHz acoustic Doppler current profiler (ADCP; RD-Instruments, Poway, United States). The ADCP on the POZ measured upward looking from the transducer head (positioned 0.5 m above the seafloor) into the water column, from 2.1 m up to 38.18 m above the seafloor, with a vertical resolution of 0.5 m and a temporal resolution of 1 min. However, due to beam attenuation and reduced beam correlation, the practical range of the ADCP was mostly constrained to distances within 20-25 m from the seafloor. The ADCP data were used to compute theoretical particle tracking to visualize the motion of water masses, their corresponding residence time within the investigated study area, and the overall potential for dispersion of solutes and suspended material (see Suppl. Material 1, Fig. 7). More methodological details are provided in Suppl. Material1, Section 1.3.

2.2.8 Sediment Sampling and Analysis

Sediment samples were obtained by the aid of a gravity corer, multicorer, and ROV-guided push cores. The gravity corer was equipped with a headweight of 2 t and a steel pipe fitted to contain PVC-liners (120 mm i.d.). The pipe was composed of segments of 3- or 6-m length depending on sediment type. Upon recovery, liners were cut into 1-m sections and split into halves. One core half was used for visual

https://doi.org/10.5194/egusphere-2026-6926
Preprint. Discussion started: 20 November 2026
© Author(s) 2026. CC BY 4.0 License.

inspection and description; the other half was used for sediment subsampling and pore water recovery. The multicorer was equipped with 6 core liners (100 mm i.d.) and a camera system enabling on-line video transmission for targeted deployment. Multicorer and push cores were stepwise extruded from the core liner and sectioned in 1–4 cm thick discs. Sediment pore water was recovered using a sediment squeezer at pressures between 3 and 5 bar. After squeezing, pore water was filtered through cellulose acetate membrane filters. A small sediment aliquot was stored in pre-weighed and airtight plastic cups for the determination of porosity and solid phase analyses after the cruise. Sub-sampling and pore water recovery were carried out in a cool room at the approximate seafloor temperature of 6°C.

Sediment porewater analyses of chloride (Cl^-), bromide (Br^-), sulfate (SO_4^{2-}), total alkalinity (TA) and total sulfide (ΣH_2S) were performed onboard shortly after pore water recovery. Anion concentrations were measured by ion-chromatography (IC, METROHM 761 Compact, conductivity mode), TA was determined by titration with 0.02 M HCl (Ivanenkov and Lyakhin, 1978) and dissolved sulfide was analyzed by applying the methylene blue method using a Hitachi U2800A spectrophotometer (Grasshoff et al., 1999). Acidified subsamples (concentrated HNO_3, supra pure) were stored in pre-cleaned LDPE vials for shore-based analyses of cations by inductively coupled plasma optical emission spectrometry (ICP-OES, VARIAN 720-ES). To characterize the local bottom water, the supernatant water of multicorer and push cores was treated the same way as described for pore waters. The IAPSO salinity standard was used to check the reproducibility and accuracy of all chemical analyses (Gieskes et al., 1991).

For porewater methane analysis, 3 mL of undisturbed sediment were disaggregated and dispersed in 20 mL sealed glass vials, prefilled with 9 mL of 1.0 M sodium hydroxide, immediately after core retrieval. The glass vials were stored and shipped at 4°C for subsequent laboratory analyses at GEOMAR. The methane concentrations in the head space of the vials were analyzed at GEOMAR by using two different gas chromatographs equipped with capillary column and a flame ionization detector (FID) (Geersen et al., 2016; Scholz et al., 2013). Stable carbon isotope ratios of methane were measured by using Continuous-flow Gas Chromatography–Combustion–Isotope Ratio Mass Spectrometry (GC-C-IRMS). Methane was separated from other gases in a Thermo Trace gas chromatograph (carrier gas: He; packed column: ShinCarbon, 1.5 m). The subsequent conversion of hydrocarbons to carbon dioxide was conducted in a Ni/Pt combustion furnace at 1150°C. The $^{13}C/^{12}C$-ratio of (produced) CO_2 was determined by a Thermo MAT253 isotope ratio mass spectrometer. All isotope ratios are reported in the δ-notation with respect to Vienna Pee Dee Belemnite (VPDB, analytical precision ±0.5 ‰ SD).

The total carbon (TC), total organic carbon (TOC), total nitrogen (N), and total sulfur (S) contents of freeze-dried and ground sediment samples were determined by flash combustion in a Carlo Erba Element Analyzer (NA1500) with a reproducibility of about 1% relative SD. The carbonate carbon was

https://doi.org/10.5194/egusphere-2026-6926
Preprint. Discussion started: 20 November 2026
© Author(s) 2026. CC BY 4.0 License.

removed by adding 1 M HCl prior to TOC analyses and total inorganic carbon (TIC) was calculated by subtracting TOC from TC.

For the determination of AOM and sulfate reduction rates three sub cores (length 30 cm, diameter 2.6 cm, polycarbonate) each (six total) were sampled from one push core. Through small silicon-filled holes, 15 µl $^{14}CH_4$ (1–2 kBq dissolved in anoxic, sterile water; specific activity 22.28 GBq mmol-1), and 6 µl $^{35}SO_4^{2-}$ (200 kBq dissolved in water; specific activity 37 TBq mmol-1), were injected into the sediment of the AOM and sulfate reduction cores, respectively, at a vertical resolution of 1 cm; according to whole-core incubation of (Jørgensen, 1978). After 24-h incubation under in situ temperature in the dark, the sub cores were sliced in 1-cm intervals. AOM samples were transferred into glass vials (50 ml) containing 20 ml 2.5 wt% NaOH, immediately closed with rubber stoppers, and shaken thoroughly, to stop all microbial activity. Sulfate reduction samples were transferred into 50 ml plastic centrifuge vials containing 25 ml 20 wt% Zn-acetate, closed, and shaken thoroughly. Controls (five for AOM, three for sulfate reduction) were first transferred into NaOH and Zn-acetate solution, respectively, before the tracer addition. AOM rates were determined according to Treude et al. (2005a) (CH_4 determination, combustion, and calculation) and Joye et al. (2004) (CO_2 trapping). Sulfate reduction rates were determined according to Kallmeyer et al. (2004).

To investigate sedimentation rates and bioturbation activity in surface sediments from a large clam-shell–dominated area, termed the *Dead Clam Field*, identified in Box-4, radionuclide activities of ^{210}Pb, ^{137}Cs, ^{226}Ra, and ^{241}Am were measured in samples collected at St. 25 (ROV-2, PC-5) and 66 (MUC-3). Radionuclide analyses followed the procedure described in Fleischmann et al. (2025). The ^{210}Pbex activity of each sample i.e., the ^{210}Pb activity in excess of its parent ^{226}Ra, was calculated by subtracting its individual ^{226}Ra activity (mean of the sum of ^{214}Pb and ^{214}Bi activities). Uncertainties include contributions from detector efficiency, calibration procedures, and counting statistics of individual measurements of ^{210}Pb, ^{241}Am, ^{214}Pb, and ^{214}Bi, and were propagated using standard error propagation rules. Relative errors of the measurements ranged between 5% and 35%.

2.2.9 Video-guided grab (TVG) Operations

During OFOS surveys (see Section 2.2.1), different types of authigenic seep carbonates were identified as targets for large-volume sampling. These were recovered using the video-guided grab (TVG) aboard R/V SONNE, which has an opening area of 1.8 m² and a battery-driven hydraulic closing system generating >2 t of pressure, enabling recovery of carbonate blocks larger than the grab volume itself. This technique facilitates sampling of large cross-sections through carbonate-cemented sediments and chemoherm structures, allowing detailed reconstruction of fluid-flow histories, growth structures, calcification processes, and fluid pathways. In addition, recovered blocks preserve associated hard-substrate

https://doi.org/10.5194/egusphere-2026-6926
Preprint. Discussion started: 20 November 2026
© Author(s) 2026. CC BY 4.0 License.

communities, including cold-water corals and seep fauna such as tubeworms, clams, and bacterial mats, providing a valuable complement to the more surface-oriented ROV sampling. During the expedition, TVG deployments recovered large carbonate samples from Box-1 and Box-3 (Table 1, Suppl. Material 3).

2.2.10 U-Th geochronology & light stable isotopes of authigenic carbonates

Sample material and sub-sampling. Massive authigenic carbonates were sampled by TVG and ROV (see Sections 2.2.2 and 2.2.9, respectively, and Suppl. Material 3). Carbonate samples were dried at 20°C for 12 hrs and gently cleaned from loosely bound sediment remains. Homogeneous subsamples (Suppl. Material 3) were collected by drilling material from solidified samples by a handheld, mm-sized mini-drill and from less-consolidated surrounding sediments. From the solidified samples, the surface of each sub-sampling spot was scoured away in an area of ~5 x 5 mm. Subsequently, the original sample powder was extracted by drilling small cavities. Prior to aliquot procedures all samples were finely ground in an agate mortar providing homogeneous aliquots of suitable grain size for the combined approach of mineral identification by X-ray diffractometry (XRD), $\delta^{18}O$ and $\delta^{13}C$ analyses by stable isotope ratio mass spectrometry (SIRMS) as well as for U-Th geochronology by multi collector-inductively coupled plasma-mass spectrometry (MC-ICP-MS).

X-ray diffraction analyses. Using representative aliquots, the semi-quantitatively mineralogical composition was investigated using a x-ray diffraction (XRD) meter equipped with a Philips X-ray diffractometer PW 1710 in monochromatic CuKα mode and measurements between 2 and 70 2θ (incident angle). Resulting spectra were analyzed with the software XPowder (XPowder, Spain). Note, especially on small sample aliquots of few 10 mg as required in this study, relative quantifications are generally accompanied by large uncertainties. Furthermore, the sensitivity for mineral identification is typically restricted to fractions greater than 5% and significant amounts remain unidentified.

Light stable isotope analysis ($\delta^{18}O$ and $\delta^{13}C$). From each homogenized carbonate powder sample (see above), an aliquot of 10 mg was separated for carbon $\delta^{13}C$ and oxygen $\delta^{18}O$ stable isotope analysis. A small part (~1 mg) of this powder was dissolved by water-free phosphoric acid at 73°C in a "Carbo-Kiel" (Thermo Fisher Scientific) online carbonate preparation line and measured for carbon and oxygen stable isotope ratios with a MAT 253 mass spectrometer (Thermo Fisher Scientific). The $\delta^{13}C$ and $\delta^{18}O$ values were calculated as deviations from the laboratory standard referred to the PDB scale and reported in ‰ relative to VPDB. The reproducibility was confirmed by replicate analyses of laboratory standards as being usually better than ±0.02‰ for $\delta^{13}C$ and $\delta^{18}O$ (1SD). In case of larger uncertainties of individual sample measurements, characteristic of impure materials, the higher value is presented.

U–Th geochronology. Age determinations via the U-Th clock were performed on aliquots (sample amount: 15 to 102 mg) of XRD and light stable isotope analyses' samples. Sample preparation

https://doi.org/10.5194/egusphere-2026-6926
Preprint. Discussion started: 20 November 2026
© Author(s) 2026. CC BY 4.0 License.

and mass-spectrometric measurements were carried out at GEOMAR, Kiel. Analytical procedures followed standard lab routines for this sample type as detailed in Berndt et al. (2014). Age uncertainties are primarily limited by the achieved accuracy and precision of the mass spectrometric determination of $^{230}Th/^{234}U$ activity ratios and to a lesser degree the assumption of a common detrital $^{230}Th/^{232}Th$ activity ratio resembling mean continental crust to correct for non-radiogenic ^{230}Th.

2.2.11 Methane Concentrations in the Water Column

Water column measurements were primarily carried using the onboard CTD system. The CTD system consisted of a carousel with a SBE9-plus-CTD (Sea-Bird Electronics, Inc., Washington, USA) equipped with standard sensors (Conductivity, Temperature, Pressure, and Dissolved Oxygen), a pH sensor, and a rosette containing 24 Niskin bottles for discrete water sampling. At each CTD station (Table 1), water samples were collected at discrete water depths. In addition to water sampling during CTD casts, additional water samples were obtained from ~1 m above the seafloor using Niskin bottles during ROV dives. After onboard recovery, all water samplers were immediately subsampled into preevacuated glass bottles following the degassing method described in Keir et al. (2008). The gas released by the vacuum degassing technique was stored in septum-stoppered glass vials for subsequent onboard concentration measurements. Methane concentrations were determined by using a Thermo Scientific TRACE GC Ultra gas chromatograph with a precision of ±0.3% RSD. The gas chromatograph was equipped with a 50 m Rt®-Alumina BOND/KCL capillary column, He carrier gas, and FID detector.

https://doi.org/10.5194/egusphere-2026-6926
Preprint. Discussion started: 20 November 2026
© Author(s) 2026. CC BY 4.0 License.

3. Results and Discussions

3.1 Site-specific results and interpretation

3.1.1 Box-1

Habitat characterization based on video footage. Box-1 represented a carbonate-dominated seep habitat in which lithified surfaces far outweighed soft sediment (Fig. 4, Suppl. Video 1, Suppl. Material 2). Massive carbonate boulders and crusts formed the dominant substrate (high frequency), while smaller carbonate plates and outcrops occurred at medium frequency. Soft sediment was widespread but generally occurred at low frequency, primarily in depressions and patches between carbonates. A single whale skeleton provided an additional localized hard substrate but no longer contained any visible organic matter.

Several chemosynthesis-based habitats were observed within this predominantly lithified environment. Living *Lamellibrachia* sp. tubeworms occurred locally at high abundance (Fig. 4D, E, I), whereas sulfur-oxidizing bacterial mats were restricted to discrete zones of diffuse seepage (Fig. 4D, F, I). In several cases, white bacterial mats grew directly on the tubeworm tubes (Fig. 4F), suggesting active sulfide supply at these sites. Other tubeworm colonies supported dense epifaunal growth (Fig. 4D, E), particularly hydroids and thin sponge films. Vesicomyid clams formed locally dense beds on the sediment surface (Fig. 4D, I). Most visible material consisted of shells and shell debris, and the imagery did not allow living and dead individuals to be reliably distinguished.

The carbonate framework supported a diverse suspension-feeding and predatory community. Soft corals (including gorgonians) were among the dominant sessile organisms (high abundance), forming dense branching thickets on carbonate ledges (Fig. 4A, B). Hydroids and sponges were also common and frequently abundant on hard substrates (Fig. 4E, G). Brittle stars (Ophiuroidea) were widespread and frequently abundant, occurring both on coral branches and partially buried within sediment pockets (Fig. 4B). Squat lobsters (Munidopsidae, Munididae) were common but generally occurred at low abundance, primarily on carbonate surfaces and among gorgonians (Fig. 4A, D, E, G). Large sea anemones were frequently observed settled on exposed carbonate outcrops (Fig. 4C, H). Sediment pockets between carbonate structures locally supported dense assemblages of deposit-feeding polychaetes, potentially including abundant ampharetid tube fields, although identification from the imagery was uncertain, and, at some locations, *Hyalinoecia*-type onuphid worms that dragged their chitinous tubes across the sediment while feeding (Suppl. Video 1, Suppl. Material 2).

Demersal megafaunas were comparatively sparse but diverse. Grenadiers (Macrouridae), catsharks (Scyliorhinidae), and eelpouts (Zoarcidae) occurred at low abundance, together with occasional large Humboldt squid (*Dosidicus gigas*) (Suppl. Video 1). Large skates, identified as *Bathyraja* spp., were also observed in association with carbonate structures. Numerous skate egg capsules previously

https://doi.org/10.5194/egusphere-2026-6926
Preprint. Discussion started: 20 November 2026
© Author(s) 2026. CC BY 4.0 License.

documented between carbonate boulders in the OFOS tracks indicate that this area serves as a regional nursery ground for deep-sea skates (Treude et al., 2011) (Fig. 4H).

During ROV dive ROV-1, the skeletal remains of a whale, presumably a baleen whale (Mysticeti), were discovered at 36.423233° S, 73.7014008° W, at a water depth of 662.7 m (Supplementary Video 1). The skeleton was entirely devoid of soft tissue, with the skull, vertebrae, and ribs scattered across the seafloor. A vertebra recovered during the dive exhibited a highly porous structure upon visual inspection. Close-up video observations of the skull revealed colonization by sessile organisms, indicating that the exposed whale bones provided additional hard substrate for benthic fauna. The absence of soft tissue and the colonization of exposed bones by sessile organisms suggest that the whale fall had reached an advanced stage of ecological succession, potentially corresponding to the reef stage described by Smith et al. (2015). During this stage, following the depletion of organic material, the remaining skeletal structures primarily serve as hard substrates for colonization by suspension-feeding organisms. Within the carbonate-dominated seep environment of CMSA, the whale skeleton thus represented an additional, spatially restricted hard-substrate habitat for sessile benthic organisms.

Authigenic Carbonates. Widespread authigenic carbonate precipitation was detected throughout Box-1, indicating extensive hardground development across the area. Stable carbon isotope compositions of the analyzed carbonate samples ($\delta^{13}C$ = -46.08 to -33.59‰ VPDB) point to a predominantly biogenic origin of the dissolved inorganic carbon, derived from methane oxidation within the slope sediments (Table 2). Similar strongly depleted carbon isotope signatures have been reported for methane-derived authigenic carbonates from other accretionary margins, including the Hikurangi Margin offshore New Zealand (Campbell et al., 2010) and the Cascadia Margin offshore Oregon (Greinert et al., 2001; Loyd et al., 2016), supporting a common methane-seep signature for carbonate precipitation in these tectonic settings. U-Th ages of the analyzed Box-1 carbonates range from 50 to 168 kyr BP (Table 2).

At 670 m, carbonate recovered by TVG-5 consists of a rounded, flat block of consolidated sediment characterized by a dispersed network of veins and tube-like pore spaces partially filled with aragonitic material. Ex situ cutting of the larger carbonate structure revealed multiple semi-horizontal aragonite layers interspersed with open pore spaces separating distinct matrix domains (Suppl. Material 3, P-5/TVG-5). Six subsamples from the structure yielded U-Th ages ranging from 50 to 168 kyr BP (Table 2). The four subsamples taken from the upper rim (TVG-5/1-4), central layer, lower vein, and center area of TVG-5 range from 50 to 85 kyr BP and are strongly dominated by aragonite (92-97 wt%). Two additional subsamples (P-5, 18 and 19) from the dispersed network and pore-volume filling yielded ages of 168 and 69 kyr BP, respectively, and contained 62-76 wt% aragonite with minor calcite and, in P-5/19, dolomite. Across all six subsamples, $\delta^{13}C$ values range from -41.73 to -33.59‰ and $\delta^{18}O$ values from 4.05 to 4.50‰ (Table 2).

https://doi.org/10.5194/egusphere-2026-6926
Preprint. Discussion started: 20 November 2026
© Author(s) 2026. CC BY 4.0 License.

A massive carbonate bank reaching heights of up to ~1 m was documented at 667.0 m. The structure exhibits erosional rounding, with living tubeworms and bacterial mats observed at its base. The carbonate was sectioned during ROV operations to expose its internal structure, allowing subsampling of successive domains from the outer to innermost portions of the bank (Suppl. Material 3, P1). Five analyzed subsamples yielded U-Th ages between 50 and 85 kyr BP and were dominated by aragonite (75-88 wt%), with minor dolomite and calcite (Table 2). $\delta^{13}C$ values vary from -46.08 to -33.91‰. Four subsamples have $\delta^{18}O$ values between 4.39 and 4.66‰, whereas the innermost dark layer has a distinctly lower $\delta^{18}O$ value of -13.50‰ (Table 2).

At the shallowest sampled site in Box-1 (660.6 m), a massive carbonate consists of a dense, consolidated matrix characterized by open vein structures and inclusions of clam-shell fragments (Suppl. Material 3, P7). The analyzed massive aragonitic vein filling yielded a U-Th age of 145 ± 5 kyr BP and consists predominantly of aragonite (66 wt%) with 14 wt% calcite. Its $\delta^{13}C$ and $\delta^{18}O$ values are -37.78 and 4.55‰, respectively (Table 2).

A rare vertical carbonate structure was encountered at 675.8 m and represents an inactive fluid conduit eroded from previously soft sediment. The recovered carbonate consists of a dense, cemented matrix containing open and aragonite-filled veins and was retrieved in two pieces (Suppl. Material 3, P6). The analyzed massive aragonitic vein filling yielded a U-Th age of 61 ± 1 kyr BP, with 81 wt% aragonite and 8.9 wt% calcite. $\delta^{13}C$ and $\delta^{18}O$ values are -43.37 and 4.61‰, respectively (Table 2).

At 676.7 m, a section was recovered from a massive, flat solitary carbonate block with living clams and tubeworms present at its base (Suppl. Material 3, P9). Two subsamples representing a pore-volume filling and a dispersed vein system yielded similar U-Th ages of 95 ± 3 and 91 ± 2 kyr BP, respectively (Table 2). The pore-volume filling contains 68 wt% aragonite, while the mineralogical composition of the dispersed vein sample was not determined. $\delta^{13}C$ values range from -44.55 to -40.53‰ and $\delta^{18}O$ values from 3.67 to 3.76‰ (Table 2).

At 685.5 m, an open vent structure with sulfur-oxidizing bacterial mats and adjacent tubeworms was identified within a sediment-covered massive carbonate block. Downward cutting with the ROV chain saw allowed recovery of the carbonate, while the surrounding substrate was sufficiently cemented to prevent sediment push coring (Suppl. Material 3, P+1). A solid center layer and an adjacent loosely packed granulate yielded U-Th ages of 52 ± 1 and 58 ± 1 kyr BP, respectively (Table 2). The center layer contains 38 wt% aragonite, 19 wt% dolomite, and 16 wt% calcite, whereas the loosely packed granulate is dominated by aragonite (88 wt%). Both subsamples have strongly depleted $\delta^{13}C$ values (-43.41 and -44.57‰), while their $\delta^{18}O$ values differ markedly, at 4.43 and 0.68‰, respectively (Table 2).

Overall, the analyzed Box-1 carbonates record U-Th ages between 50 and 168 kyr BP, with most samples falling between approximately 50 and 95 kyr BP (Table 2). The wide range of carbonate

https://doi.org/10.5194/egusphere-2026-6926
Preprint. Discussion started: 20 November 2026
© Author(s) 2026. CC BY 4.0 License.

morphologies, including layered carbonate banks, vein- and pore-filling cements, a vertical fluid conduit, and vent-associated carbonate, documents extensive carbonate precipitation across Box-1 (Suppl. Material 3).

Methane in the water column. In Box-1, a single CTD cast (CTD-5, St. 20; Fig. 5A) was conducted at the center of the site above a topographic elevation (Fig. 2). The profile revealed a methane maximum of 8.4 nM within the upper pycnocline at ~50 mbsl, which is possibly associated with methane production in surface waters (Mao et al., 2024). However, numerous gas bubble flares localized in the CMSA area could provide an additional source for slightly elevated methane concentrations in the shallower water masses (Wieman et al., 2026). Methane concentrations remained low throughout most of the water column but increased sharply below ~550 m water depth, reaching up to 35 nM near the seafloor.

Niskin bottle samples collected near the seafloor during ROV dives showed substantially elevated methane concentrations ranging from 10 to 587 nM (Fig. 5A). The highest concentrations were measured in water overlying sediments covered by sulfur-oxidizing bacterial mats, followed by clam beds and Lamellibrachid tubeworm assemblages; lowest concentrations (but still in triple-digit nM) were found above crevices in the seafloor (Table 3).

These patterns indicate that methane is enriched near the seafloor in Box-1 and that concentrations scale with seep activity, being highest above habitats associated with stronger methane fluxes (e.g., bacterial mats) and lower above communities with reduced fluxes (e.g., clams and tubeworms) (Treude et al., 2003; Niemann et al., 2006; Cordes et al., 2005). Elevated methane concentrations above seafloor crevices further suggest recent localized methane release.

3.1.2 Box-2

Habitat characterization based on video footage. Box-2 was characterized by extensive soft sediment with spatially patchy but clear signs of active seepage (Fig. 6, Suppl. Video 2, Suppl. Material 2). Soft substrate dominated the area (high abundance), with no larger carbonate outcrops or chemohermal structures. Small, pebble-sized carbonate rocks occurred locally and provided isolated hard substrate for sessile organisms (Suppl. Video 2). Seepage manifested primarily through localized sulfur-oxidizing bacterial mats (Fig. 6A, B, C, F, G, I), which occurred at low to medium abundance across multiple sediment patches and were frequently associated with patches of black reduced sediment. Very small Vesicomyid clams occurred locally at medium abundance, primarily along the edges of or within sulfur-oxidizing bacterial mats, providing an additional indication of active seepage (Suppl. Material 2).

A prominent faunal component consisted of dense aggregations of tube-dwelling polychaetes (Suppl. Video 2, Suppl. Material 2), which locally reached high abundances on the sediment surface.

https://doi.org/10.5194/egusphere-2026-6926
Preprint. Discussion started: 20 November 2026
© Author(s) 2026. CC BY 4.0 License.

Taxonomic identification of these polychaetes was not possible based on the video footage. However, their visual appearance and the absence of characteristic sediment depressions surrounding their tubes, as reported for ampharetid polychaetes at other methane seeps (Sommer et al., 2010; Bowden et al., 2013), suggest that they were unlikely to belong to this family.

The megafaunal assemblage was comparatively sparse but diverse. Grenadiers/rattails (Macrouridae, Fig. 6H) were encountered relatively frequently and occurred at low to high abundance, whereas skates/rays (Rajidae, Fig. 6D), catsharks, and chimaeras occurred more sporadically (Suppl. Video 2). Shrimp (Caridea) occurred at low to medium abundance, primarily on soft sediment (Fig. 6A, I). Echinoderms included occasional sea urchins and brittle or basket stars, whereas pelagic holothurians were encountered repeatedly in the water column (Suppl. Video 2, Suppl. Material 2). A particularly large aggregation of purple bentho-pelagic holothurians (*Eunipniastes* sp.) was observed drifting in the water column during ROV-5 (Fig. 6F). The isolated small carbonate nodules provided attachment substrate for sessile organisms, including gorgonians or other colonial anthozoans, hydroids, and sponges (Suppl. Video 2).

Authigenic Carbonates. ROV dives and OFOS surveys in Box-2 did not reveal major outcropping authigenic carbonate structures that were appropriate for sampling. A single small ridge (approximately 20-30 m long) was observed during OFOS-3 (St. 14-1; 36.4674832° S, 73.6734768° W), crossing an area of higher backscatter area (Fig. #3). Another small ridge was observed during ROV 4 (St. 37; 36.476517° S, 73.673866° W).

Sediment Biogeochemistry. Sediment in Box-2 was characterized by a soft, clay-rich, carbonate-free matrix. Visual indicators of seep activity include subsurface blackened layers, localized black spots exposed at the sediment surface, and areas covered by white mats of sulfur-oxidizing bacteria (Fig. 6).

The occurrence of black sediment patches likely reflects sedimentary reduction associated with sulfide production during AOM, resulting in the formation of iron sulfides. In one sampled location, sulfide production progressed to free sulfide accumulation (3-15 mmol L^{-1}) close to the SWI (Fig. 7E, St. 42), which was accompanied by the development of conspicuous white sulfur-oxidizing bacterial mats. Where free sulfide accumulated only below 5 cm sediment depth (St. 16, 54, and 82), sulfur-oxidizing bacterial mats were absent.

This vertical zonation of sulfide was reflected in measured methane oxidation rates (Fig. 7A), sulfate reduction rates (Fig. 7B), methane concentrations (Fig. 7C), and total alkalinity (TA, Fig. 7F). At Station 42, rates (up to 832 and 774 nmol cm^{-3} d^{-1} for AOM and sulfate reduction, respectively) and concentrations (up to 7.3 mmol L^{-1} methane and 36.3 mEq L^{-1} TA) were high immediately below the SWI, whereas at Stations 16, 54, and 82, increased levels were only observed below ~5–8 cm depth. Conversely, sulfate (Fig. 7D) and calcium (Ca^{2+}; Fig. 7G) concentrations exhibited an opposing depth

https://doi.org/10.5194/egusphere-2026-6926
Preprint. Discussion started: 20 November 2026
© Author(s) 2026. CC BY 4.0 License.

trend, with sharp decreases observed starting at the SWI at Station 42 and below 5–8 cm at Stations 16, 54, and 82. These patterns are consistent with sulfate consumption during methane-dependent sulfate reduction and concomitant removal of Ca^{2+} during carbonate precipitation (Luff and Wallmann, 2003).

A gravity core recovered from the same area (St. 29, Fig. 8 A-E), which sampling location (penetration hole) was later confirmed visually during ROV-5 dive, revealed high methane concentrations (1.7 to 98.2 mmol L^{-1}) down to 300 cm sediment depth, accompanied by elevated total alkalinity (>21 mEq L^{-1}) and sulfide concentrations (>4 mmol L^{-1}). In contrast, sulfate (<2 mmol L^{-1}) and Ca^{2+} (≤4 mmol L^{-1}) concentrations remained low throughout the core, suggesting that the sulfate–methane transition zone (SMTZ) had migrated upward through the sediment column over time, progressively depleting sulfate and Ca^{2+} from the porewater. Because gravity coring commonly disturbs or removes soft surficial sediment, the expected near-surface increases in these parameters at the SWI could not be resolved in this core. The extremely high methane concentration measured at 300 cm depth (98.2 mmol L^{-1}), derived from a sample collected in the core catcher, could indicate the presence of gas hydrates. However, chlorinity concentrations (553 mmol L^{-1}; data not shown) do not indicate the depletion typically associated with gas hydrate dissociation and thus do not provide independent support for this interpretation.

Benthic fluxes of solutes. Benthic fluxes of O_2 in Box-2 were determined using a Profile lander, ECM, and a BIGO lander deployed in an area of soft sediments characterized by patches of white sulfur-oxidizing bacterial mats and blackened sediment spots.

Profiler lander. Profiler deployments in Box-2 at PRFL-1 and PRFL-2 were conducted along parallel transects with similar physical settings (Suppl. Material 1, Fig. 2). ADCP-based current measurements, obtained 5.8 m above the seafloor, revealed similar current velocities of ~9 cm s^{-1} at both sites, with slightly greater variability at PRFL-2. Current direction ranged from 40–140° at PRFL-1 and 150–240° at PRFL-2 and exhibited an apparent ~12 h periodicity reflecting a semidiurnal (M2) dominated tidal signal. Near-bottom O_2 concentrations, measured ~18 cm above the seafloor, were ~130 µmol L^{-1} along both transects and showed little variability.

Time-lapse images from the Profiler camera system showed that the PRFL-1 transect was characterized by frequent occurrences of sulfide-oxidizing bacterial mats of varying spatial extent (Suppl. Material 1, Fig. 2a), whereas at PRFL-2 mats were only observed toward the end of the transect (Suppl. Material 1, Fig. 2c). Sediment topography, derived from the depth of the SWI as determined by O_2 micro-sensor profiles (first profile set to 0 mm), showed maximum relief of 23 mm at PRFL-1 and a ~21 mm depression at the end of the PRFL-2 transect (Suppl. Material 1, Fig. 2b, 2d). Camera images also revealed irregularities in the transecting steps. At PRFL-1, an increased step between profiles 10 and 11 resulted in a 130-mm unsampled gap (Suppl. Material 1, Fig. 2a); consequently, profiles 22–27 were acquired at the same location and are not shown. At PRFL-2, step sizes were inconsistent, with shorter

https://doi.org/10.5194/egusphere-2026-6926
Preprint. Discussion started: 20 November 2026
© Author(s) 2026. CC BY 4.0 License.

steps between profiles 6–7 and 13–14, and a larger step between profiles 26–27 (Suppl. Material 1, Fig. 2c). Because the time interval between profiles remained constant despite these variations, profiles are presented as a function of deployment time rather than distance.

A total of 42 and 54 O_2 profiles were collected at PRFL-1 and PRFL-2, respectively. After quality control assessment, 34 (PRFL-1) and 39 (PRFL-2) profiles were retained for analysis. Representative profiles are shown in Suppl. Material 1, Fig. 3. O_2 profiles exhibited well-defined diffusive boundary layers (DBLs), with δ_{DBL} ranging from 0.1–1.6 mm (mean 0.5 ± 0.4 mm) at PRFL-1 and 0.2–1.3 mm (mean 0.5 ± 0.5 mm) at PRFL-2 (Suppl. Material 1, Fig. 4). Consistent with theoretical expectations, δ_{DBL} varied inversely with near-bottom current velocity. At PRFL-1, δ_{DBL} decreased from 0.8 mm during low flow (~5 cm s^{-1}) to 0.3 mm during high flow (~11 cm s^{-1}). At PRFL-2, δ_{DBL} decreased from 0.4 mm (~6 cm s^{-1}) to 0.2 mm (~13 cm s^{-1}), although the change was less pronounced than at PRFL-1.

At PRFL-1, where the sediment was more widely covered with bacterial mats, the depth of O_2 penetration into the sediment (z_{max}) displayed limited variability along the transect and was on average 29% of that observed on PRFL-2 (1.7 mm and 5.9 mm, respectively; Suppl. Material 1, Fig. 4). Correspondingly, z_{max} strongly decreased near the few regions of reduced, anoxic sediment covered with bacterial mats along PRFL-2 (Suppl. Material 1, Figs. 2 and 4), which supports sediment-side control of *DOU* and z_{max}. Variability in z_{max} showed no relation to changes in near-bottom O_2 concentrations, regardless of the differing bacterial mat coverage between habitats. A clear suboxic zone within the sediment, defined as the zone between z_{max} and the depth of H_2S detection, was observed in all profiles where H_2S was present (Suppl. Material 1, Fig. 3). Suboxic-zone thickness at PRFL-1 ranged from 2.9 to 20.2 mm (average 14.3 ± 4.6 mm) at PRFL-1 and from 2.1 to 18.8 mm (average 10.6 ± 4.6 mm) at PRFL-2.

At PRFL-1, DOU was higher (mean 8.4 mmol m^{-2} d^{-1}) and more variable than at PRFL-2 (mean 4.1 mmol m^{-2} d^{-1}) (Table 4). Statistical analysis indicated that at least eight sensor array profiles (i.e., 16 O_2 profiles) were required to obtain robust DOU estimates for habitat comparisons along each transect. A reliable differentiation between PRFL-1 and PRFL-2 based on DOU required ≥13 profiles (26 O_2 profiles), indicating that shorter transects could have led to the erroneous conclusion that DOUs at both sites were similar.

H_2S was detected more frequently at PRFL-1 than at PRFL-2 (i.e., in 15/21 vs. 6/27 profiles; for representative profiles see Suppl. Material 1, Fig. 3), with a maximum concentration of 132 µmol L^{-1} (profile 23 at PRFL-2, data not shown). The presence of H_2S was consistently associated with shallower O_2 penetration depths (z_{max}), reduced variability in z_{max}, and elevated DOU (Suppl. Material 1, Fig. 4). This relationship was most pronounced at PRFL-2 where z_{max} was markedly reduced in the presence of H_2S, while the same trend was less distinct at PRFL-1. Across both transects, average DOU was higher at

https://doi.org/10.5194/egusphere-2026-6926
Preprint. Discussion started: 20 November 2026
© Author(s) 2026. CC BY 4.0 License.

profile sites where H_2S was present (Table 4, Suppl. Material 1, Fig. 4). Because H_2S was rarely absent at PRFL-1 and only occasionally present at PRFL-2, the two transects can be distinguished in terms of reactivity. PRFL-1 represents a more reactive, sulfidic environment, whereas PRFL-2 reflects less-reactive conditions. This interpretation is consistent with the generally higher DOU and shallower z_{max} observed at PRFL-1 as compared to PRFL-2 (Suppl. Material 1, Fig. 4; Table 4).

Eddy Correlation Module. In Box-2, the ECM (ROV-4; ECM-1 and -2) recorded an 18-h time series of 3D flow velocity and O_2 concentration. Near-bottom O_2 ranged from 142–154 µmol L^{-1} (Suppl. Material 1, Fig. 5a), while corresponding acoustic doppler velocimeter (ADV) measurements (27 cm above the seabed) showed flow velocities of 0.1–5.9 cm s^{-1} (Suppl. Material 1, Fig. 5b; mean 2.3 cm s^{-1}). Spectral analysis indicated that flow <2 cm s^{-1} did not sustain turbulent transport; corresponding fluxes were excluded. Turbulent O_2 uptake fluxes (1-h bins) ranged from 2.3 to 15.5 mmol m^{-2} d^{-1} (Suppl. Material 1, Fig. 5c; mean 9.1 ± 5.0 mmol m^{-2} d^{-1}) and correlated with flow but not with O_2 concentration (Suppl. Material 1, Fig. 5d and e). The average roughness length (z_0) was 7.8 mm. Footprint analysis (Berg et al., 2007) indicates that fluxes were integrated over an area of ~48 m^2 (34 m × 1.8 m), with dominant contributions from ~1.3 m upstream of the ADV.

BIGO lander. In Box-2, DOU was elevated (16.4 and 9.1 mmol m^{-2} d^{-1}; Table 4) relative to the global average for comparable water depths (~2.8 mmol m^{-2} d^{-1} at ~700 m, (Jørgensen et al., 2022)), indicating enhanced benthic reactivity. Geochemical profiles from sediment cores collected in Chamber 1 (K1; Fig. 7) revealed low methane concentrations and near-seawater sulfate levels in the surface sediment (0-8 cm) indicating limited near-surface AOM and sulfide production. Elevated sulfate reduction and methane oxidation rates at depth (> 8 cm) suggest that AOM is largely confined to deeper sediment horizons, where sulfide is produced but does not reach the SWI.

Methane in the water column. In Box-2, two CTD casts (CTD-4 and CTD-10) were conducted at approximately the same location within a broader area characterized by soft sediments, blackened patches of reduced sediment, and sulfur-oxidizing bacterial mats (Fig. 2B). While CTD-4 sampling focused on depths below 300 m, CTD-10 provided a full-depth profile from surface to seafloor.

In CTD-4, methane concentrations remained below 5 nM until ~689 m water depth, below which they increased sharply to reach up to 60 nM near the seafloor (Fig. 5C). In CTD-10, near-bottom methane concentrations were similarly high; however, the increase was observed to start at a shallower depth of ~494 m.

ROV-based Niskin samples collected directly above black sediment patches during dive ROV-4 exhibited methane concentrations approximately two- to four-fold higher than those measured in the CTD casts (Fig. 5C, Table. 3). These elevated concentrations support that reduced seep sediments were the primary source of methane and indicate localized enrichment near the seafloor.

https://doi.org/10.5194/egusphere-2026-6926
Preprint. Discussion started: 20 November 2026
© Author(s) 2026. CC BY 4.0 License.

3.1.3 Box-3

Habitat characterization based on video footage. Box-3 was characterized by a heterogeneous mixture of soft sediment and authigenic carbonate structures, with soft sediment forming a substantial component of the seafloor (Fig. 9, Suppl. Video 3). The OFOS and ROV surveys showed scattered exposed carbonate boulders, ledges, and plates rather than a continuously carbonate-dominated seafloor. ROV push coring additionally revealed subsurface carbonates and rising gas bubbles from methane-charged sediments (Linke, 2011). Sulfur-oxidizing bacterial mats occurred patchily at low to occasionally medium abundance, including thin white films in cracks between carbonate structures (Fig. 6C, F, G) and in sediment depressions (Fig. 6B), indicating spatially localized active seepage.

The exposed carbonate surfaces supported a diverse sessile epifauna. Cemented serpulid tubes were locally abundant on exposed carbonate (Suppl. Video 3, Fig. 9E, G), while living siboglinid tubeworms (Lamellibrachid) occurred at medium abundance, typically in association with carbonate structures or sediment-carbonate contacts (Suppl. Video 3, Fig. 9B, F). Soft corals and gorgonians (Fig. 9A, C, E), including the distinctive coiled, stalked octocoral *Acanella* sp. (Suppl. Video 3, Fig. 9C), occurred on carbonate surfaces, while Epizoanthus-type colonial anthozoans (Fig. 9G), hydroids, sponges, and sea anemones (Suppl. Video 3, Fig. 9C) contributed additional, more localized components of the hard-substrate community.

Chemosynthetic fauna also occurred within the sediment-carbonate mosaic. Vesicomyid clams formed locally dense assemblages at medium to high abundance, particularly on sediment and within cracks between carbonate boulders (Fig. 9B, F, H). Many consisted of dead shells or shell accumulations (Suppl. Video 3), although living individuals were also observed. Together with the Lamellibrachid tubeworms and localized sulfur-oxidizing bacterial mats, these assemblages indicated ongoing seep activity within an otherwise heterogeneous benthic habitat.

Mobile invertebrates occurred at variable abundance on both carbonate and sediment. Sea urchins were widespread and generally occurred at medium abundance (Fig. 9C), primarily in association with carbonate structures, while brittle and basket stars were also common and generally occurred at medium abundance sometimes associated with gorgonians (Suppl. Video 3, Fig. 9A, E). Squat lobsters occurred occasionally at low abundance on carbonate surfaces, including in association with anthozoan colonies (Supp. Material 3), whereas shrimp occurred occasionally at low abundance on soft sediment. Sea stars and octopuses were recorded sporadically at low abundance (Suppl. Video 3).

Soft-sediment patches supported additional polychaete assemblages, including locally abundant *Hyalinoecia*-type quill worms observed feeding on the sediment surface (Fig. 9D, I). These sediment-

https://doi.org/10.5194/egusphere-2026-6926
Preprint. Discussion started: 20 November 2026
© Author(s) 2026. CC BY 4.0 License.

associated communities contributed to the pronounced small-scale heterogeneity of Box-3 and occurred alongside the clam assemblages, Lamellibrachid tubeworms, and other seep-associated fauna.

Authigenic Carbonates. Carbonates recovered from Box-3 comprise two contrasting structures from the deeper part of the CMSA. At the deepest sampling site (1022 m), TVG-4 recovered a massive carbonate block characterized by highly resistant laminated aragonite layers that protect the outer surface from progressive erosion. Pockets of soft sediment are preserved within open pore spaces enclosed by laminated aragonite, and ex situ cutting revealed the complex three-dimensional internal architecture of the block (Suppl. Material 3, TVG-4). Seven subsamples were obtained from different structural domains, including the upper rim, several laminated white layers, a bottom network, and a soft sediment filling.

The five domains for which mineralogical analyses were available are strongly dominated by aragonite (90-96 wt%). Across all seven subsamples, $\delta^{13}C$ values range from -51.41 to -46.88‰ VPDB and $\delta^{18}O$ values from 3.97 to 5.60‰ (Table 2). U-Th ages span a wide range from 173 ± 9 to 530 ± 175 kyr BP, but the U-series systematics indicate that these apparent ages need to be interpreted with caution. Initial $\delta^{234}U$ values range from 37 to 128‰ and are consistently below the seawater value, with particularly low values of 37-71‰ in several carbonate domains (Table 2). The large spread in apparent ages, together with the anomalous initial U isotope compositions and the complex laminated architecture, is consistent with a multi-stage precipitation history and possible open-system behavior rather than a simple sequence of discrete, reliably dated formation events. The soft sediment filling is compositionally distinct within this structure, with a much lower $^{238}U/^{232}Th$ ratio (12.87) than the analyzed carbonate domains (783.57-6705.18), but the available data do not establish whether this material was incorporated during carbonate growth or introduced subsequently (Table 2).

At 1008 m, a carbonate fragment was detached by ROV manipulator from a large overhanging carbonate plate above a prominent crack. The crack may represent an active seepage pathway, and both the recovered fragment and carbonate surfaces surrounding the crack were densely covered by filamentous sulfur-oxidizing bacterial mats (Suppl. Material 3, P0). In contrast to the aragonite-dominated TVG-4 structure, the two analyzed P0 subsamples are strongly dolomite-dominated. The soft carbonate contains 72 wt% dolomite, whereas the hard carbonate contains 72 wt% dolomite, 8.2 wt% aragonite, and 5.2 wt% lansfordite (Table 2). The two subsamples have $\delta^{13}C$ values of -40.91 and -35.87‰ and $\delta^{18}O$ values of 4.75 and 7.64‰, respectively (Table 2).

A U-Th age of 180 ± 28 kyr BP was obtained for the soft carbonate, whereas the hard carbonate was not dated (Table 2). The dated sample has a low $^{238}U/^{232}Th$ ratio of 3.95 and an anomalously high initial $\delta^{234}U$ value of 287‰, indicating that its U-Th age should also be regarded with caution. Notably, its U isotope deviation is opposite to that observed in TVG-4, where initial $\delta^{234}U$ values are consistently below the seawater value. The distinct mineralogy and isotope systematics of P0, together with its

https://doi.org/10.5194/egusphere-2026-6926
Preprint. Discussion started: 20 November 2026
© Author(s) 2026. CC BY 4.0 License.

association with a crack and sulfur-oxidizing bacterial mats, indicate a carbonate precipitation environment distinct from that represented by the laminated aragonitic TVG-4 block, although the available data do not constrain the processes responsible for these differences.

Sediment Biogeochemistry. Sediment-hosted seep habitats were rare in Box-3. Only one prominent site, characterized by adjacent patches of sulfur-oxidizing bacterial mats, chemosymbiotic clams, and Lamellibrachid tubeworms (Fig. 9B), was investigated using ROV push cores (St. 98). Porewater geochemical profiles obtained from cores ranging between 14 and 19 cm in length revealed distinct differences among the three habitat types (Fig. 10). The highest methane (up to 9.5 mmol L^{-1}, Fig. 10C), sulfide (up to 15.5 mmol L^{-1}, Fig. 10E), and total alkalinity (up to 32.6 mEq L^{-1}, Fig. 10F) concentrations were measured beneath the bacterial mats. Intermediate concentrations were observed beneath the clam bed (methane up to 5.5 mmol L^{-1}; sulfide up to 14.5 mmol L^{-1}; total alkalinity up to 31.2 mEq L^{-1}), whereas the lowest concentrations occurred beneath the tubeworm field (methane up to 0.39 mmol L^{-1}; sulfide below detection; total alkalinity up to 3.31 mEq L^{-1}). Conversely, sulfate (Fig. 10D) and Ca^{2+} (Fig. 10G) concentrations showed the strongest depletion beneath the mats (minimum 3.89 and 4.36 mmol L^{-1}, respectively), while profiles beneath the tubeworm field remained largely unchanged with depth.

Process rate measurements, however, did not fully mirror these porewater trends. Methane oxidation (Fig. 10A) and sulfate reduction rates (Fig. 10B) beneath the mats (up to 46 and 45 nmol cm^{-3} d^{-1}, respectively) were similar or even lower than those measured beneath the clam field (up to 177 and 68 nmol cm^{-3} d^{-1}, respectively). Given the small and patchy distribution of the mats, a likely explanation is slight spatial offset between cores: the porewater core may have been positioned directly within the mat, whereas the rate core was collected adjacent to it and therefore did not fully capture mat-associated AOM activity. Nevertheless, methane concentrations measured in the AOM incubation samples remained high (1–2 mmol L^{-1}, data not shown) across all three replicate sub-cores, indicating that methane was readily available but not consumed to the extent expected based on its availability. One possible explanation is that methane flux increased only recently in this sediment section, such that the AOM community had insufficient time to develop biomass capable of sustaining higher oxidation rates. Irrespective of the underlying cause, the observed differences between closely spaced sediment cores underscore the highly localized and focused nature of seepage at this site.

Methane oxidation rates were highest in the uppermost sediment layer beneath the Lamellibrachid tubeworm field (up to 461 nmol cm^{-3} d^{-1}), exceeding those measured beneath the mats and clam beds. Sulfate reduction was not detected at this habitat, except for a minor activity of 5.08 nmol cm^{-3} d^{-1} at 18–19 cm depth in one replicate. The absence of elevated sulfate reduction suggests that the observed methane oxidation primarily reflects aerobic methane oxidation rather than sulfate-dependent AOM.

https://doi.org/10.5194/egusphere-2026-6926
Preprint. Discussion started: 20 November 2026
© Author(s) 2026. CC BY 4.0 License.

Enhanced methane oxidation beneath the tubeworm field may be linked to methane transport through the tubeworm tubes from deeper sediment layers to the sediment–water interface, where it becomes accessible to aerobic methanotrophs. The tubes may also facilitate deeper oxygen penetration into the sediment. Alternatively, methane oxidation could be coupled to other electron acceptors, such as nitrate or iron.

Methane in the water column. In Box-3, two CTD casts (CTD-2 and CTD-11) were conducted approximately 310 m apart above a depression between two mound-shaped chemoherm structures (Fig. 2). No ROV-based Niskin samples were collected at this site. Methane concentrations remained low throughout both profiles (1–15 nM), and no increase was observed near the seafloor (Fig. 5C). Although the CTD casts may not have captured localized methane emissions, the low water-column concentrations indicate comparatively low methane release at the locations surveyed.

3.1.4 Box-4

Habitat characterization based on video footage. Box-4 consisted of a heterogeneous seafloor dominated by soft sediment with numerous small carbonate nodules and occasional larger outcrops (Fig. 11, Suppl. Video 4, Suppl. Material 3). Several decimeter-deep cracks cut through the sediment (Fig. 11E), and sulfur-oxidizing bacterial mats were widespread but patchy (Suppl. Video 4, Fig. 11E, F, H) and generally occurred at low abundance, frequently along the cracks and in small depressions. These cracks likely represent relatively recent pathways for fluid migration, potentially related to seismic activity (Geersen et al., 2016), and the occurrence of sulfur-oxidizing bacterial mats suggests that sulfide production through AOM had become established along at least some of these seepage pathways. The carbonate nodules created substantial small-scale relief and provided the primary hard substrate available to sessile fauna (Suppl. Video 4, Fig. 11D, H).

A major feature of Box-4 was a dense dead clam field situated within a depression (Fig. 11A, B, C) and partly surrounded by carbonate structures and Lamellibrachid tubeworms (Suppl. Video 4). Vesicomyid clams (*Calyptogena* sp.) occurred at high abundance within the field, with dense accumulations of articulated shells, including numerous open individuals that were clearly dead. Some shells remained closed and upright, and their living status could not be determined from the imagery alone. Reduced, blackened sediment was visible beneath parts of the clam layer during sediment coring. Living epifauna within the clam field was sparse: hydroids occurred in patches but were frequently sediment-covered, while Lamellibrachid tubeworms occurred primarily around the margins of the depression and adjacent carbonate structures. Sulfur-oxidizing bacterial mats also occurred locally within the dead clam-field habitat, including on Lamellibrachia tubes and small carbonate surfaces, while some Lamellibrachia tubes were densely covered by hydroids (Suppl. Video 4).

https://doi.org/10.5194/egusphere-2026-6926
Preprint. Discussion started: 20 November 2026
© Author(s) 2026. CC BY 4.0 License.

Outside the dead clam field, soft-sediment habitats supported dense fields of unidentified tube-dwelling polychaetes, which occurred at medium to high abundance (Suppl. Material 2). A single distinct field of frenulate tubeworms, characterized by thin, soft tubes forming dense bushes, occurred away from the dead clam field and locally reached high abundance (Suppl. Video 4, Fig. 11F). Lamellibrachid tubeworms also occurred elsewhere as more isolated tubes protruding from the sediment and carbonates (Fig. 11D). Additional sediment-associated fauna included *Hyalinoecia*-type quill worms, brittle stars extending their arms from the sediment, and occasional sea cucumbers (Suppl. Material 2). A dense accumulation of dead solemyid clams was also observed locally on the sediment surface, with numerous open shells, some of which remained upright (Suppl. Material 2).

Carbonate nodules across the site hosted a diverse suite of suspension feeders (Suppl. Video 4, Fig. 11D, I). Hydroids were particularly common and frequently reached medium abundance, while sea anemones, soft corals and gorgonians, sponges, and occasional scleractinian corals occurred at generally low to medium abundance. Brittle stars, sea urchins, and sea cucumbers also occurred on individual carbonate nodules. Gorgonians and other sessile organisms appeared preferentially on nodules without sea urchins (Suppl. Material 2), suggesting that grazing by sea urchins may have limited sessile colonization on some carbonate surfaces (Fig. 11D). Squat lobsters and shrimp occurred at low abundance on carbonate structures, gorgonians, and adjacent soft sediment.

Authigenic Carbonates. In Box-4, carbonate was recovered at 683.7 m from an area characterized by outcropping porous carbonate plates that were intermingled and densely populated by living lamellibrachid tubeworms. The recovered sample also had attached tubeworms and was subsampled from the downside surface and internal layers (Suppl. Material 3, P-4).

The two subsamples were strongly dominated by aragonite, with 93 wt% aragonite in the surface layer and 80 wt% aragonite plus 10 wt% calcite in the internal layer (Table 2). Their $\delta^{13}C$ values of -45.56 and -46.40‰ VPDB indicate a strong contribution of methane-derived carbon to carbonate precipitation, while $\delta^{18}O$ values were 3.53 and 3.14‰, respectively.

U-Th dating yielded ages of 4.7 ± 0.1 kyr BP for the surface layer and 5.7 ± 0.2 kyr BP for the internal layer (Table 2), representing the youngest dated carbonates in the analyzed CMSA dataset. Both samples show comparatively consistent U-Th systematics, with high $^{238}U/^{232}Th$ ratios of 1335 and 208 and initial $\delta^{234}U$ values of 141 ± 2.8 and 144 ± 2.4‰, respectively, close to the seawater value. Together with the small analytical uncertainties and similar ages of the two subsamples, these characteristics support a relatively reliable late-Holocene chronology for carbonate formation at this site.

The strongly ^{13}C-depleted carbonate signatures document methane-influenced precipitation approximately 5-6 kyr ago, whereas the presence of living lamellibrachid tubeworms demonstrates that seepage activity was still ongoing at the site when it was observed.

https://doi.org/10.5194/egusphere-2026-6926
Preprint. Discussion started: 20 November 2026
© Author(s) 2026. CC BY 4.0 License.

Sediment Biogeochemistry. Biogeochemical characteristics of sediments within the dead clam field of Box-4 were investigated using ROV push cores, benthic chamber deployments, multicorer samples (Fig. 12), and a gravity core (Fig. 8 F-J). Sediment cores recovered from the benthic chamber (St. 88, BC) and ROV push cores (St. 25, PC-3 and -5) exhibited very high rates of methane oxidation (up to 856 nmol cm^{-3} d^{-1}) and sulfate reduction (up to 1946 nmol cm^{-3} d^{-1}), peaking between 5 and 10 cm depth (Fig. 12). These elevated rates coincided with steep increases in methane (up to 3.1 mmol L^{-1}), sulfide (up to 17.4 mmol L^{-1}), and total alkalinity (up to 37.0 mEq L^{-1}), as well as pronounced decreases in sulfate (down to 2.62 mmol L^{-1}) and Ca^{2+} (down to 3.9 mmol L^{-1}), reflecting intense AOM-driven sulfide production and carbonate precipitation. A gravity core (GC-13, St. 41, Fig. 8 F-J), revealed a well-defined, shallow SMTZ between approximately 10 and 30 cm depth (total core length approximately 87 cm). Below the SMTZ, methane concentrations reached up to 3.54 mmol L^{-1}, while sulfate declined to 0.33 mmol L^{-1}. In parallel, total alkalinity (up to 29.2 mEq L^{-1}) and sulfide (up to 9.3 mmol L^{-1}) increased strongly, whereas Ca^{2+} decreased. Together, these sediment data from the dead clam field indicate intense AOM activity fueled by high methane availability, resulting in substantial hydrogen sulfide production in the near-surface sediment.

ROV push cores PC-1 and PC-5 (St. 88) were collected approximately 200 m from the center of the dead clam field in an area of soft sediment characterized by dense, grass-like assemblages of frenulate tubeworms (Fig. 11F). Similar to sediments associated with lamellibrachid tubeworms in Box-3 (Fig. 10A), these sediments exhibited high methane oxidation rates near the sediment surface (up to 543 nmol cm^{-3} d^{-1}) that were not accompanied by elevated sulfate reduction ($\leq$ 5 nmol cm^{-3} d^{-1} at corresponding depths) (Fig. 12A). This pattern indicates that methane oxidation was likely predominantly aerobic. Enhanced methane oxidation may be linked to transport processes along the tubeworm tubes, which can facilitate both upward methane flux and downward oxygen penetration. Methane concentrations reached only ~0.09 mmol L^{-1} at 5 cm depth (the deepest sampled horizon), while sulfate showed only a slight decrease and total alkalinity and sulfide increased modestly below ~8 cm. These trends indicate comparatively low methane fluxes and a deeper zone of AOM activity relative to the dead clam field.

Another gravity core (GC-18, St. 60; total length ~572 cm), collected approximately 2 km from the clam field at the base of the elevation hosting the site, revealed a shallow SMTZ comparable to that observed in GC-13 within the dead clam field (Fig. 8 F-J). Methane, sulfate, total alkalinity, sulfide, and Ca^{2+} concentrations within the upper 1 m were similarly consistent with those measured in GC-13.

Together, these observations suggest that methane fluxes in Box-4 are spatially heterogeneous, with localized zones of focused seepage interspersed with areas of comparatively low flux. However, the available dataset is too limited to fully resolve the spatial variability of methane supply across the site.

https://doi.org/10.5194/egusphere-2026-6926
Preprint. Discussion started: 20 November 2026
© Author(s) 2026. CC BY 4.0 License.

Sedimentation Rate and Bioturbation at the Dead Clam Field. At the Dead Clam Field site, a decrease of $^{210}Pb_{ex}$ specific activities with depth was observed in both sediment cores investigated. To minimize the effects of variable water content and sediment compaction, $^{210}Pb_{ex}$ activities were plotted against cumulative sediment mass (Fig. 13). Both cores exhibit mixed surface layers (St. 25, ROV-2, PC-5: 0–2 cm; St. 66, MUC-3: 0–1 cm), consistent with recent bioturbation. Excluding these mixed layers, sediment mass accumulation rates derived from logarithmic fits to the cumulative mass distributions of $^{210}Pb_{ex}$ are 0.12 ± 0.05 g cm^{-2} yr^{-1} (St. 25 ROV2) and 0.15 ± 0.06 g cm^{-2} yr^{-1} (St. 66 MUC-3). These values agree well with previous investigations along the Chilean continental margin (Muñoz et al., 2004). Measurable ^{241}Am was detected only in core St. 66 MUC-3. If its first occurrence marks the onset of atmospheric nuclear weapon testing in 1954, an independent mass accumulation rate of 0.11 ± 0.03 g cm^{-2} yr^{-1} was calculated, in good agreement with the $^{210}Pb_{ex}$-derived rate of 0.15 ± 0.06 g cm^{-2} yr^{-1}.

Benthic fluxes of solutes. Benthic fluxes of O_2 in Box-4 were determined using an ECM and an ROV-operated benthic chamber deployed within the Dead Clam Field.

Eddy Correlation Module. In Box-4, the ECM (ROV-8; ECM-1 and -2) recorded a 12-h time series of 3D flow velocity and O_2 concentration. Near-bottom O_2 ranged from 152–155 µmol L^{-1} (Suppl. Material 1, Fig. 6a), and flow velocities (28 cm above the seabed) ranged from 0.1–7.2 cm s^{-1} (Suppl. Material 1, Fig. 6b; mean 2.5 cm s^{-1}). Spectral analysis showed that flow <3 cm s^{-1} was insufficient for turbulent transport and fluxes obtained during these flow periods were excluded. Turbulent O_2 uptake ranged from 5.2 to 7.0 mmol m^{-2} d^{-1} (Suppl. Material 1, Fig. 6c; mean 6.3 ± 1.1 mmol m^{-2} d^{-1}) and correlated with flow but not with O_2 concentration (as also observed in Box-2; Suppl. Material 1, Fig. 6d, 6e). The average sediment surface roughness parameter (z_0) was 1.3 cm. Footprint analysis indicates flux integration over ~42 m² (29 m × 1.8 m), with primary contributions from ~1 m upstream of the ADV.

ROV-operated Benthic Chamber. In Box-4, total oxygen uptake (TOU) was markedly elevated (−38.9 mmol m^{-2} d^{-1}), with bottom-water O_2 decreasing from ~140 to ~10 µmol L^{-1} over 33 h, indicating intense benthic oxygen consumption (Table 4). The magnitude of O_2 uptake indicates that oxidation of reduced compounds was likely a major driver. This interpretation is supported by the corresponding sediment profiles (BC; Fig. 12), which show elevated rates of AOM and sulfate reduction extending into the upper centimeters, indicating a shallow and highly active redox zone. Despite substantial sulfide production at depth, porewater sulfide concentrations remain low near the sediment surface, consistent with efficient re-oxidation at or below the sediment–water interface. Given the dead clam-bed setting and the likelihood that elevated sulfide concentrations suppress benthic fauna, the contribution of macrofaunal respiration to the observed O_2 uptake was likely minor. Overall, the O_2 fluxes and sediment data indicate a highly reactive system in which O_2 consumption is dominated by near-surface oxidation of reduced species, with additional contributions from nitrification.

https://doi.org/10.5194/egusphere-2026-6926
Preprint. Discussion started: 20 November 2026
© Author(s) 2026. CC BY 4.0 License.

Methane in the water column. In Box-4, three CTD casts were conducted (Fig. 2), revealing pronounced spatial variability in water column methane concentrations. Across all casts, methane concentrations in the upper ~400 m remained below, and often well below, 10 nmol L^{-1}, with the exception of a localized peak of 99 nmol L^{-1} at 203 m in CTD-7 (Fig. 5D), which might also be related to gas bubble flares frequently observed in the CMSA area (Wieman et al., 2026).

In CTD-13, conducted above the Dead Clam Field, methane concentrations remained consistently below 10 nmol L^{-1} throughout the water column, including near the seafloor at 681 m. In contrast, CTD-7, located above a slope to the north of the Dead Clam Field, exhibited increasing methane concentrations below ~550 m, reaching 35–92 nmol L^{-1} between 550 and 699 m. The highest concentrations were observed in CTD-6, also situated above the Dead Clam Field, where methane levels began to exceed 10 nmol L^{-1} at ~610 m and increased further to >100 nmol L^{-1} toward the seafloor, with a maximum of 167 nmol L^{-1} at 677 m.

Near-seafloor methane concentrations thus vary by up to three orders of magnitude among the three casts, highlighting pronounced spatial heterogeneity in methane input to the water column. This variability is particularly notable given that CTD-13 (lowest concentrations) and CTD-6 (highest concentrations) were conducted above the Dead Clam Field. This variability is further supported by ROV-based Niskin sampling (Fig. 5D, Table 3). The highest methane concentrations were measured inside the Dead Clam Field above sulfur-oxidizing bacterial mats (St. 25, StB) and above clams (St. 25, BB), reaching 3776 and 1984 nmol L^{-1}, respectively. In contrast, samples collected above seafloor cracks and rims outside the Dead Clam Field exhibited substantially lower and more variable concentrations, ranging from 5 to 411 nmol L^{-1}.

3.1.5 Box-8

Habitat characterization based on video footage. During the limited survey of Box-8, the observed seafloor consisted of carbonate plates and small outcrops interspersed with soft sediment, with massive carbonate boulders encountered locally (Fig. 14, Suppl. Video 5, Suppl. Material 2). Carbonate plates and nodules were prominent throughout the observations (Fig. 14A-D, F), whereas soft sediment generally occurred at low to medium abundance (Fig. 14E). Because survey coverage of Box-8 was comparatively limited, these observations should be regarded as a characterization of the visited area rather than necessarily representative of the entire box.

The exposed carbonates supported conspicuous sessile assemblages dominated by gorgonians and other soft corals, which frequently occurred at high abundance (Suppl. Video 5, Fig. 14A, C). Hydroids were locally present at medium abundance, while sponges generally occurred at low abundance (Suppl. Material 2). Brittle and basket stars were frequently abundant and occurred characteristically on or within

https://doi.org/10.5194/egusphere-2026-6926
Preprint. Discussion started: 20 November 2026
© Author(s) 2026. CC BY 4.0 License.

gorgonian colonies (Suppl. Video 5, Fig. 14A, C). Other gorgonian-associated fauna included squat lobsters, king crabs, and sea stars, generally at low abundance, although squat lobsters were locally abundant (Suppl. Material 2). Sea urchins were occasionally observed on carbonate, whereas shrimp occurred at low abundance on adjacent soft sediment. Demersal fauna, including grenadiers, eelpouts, a catshark, and a *Bathyraja*-type skate, occurred sporadically at generally low abundance; a Humboldt squid was also observed (Suppl. Video 5).

Vesicomyid clams and shells occurred repeatedly on soft sediment, generally at low to medium abundance (Suppl. Video 5, Suppl. Material 2). In several observations, most visible clams appeared to consist of dead, empty shells. A localized occurrence of lamellibrachid tubeworms was observed at medium abundance on soft sediment with carbonate plates (Fig. 14D). Sulfur-oxidizing bacterial mats occurred locally at low to medium abundance on soft sediment and between small carbonate nodules and plates, indicating spatially restricted seep activity (Fig. 14B, D, E, F).

Authigenic Carbonates. A single carbonate piece was collected at 701.6 m from the lower level of a seep structure colonized by soft corals (Suppl. Material 3, P2+). One subsample (P2+ spec) was analyzed. The carbonate consisted of 29% aragonite, 21% calcite, and 18% dolomite. Its stable isotope composition ($\delta^{13}C$ = -46.03‰; $\delta^{18}O$ = 5.78‰) indicates precipitation from methane-influenced pore fluids (Table 2). U-Th data are not available.

Sediment Biogeochemistry. In Box-8, two seep habitats were sampled using ROV push cores (St. 74): sediment covered by a sulfur-oxidizing bacterial mat (PC-1, -12) and sediment inside a clam field (PC-5, -7) (Fig. 15). Several porewater geochemical profiles (sulfate, total alkalinity, Ca^{2+}) were similar in both shape and magnitude between the two habitats, exhibiting steep, concurrent gradients within the upper ~8 cm. In contrast, methane and sulfide profiles showed comparable concentration ranges but differed slightly in the depth of their maxima.

Methane oxidation rates, likely reflecting AOM based on the porewater signatures, were relatively low and similar in both habitats (approximately 10–40 nmol cm^{-3} d^{-1}), with little variation over depth. In contrast, sulfate reduction rates differed markedly. While rates in the uppermost centimeter were in the double-digit nmol cm^{-3} d^{-1} range at both sites, sulfate reduction beneath the mat increased sharply below 1 cm, reaching values one to two orders of magnitude higher (up to 493 nmol cm^{-3} d^{-1}) than those measured at equivalent depths beneath the clam field.

Previous studies of methane seeps typically report elevated AOM rates in sediments underlying sulfur-oxidizing bacterial mats compared to clam fields (Treude et al., 2003; Sommer et al., 2006). In this context, the similarity of porewater profiles between the two habitats, despite pronounced differences in sulfate reduction rates, is unexpected. It is also notable that AOM rates beneath the mat are substantially lower than the corresponding sulfate reduction rates. One possible explanation is methodological: AOM

https://doi.org/10.5194/egusphere-2026-6926
Preprint. Discussion started: 20 November 2026
© Author(s) 2026. CC BY 4.0 License.

rates may be underestimated if the $^{14}C–CH_4$ tracer was introduced while cores were still degassing following recovery, leading to partial tracer loss. This effect would not influence ^{35}S–sulfate tracer measurements. However, the reason for the overall similarity in porewater chemistry between the two habitats remains unresolved.

Methane in the water column. In Box-8, a single CTD cast (CTD-12) was conducted (Fig. 2). Methane concentrations ranged between 2 and 4 nmol L^{-1} in the upper 452 m of the water column. Below this depth, concentrations increased to 27–40 nmol L^{-1} down to 688 m, indicating methane input from the seafloor.

Two ROV-based Niskin samples collected over sulfur-oxidizing bacterial mats (St. 74; Fig. 5E; Table 3) exhibited the highest methane concentrations (52–63 nmol L^{-1}), further supporting active benthic methane release.

3.1.6 Reference Station

The reference station was selected in proximity to Box-3 but outside areas of active seepage and seafloor deformation, as indicated by geophysical data. One gravity core (St. 35) and one multicorer (St. 68) were recovered from this site.

Geochemical profiles from the gravity core revealed a deep SMTZ located between approximately 300 and 400 cm depth (Fig. 8 K-N). Methane concentrations increased with depth, reaching up to 1 mM at the base of the core (531 cm), and were accompanied by elevated sulfide concentrations, consistent with active AOM. Total alkalinity increased continuously with depth, while sulfate decreased from surface values to ~0.2 mM at and below 434 cm.

In contrast, multicorer samples representing the upper ~25–30 cm of the sediment exhibited largely uniform porewater profiles (Fig. 16). Sulfate, total alkalinity, and Ca^{2+} showed little to no variation with depth, and sulfide remained below detection. Methane concentrations were low (< 0.015 mmol L^{-1}) and displayed a weak subsurface maximum. Methane oxidation rates peaked in the upper 3 cm (1–11 nmol cm^{-3} d^{-1}) but were not accompanied by elevated sulfate reduction, suggesting that methane oxidation was likely coupled to oxygen and/or alternative electron acceptors such as nitrate. The slight enrichment of methane between 2 and 11 cm may indicate a contribution from methylotrophic (non-competitive) methanogenesis with coupled methane oxidation (Krause et al., 2023). Sulfate reduction rates were negligible in the uppermost centimeter and increased below, reaching a maximum of ~5 nmol cm^{-3} d^{-1} at 7–8 cm depth before declining slightly. As these rates were not associated with methane oxidation, sulfate reduction is more likely linked to organic matter degradation.

https://doi.org/10.5194/egusphere-2026-6926
Preprint. Discussion started: 20 November 2026
© Author(s) 2026. CC BY 4.0 License.

Together, these observations characterize background sediment biogeochemistry in the absence of advective fluid flow and methane seepage. The profiles are consistent with organic matter-driven diagenesis and a deep SMTZ (Treude et al., 2005b).

3.1.7 Carbon isotopic signatures of methane in sediment and water

Carbon isotopic signatures ($\delta^{13}C$) of methane in sediment-derived samples (gravity cores, multicorer samples, and ROV push cores) from Box-2 to Box-4 indicate a predominantly biogenic origin, with values ranging from −60.4 to −85.6 ‰ VPDB (Table 3; Whiticar (1999)). The most depleted values (down to −85.6 ‰) are consistent with methane production via hydrogenotrophic methanogenesis. Variability in $\delta^{13}C$ values within individual sediment cores likely reflects a combination of methane production, oxidation, and mixing processes.

In contrast, $\delta^{13}C$ values of methane from water column samples (ROV-based Niskin bottles) ranged from −57.0 to −63.8 ‰ VPDB and are thus consistently heavier and less variable than those observed in sediments. This pattern indicates that methane in the water column is derived from sedimentary biogenic sources but has undergone isotopic enrichment during transport. Microbial methane oxidation in both sediments and the water column preferentially consumes $^{12}CH_4$, leaving the residual methane isotopically heavier (Valentine et al., 2001; Biddle et al., 2012). The broader and more depleted isotopic range in sediment samples compared to the narrower and consistently heavier signatures in the water column further supports this interpretation. No isotopic signatures indicative of a thermogenic methane contribution were observed.

In addition, $\delta^{13}C$ values obtained from samples with low methane concentrations (30–63 nmol L^{-1}) should be interpreted with caution due to increased analytical uncertainty.

https://doi.org/10.5194/egusphere-2026-6926
Preprint. Discussion started: 20 November 2026
© Author(s) 2026. CC BY 4.0 License.

3.2 Synthesis and broader implications

3.2.1 Successional stages of methane seep ecosystems at the CMSA

The different CMSA seep locations investigated in this study (represented by Box-1, -2, -3, -4, -8) can be analyzed with respect to their life cycle of methane seep ecosystems using the five conceptual stages defined by Arrázola and Acosta (2024), which integrate geological development, hydrocarbon supply, biogeochemistry, microbial processes, and metazoan succession. The five stages defined are: 1. Birth, 2. Youth, 3. Maturity, 4. Senescence, and 5. Extinction. At Birth methane begins migrating from subsurface reservoirs toward the seafloor, while the characteristic AOM, sulfate reduction, and chemosynthetic communities of an established seep have not yet fully developed. Youth is characterized by increasing methane supply, development of a shallow SMTZ, strong AOM and sulfate reduction, sulfide production, sulfide-oxidizing mats, and establishment of chemosymbiotic fauna. Maturity represents maximum seep development, with extensive AOM, sulfide oxidation, chemosynthetic communities and substantial authigenic carbonate formation. Senescence involves declining hydrocarbon supply, increasingly carbonate-dominated seafloor, persistence of some chemosynthetic organisms, especially siboglinids, and increasing importance of non-seep heterotrophic fauna. Extinction follows cessation of hydrocarbon supply and disappearance of the remaining chemosynthetic ecosystem. Arrázola and Acosta (2024) specifically predict that extensive carbonate surfaces become increasingly important during maturity and senescence, eventually providing substrate for sessile organisms as the chemosynthetic community declines. Because methane seepage is spatially and temporally heterogeneous, different successional stages may coexist within the same seep system as fluid pathways shift and individual venting centers become active or inactive (Tryon et al., 2002; Teichert et al., 2003; Arrázola and Acosta, 2024).

Applying the conceptual framework of Arrázola and Acosta (2024) to the different habitats of the CMSA suggests that the investigated Boxes represent different stages in the life cycle of methane seep ecosystems (Table 5, Fig. 17a). Box-2 most closely represents the transition from birth to youth. The seafloor is almost entirely dominated by soft sediment and lacks extensive authigenic carbonate structures, while active methane seepage is expressed by sulfur-oxidizing bacterial mats, reduced sediments, chemosymbiotic clams, high sediment methane and sulfide concentrations, and locally high rates of methane oxidation and sulfate reduction. The establishment of AOM coupled to sulfate reduction and the resulting sulfide supply to surface microbial communities are characteristic of the youth stage of the model by Arrázola and Acosta (2024). Thus, although the absence of substantial carbonate development indicates a relatively early stage of seep evolution, the well-developed methane-dependent microbial processes and chemosynthetic communities suggest that Box-2 has already progressed beyond the initial birth stage.

https://doi.org/10.5194/egusphere-2026-6926
Preprint. Discussion started: 20 November 2026
© Author(s) 2026. CC BY 4.0 License.

Box-4 can be assigned to the youth stage but represents a more developed and particularly active seep habitat. Soft sediment still dominates the seafloor, although small carbonate nodules and occasional carbonate outcrops indicate that authigenic carbonate formation has become established. This interpretation is independently supported by the young ages of the sampled carbonates of 4.7 to 5.7 ka. The extensive Dead Clam Field provides additional evidence that a substantial chemosymbiotic community had become established during the development of the seep, even though most of the clams were no longer alive at the time of our investigation. At the same time, Box-4 contains some of the strongest indications of contemporary seepage observed in the CMSA, including sulfur-oxidizing bacterial mats, Lamellibrachid and frenulate tubeworms, high methane and sulfide concentrations, and exceptionally high rates of methane oxidation and sulfate reduction. The high methane concentrations immediately above the seafloor further demonstrate that methane supply locally exceeds consumption within the sediment. Collectively, these characteristics are consistent with an actively developing seep in which methane-driven biogeochemical processes and chemosynthetic communities are well established, while extensive carbonate structures have not yet developed.

Box-8 most closely corresponds to the maturity stage, although this assignment should be considered tentative because the spatial extent of the video surveys and number of samples from this Box were limited. In contrast to Boxes-2 and -4, the seafloor comprises a mixture of soft sediment and carbonate plates and locally larger carbonate structures. At the same time, active seepage remains evident from sulfur-oxidizing bacterial mats, clams, Lamellibrachid tubeworms, elevated methane concentrations, and substantial rates of methane oxidation and sulfate reduction. The coexistence of active chemosynthetic communities with increasingly developed carbonate habitat and carbonate-associated fauna is consistent with the maturity stage described by Arrázola and Acosta (2024).

Box-3 is interpreted as representing a predominantly senescent seep system. Here, massive and structurally complex authigenic carbonates constitute a major component of the seafloor, and the carbonate surfaces support abundant sessile and mobile fauna, including soft corals, serpulids, hydroids, sponges and echinoderms. These characteristics indicate a long history of seepage and extensive transformation from sediment to hard-substrate habitat. Nevertheless, Box-3 is clearly not inactive. Localized sulfur-oxidizing bacterial mats, clams and Lamellibrachid tubeworms occur among the older carbonate structures, and locally high methane oxidation rates demonstrate continued methane supply. Box-3 therefore illustrates an important characteristic of seep senescence: declining or spatially restricted seepage can coexist with substantial remnants of active chemosynthetic communities. In this respect, the Box also retains characteristics of a mature seep within an overall older, carbonate-dominated habitat.

Box-1 represents the most advanced ecological stage observed and is best classified as transitioning from senescence toward extinction. Massive carbonate boulders and crusts dominate the

https://doi.org/10.5194/egusphere-2026-6926
Preprint. Discussion started: 20 November 2026
© Author(s) 2026. CC BY 4.0 License.

seafloor, whereas soft sediment is scarce, and the carbonate structures are extensively colonized by non-seep sessile fauna, including soft corals, hydroids, sponges and brittle stars. Chemosynthetic communities are much less conspicuous than in the younger Boxes, although localized bacterial mats, clams and Lamellibrachid tubeworms, together with elevated methane concentrations immediately above the seafloor, demonstrate that seepage has not ceased completely. Box-1 therefore does not represent the extinction stage sensu Arrázola and Acosta (2024), which requires cessation of hydrocarbon supply and loss of the chemosynthetic ecosystem. Rather, it represents an advanced stage of senescence approaching extinction, in which the ecological importance of the carbonate structures as hard substrate has become increasingly prominent relative to active chemosynthesis.

Taken together, the five Boxes represent a spatial mosaic of seep habitats at different stages of development, ranging from actively reducing, sediment-dominated habitats with sulfur-oxidizing bacterial mats to old carbonate-dominated systems with increasingly restricted chemosynthetic activity (Table 5, Fig. 17a). This spatial distribution should not, however, be interpreted as a strictly chronological or unidirectional successional sequence. The coexistence of old carbonate structures with localized active seepage, particularly in Box-3, demonstrates that methane supply can persist within older seep systems and suggests that fluid pathways may shift or become reactivated over time (Fig. 17b). Thus, the stages identified here are best regarded as dominant ecological and biogeochemical states rather than successive stages through which individual seep locations necessarily progress.

Similar spatial mosaics occur at several well-studied seep systems, although they are not always interpreted explicitly in terms of successional stages. At Hydrate Ridge in the northeast Pacific Ocean, strongly active sediment-hosted seepage, extensive carbonate deposits, and spatially variable fluid-flow regimes coexist, while carbonate chronology demonstrates repeated episodes of seep activity over long timescales (Torres et al., 2002; Teichert et al., 2005; Tryon et al., 2002). At the Hikurangi Margin, a hypothetical successional model describes the transition from bacterial mats and ampharetid polychaete beds in soft sediments through clam and tubeworm communities to extensive carbonate structures increasingly colonized by non-chemosynthetic fauna (Bowden et al., 2013; Baco et al., 2010; Sommer et al., 2010). Ampharetid polychaetes are proposed to play an important role during early succession by modifying sediment biogeochemistry, potentially enhancing AOM and sulfide production and facilitating subsequent colonization by chemosymbiotic clams (Bowden et al., 2013). This progression closely resembles the habitat changes observed across the CMSA, although the prominent tube-dwelling polychaetes observed in Box-2 could not be identified as ampharetids. Episodic and spatially shifting fluid discharge is also documented at Costa Rican margin seeps, where active and apparently inactive carbonate habitats can occur within the same seep systems and carbonate records indicate repeated phases of fluid venting (Kutterolf et al., 2008; Levin et al., 2015). Thus, the coexistence of seep habitats at

https://doi.org/10.5194/egusphere-2026-6926
Preprint. Discussion started: 20 November 2026
© Author(s) 2026. CC BY 4.0 License.

different stages of development is not restricted to the CMSA. What makes the CMSA particularly informative is the clear representation of different successional stages across closely spaced seep habitats, particularly Boxes 1, 2, 4, and 8, which occur within only a few kilometers of one another, with the more distant Box-3 extending this range of seep stages farther north. Rather than being exceptional in the processes involved, the CMSA provides a particularly well-developed example of the spatial and temporal heterogeneity that characterizes long-lived methane seep systems.

3.2.2 Seep communities as indicators of subsurface biogeochemistry

The distribution of chemosynthetic communities at methane seeps is closely linked to methane supply and the resulting sediment biogeochemistry. Upward methane transport stimulates AOM, producing sulfide that supports sulfur-oxidizing microorganisms and thiotrophic symbioses. Differences in methane and fluid flux and in the depth and intensity of AOM and sulfate reduction can therefore be reflected in distinct seafloor communities (Sahling et al., 2002; Torres et al., 2002; Treude et al., 2003; Boetius and Suess, 2004; Fischer et al., 2012). This relationship is particularly well documented at Hydrate Ridge, where sulfur-oxidizing bacterial mats occupied areas of high sulfide and methane flux, vesicomyid clams occurred under substantially lower flux, and solemyid clams occupied peripheral habitats with low sulfide availability (Sahling et al., 2002; Torres et al., 2002; Treude et al., 2003; Sommer et al., 2006; Tryon et al., 2002). Methane fluxes of 30 to 90 mmol m^{-2} d^{-1} were estimated for mat-covered sites compared with <1 mmol m^{-2} d^{-1} at clam sites, while fluid transport varied strongly over short spatial scales and through time.

This relationship is particularly evident for sulfur-oxidizing bacterial mats and adjacent black sediments in Box-2. Mat-covered sediments contained high concentrations of methane and sulfide and showed some of the highest AOM and sulfate reduction rates measured in this Box (Fig. 7). Sulfide extended close to the sediment-water interface, providing the reduced substrate required by sulfur-oxidizing bacteria, while mat-rich sediments showed shallower oxygen penetration and approximately twofold higher diffusive oxygen uptake than sediments with less mat coverage. Similar associations between bacterial mats, high methane supply, shallow sulfide, and elevated methane turnover have been observed at other methane seeps (Sahling et al., 2002; Treude et al., 2003; Joye et al., 2004; Niemann et al., 2006; Fischer et al., 2012). The black sediment patches observed in Box-2 likely represent a related but geochemically distinct condition (Fig. 6 C, G, I). Here, sulfide produced by sulfate reduction, largely fueled by AOM, may be consumed through reaction with reactive iron before free sulfide accumulates sufficiently to support conspicuous sulfur-oxidizing bacterial mats (Fig 7 A, B, E). Precipitation of iron sulfides would account for the characteristic black coloration. A similar decoupling between high sulfate reduction activity and detectable free sulfide has been observed in organic-rich sediments at a deep-sea

https://doi.org/10.5194/egusphere-2026-6926
Preprint. Discussion started: 20 November 2026
© Author(s) 2026. CC BY 4.0 License.

whale fall, where sulfate reduction was primarily fueled by degradation of whale-derived organic matter rather than methane (Treude et al., 2009). Thus, the transition from black reduced sediments to white bacterial mats in Box-2 may reflect whether sulfide production exceeds its consumption within the sediment, allowing free sulfide to reach the sediment-water interface.

Chemosymbiotic clams provide a somewhat different indication of subsurface conditions. Vesicomyid communities at Hydrate Ridge occurred outside bacterial-mat-dominated habitats and were associated with lower methane and fluid flux and deeper sulfide availability (Sahling et al., 2002; Torres et al., 2002; Treude et al., 2003). Importantly, clams are not merely passive indicators of these conditions. Burrowing, irrigation, and pumping can enhance the transport of sulfate- and oxygen-containing bottom water into the sediment, promoting microbial turnover and sulfide production (Treude et al., 2003; Wallmann et al., 1997; Fischer et al., 2012). The living clam communities at the CMSA were broadly consistent with this pattern. In Box-3, clam-associated sediments showed AOM and sulfate reduction rates of up to 177 and 68 nmol cm^{-3} d^{-1} (Fig. 10 A, B), respectively, whereas AOM beneath the Box-8 clam field was lower, approximately 10–40 nmol cm^{-3} d^{-1}, with sulfate reduction remaining in the double-digit range (Fig. 15 A, B). Box-4 represents a fundamentally different situation because the predominantly dead clam shells record a previous ecological state rather than contemporary conditions. The underlying sediments nevertheless showed some of the highest AOM and sulfate reduction rates at the CMSA, together with high methane and sulfide concentrations, a shallow sulfate-methane transition, and exceptionally high total oxygen uptake. Thus, the ecological framework derived from living clam communities cannot be directly applied to the Dead Clam Field, where the shells instead document conditions suitable for clams at an earlier stage of seep development (see Section 3.2.4).

Lamellibrachid and frenulate tubeworms represent another relationship between visible communities and subsurface geochemistry. Siboglinid tubeworms harbor sulfide-oxidizing symbionts and can access sulfide below the sediment surface, allowing them to persist where free sulfide does not reach the sediment-water interface (Cordes et al., 2009). Their occurrence across several CMSA habitats therefore indicates access to reduced sulfur but does not necessarily imply the high near-surface sulfide flux associated with bacterial mats. Tubeworm activity can, in turn, modify sediment redox conditions through bioirrigation, demonstrating that these organisms can both respond to and influence subsurface biogeochemistry (Melaniuk et al., 2022; Sommer et al., 2009). This interaction may help explain the unusually high near-surface methane oxidation rates in the Lamellibrachia field in Box-3 (Fig. 10 A, B) and the frenulate tubeworm field in Box-4 (Fig. 12 A, B), which were accompanied by little sulfate reduction. A similar pattern was observed in a Siboglinidae field at Vestnesa Ridge, where methane oxidation reached 196 nmol cm^{-3} d^{-1} in the uppermost sediment but was decoupled from sulfate reduction (Melaniuk et al., 2022). Bioirrigation maintained oxidized surface sediments, and methane oxidation in

https://doi.org/10.5194/egusphere-2026-6926
Preprint. Discussion started: 20 November 2026
© Author(s) 2026. CC BY 4.0 License.

this interval was attributed primarily to aerobic methanotrophy, whereas deeper methane oxidation was consistent with AOM. Aerobic methane oxidation was also inferred for low-flux solemyid clam habitats at Hydrate Ridge, where near-surface methane oxidation was associated with little sulfate reduction (Treude et al., 2003). These observations strongly support aerobic methane oxidation as an explanation for the high surface methane oxidation rates and low sulfate reduction measured in the CMSA tubeworm fields.

Overall, the CMSA observations support the close relationship between chemosynthetic community type and sediment biogeochemistry established at other methane seeps. Local deviations among methane oxidation, sulfate reduction, and porewater methane and sulfide profiles appear to reflect the strong small-scale heterogeneity of seepage and the influence of the organisms themselves on sediment biogeochemistry. Fluid and methane fluxes can vary substantially over short distances and through time because of changes in permeability, gas transport, and shifting flow pathways (Torres et al., 2002; Tryon et al., 2002). Consequently, individual sediment cores may not always capture the full biogeochemical conditions represented by a visible chemosynthetic community.

Beyond the conspicuous chemosynthetic communities, the CMSA carbonate structures supported abundant hydroids, soft corals, sponges, serpulids, and echinoderms (Figs. 4, 9, 11, 14; Suppl. Video 1-4). These organisms should not generally be considered direct indicators of active methane seepage. However, recent studies have demonstrated that taxa traditionally considered non-chemosymbiotic, including some observed at seep habitats in our study, can establish nutritional associations with chemosynthetic microorganisms. Methanotrophic symbionts can contribute substantially to the nutrition of seep-associated serpulid and sabellid worms, while associations with sulfur-oxidizing bacteria have been demonstrated in deep-sea anemones (Goffredi et al., 2021; Goffredi et al., 2020). More recently, a cold-water coral inhabiting a methane seep was shown to associate with thiotrophic and potentially methanotrophic bacteria and to incorporate chemosynthetically derived carbon, suggesting a facultative nutritional association with seep microorganisms (Stabbins et al., 2026). These findings raise the possibility that some of the apparently non-chemosynthetic fauna at the CMSA may also benefit directly from microbial chemosynthesis. We have no evidence for such associations in the CMSA specimens, however, and resolving this possibility would require targeted microbiological, molecular, and isotopic analyses beyond the scope of this study. The carbonate-associated fauna should therefore primarily be interpreted as a response to the physical habitat created by seepage (see Section 3.2.5), while recognizing that presently unresolved trophic associations with chemosynthetic microorganisms cannot be excluded.

Overall, the CMSA communities provide useful indicators of subsurface biogeochemical conditions, but not simple quantitative proxies for methane flux. Sulfur-oxidizing bacterial mats most directly indicate shallow sulfide production and high methane supply, whereas clams and tubeworms can

https://doi.org/10.5194/egusphere-2026-6926
Preprint. Discussion started: 20 November 2026
© Author(s) 2026. CC BY 4.0 License.

exploit reduced substrates deeper within the sediment and actively modify their biogeochemical environment. Strong small-scale spatial heterogeneity in fluid flow can nevertheless cause individual sediment cores to capture only part of the biogeochemical conditions represented by a visible chemosynthetic community.

3.2.3 Authigenic carbonates as records of seep evolution

Authigenic carbonates provide a long-term archive of methane seepage because AOM increases alkalinity and promotes carbonate precipitation where methane-rich fluids interact with sulfate-bearing seawater or porewater. Their mineralogy, fabrics, stable isotope composition, and ages can therefore preserve information on past methane sources, fluid pathways, and seepage intensity (Teichert et al., 2005; Smrzka et al., 2025; Naehr et al., 2000; Han et al., 2008; Greinert et al., 2001; Bohrmann et al., 1998; Liebetrau et al., 2014; Leefmann et al., 2008; Liebetrau et al., 2010). The strongly negative $\delta^{13}C$ values of the CMSA carbonates, reaching approximately −46‰ (Table 2), confirm a major contribution of methane-derived carbon and are similar to seep carbonates reported from other active continental margins. The predominance of aragonite in many CMSA samples is also characteristic of carbonate precipitation in shallow, sulfate-rich zones at methane seeps, although carbonate mineralogy is influenced by fluid chemistry, saturation state, Mg/Ca ratios, microbial processes, and subsequent diagenesis (Greinert et al., 2001; Bohrmann et al., 1998; Mavromatis et al., 2014).

Carbonate abundance and U-Th ages at the CMSA broadly correspond to the relative seep stages inferred from seafloor observations (Tables 2 and 5). Box-2, representing the earliest developmental stage among the investigated seep habitats, is dominated by soft sediment and lacks the extensive carbonate structures of the older habitats. Box-4 remains predominantly sediment-covered but contains carbonate nodules and plates, with reliable ages of 4.7 ± 0.1 and 5.7 ± 0.2 kyr BP. In contrast, the advanced-senescent Box-1 is dominated by massive carbonate banks, pavements, veins, and former fluid conduits with ages of approximately 50 to 168 kyr BP, most between 50 and 95 kyr BP. This progression from sediment-hosted seepage through habitats with relatively young carbonates to massive, old carbonate structures supports the use of carbonate development as a first-order visual indicator of relative seep development stage. Extensive chemoherms similarly record prolonged or repeated methane seepage at Hydrate Ridge and elsewhere along the central Chile margin (Teichert et al., 2005; Klaucke et al., 2012). A similar relationship between carbonate age and habitat development was observed at the Hikurangi Margin, where older carbonate structures were generally associated with non-chemosynthetic fauna, including cold-water corals, whereas younger carbonate habitats supported more abundant chemosynthetic communities (Liebetrau et al., 2010; Bowden et al., 2013).

https://doi.org/10.5194/egusphere-2026-6926
Preprint. Discussion started: 20 November 2026
© Author(s) 2026. CC BY 4.0 License.

However, carbonate age cannot be equated with the age of a seep. Carbonate precipitation is spatially heterogeneous and episodic as methane flux and fluid pathways change, and individual structures can record multiple phases of growth separated by periods of reduced activity (Liebetrau et al., 2014; Liebetrau et al., 2010; Kutterolf et al., 2008; Teichert et al., 2003) (Fig. 17b). Forearc seep systems can remain active for several hundred thousand years while alternating between active and quiescent phases, and neighboring seep structures may follow different histories (Kutterolf et al., 2008). Carbonates may also occur outside the location of the contemporary AOM zone, preserving former fluid pathways after subsurface flow has shifted (Mavromatis et al., 2014). Thus, a U-Th age dates a particular episode of carbonate precipitation rather than the initiation, duration, or termination of seepage.

Box-3 emphasizes an additional limitation. Its massive carbonates are consistent with a long-developed seep system, but apparent ages exceeding 150 kyr and extending to several hundred thousand years should be treated cautiously because several subsamples show evidence of open-system behavior. Post-depositional uranium exchange with pore fluids can disturb U-Th systematics, while seep fluids may themselves carry uranium isotope compositions different from seawater (Teichert et al., 2003; Liebetrau et al., 2014). In contrast, the Box-4 carbonates have high $^{238}U/^{232}Th$ ratios, initial $\delta^{234}U$ values close to seawater, small analytical uncertainties, and similar ages in two subsamples, supporting their approximately 5 to 6 kyr chronology. U-Th ages of seep carbonates therefore need to be evaluated together with their isotope systematics and petrographic context rather than from analytical uncertainty alone.

Importantly, exposed seep carbonates should not necessarily be regarded as biogeochemically inactive remnants of past seepage. Methane-oxidizing archaea and sulfate-reducing partners can inhabit pore spaces within seep carbonates, and active AOM has been demonstrated within well-lithified carbonate rocks, allowing methane oxidation and sulfide production to continue after carbonates become exposed at the seafloor (Marlow et al., 2014; Case et al., 2015; Mayr et al., 2025). Carbonate-hosted AOM could therefore potentially sustain sulfur-oxidizing and chemosymbiotic communities where methane continues to migrate through older carbonate structures. We did not measure microbial activity within CMSA carbonates and therefore cannot determine whether this process occurred here. Nevertheless, the occurrence of sulfur-oxidizing bacterial mats directly on or within carbonate structures, particularly in Boxes 1 and 3 (Figs. 4C, F and 9C), is consistent with continued delivery of reduced compounds through these old carbonate systems and makes carbonate-hosted AOM a plausible mechanism.

Overall, the CMSA carbonates support the relative seep evolution inferred visually, particularly the progression from the largely sediment-hosted Box-2 through relatively young carbonates in Box-4 to the extensive old carbonate structures of Boxes 1 and 3. Authigenic carbonates therefore provide a

https://doi.org/10.5194/egusphere-2026-6926
Preprint. Discussion started: 20 November 2026
© Author(s) 2026. CC BY 4.0 License.

cumulative and discontinuous archive of seepage rather than a direct age of the seep ecosystem. Their extent and morphology can provide useful information on relative seep development, but numerical ages record individual episodes of carbonate formation and must be interpreted in the context of episodic fluid flow, possible diagenetic alteration, and potentially continuing methane cycling within older carbonate structures.

3.2.4 Tectonic control of seepage and ecological disturbance at the Box-4 Dead Clam Field

The Dead Clam Field in Box-4 represents a striking mismatch between the visible seep community and contemporary biogeochemical activity. The seafloor was densely covered by predominantly open, articulated Vesicomyid shells, indicating the former presence of a substantial chemosymbiotic clam community, whereas only a few closed or upright individuals could potentially have been alive (Fig. 11). In contrast, the underlying sediment remained highly active, with AOM and sulfate reduction reaching 856 and 1946 nmol cm^{-3} d^{-1}, respectively, methane concentrations of up to 3.1 mM, sulfide concentrations of up to 17.4 mM, and a shallow sulfate-methane transition in the top 6-8 cm of the sediment (Fig. 12). Thus, the decline of the clam community cannot simply be explained by cessation of methane seepage. Extensive accumulations of dead vesicomyid shells, accompanied by few living clams, have also been documented at the Hikurangi Margin and interpreted as evidence of former chemosymbiotic communities affected by changes in fluid supply (Bowden et al., 2013). The CMSA Dead Clam Field provides an important additional perspective, demonstrating that the decline of a clam community can coincide with exceptionally high contemporary rates of methane oxidation and sulfate reduction.

Benthic oxygen consumption provides an additional, integrated measure of the intense contemporary biogeochemical activity in the Dead Clam Field. Total oxygen uptake reached 38.9 mmol m^{-2} d^{-1}, substantially exceeding the oxygen uptake measured in Box-2, where diffusive oxygen uptake ranged from 9.1 to 16.4 mmol m^{-2} d^{-1} and eddy correlation yielded a mean of 9.1 mmol m^{-2} d^{-1} (Table 4). The more moderate oxygen demand in Box-2 is consistent with its interpretation as a comparatively controlled birth-to-youth seep, characterized by spatially restricted methane cycling and sulfide production. In contrast, the exceptionally high oxygen consumption in the Dead Clam Field is consistent with the much greater methane-driven biogeochemical activity observed in Box-4. Methane seeps can exhibit high oxygen demand because methane oxidation and the reoxidation of reduced products generated during AOM, particularly sulfide, consume oxygen at and near the sediment-water interface (Sommer et al., 2006; Boetius and Wenzhöfer, 2013). In Box-4, the scarcity of living macrofauna, together with high methane oxidation and sulfate reduction rates and substantial subsurface sulfide production, suggests that much of this oxygen demand was associated with chemical and microbial

https://doi.org/10.5194/egusphere-2026-6926
Preprint. Discussion started: 20 November 2026
© Author(s) 2026. CC BY 4.0 License.

oxidation of reduced compounds rather than faunal respiration. This contrasts with seep habitats where dense macrofaunal communities can account for a substantial fraction of total oxygen consumption (Sommer et al., 2010).

A possible explanation emerges from the tectonic setting and timing of our observations. Box-4 was investigated only about seven months after the Mw 8.8 Maule earthquake of 27 February 2010, within its rupture area. The CMSA is located above major upper-plate faults, and juvenile extensional fractures observed during the same expedition indicate recent deformation. Coulomb stress modeling suggests that the Maule earthquake produced coseismic extension in this part of the marine forearc, potentially reactivating and dilating upper-plate faults and increasing their permeability (Geersen et al., 2016). This could allow pulses of methane-rich fluids to migrate toward the seafloor along newly opened or reactivated pathways (Fig. 17b).

The decimeter-scale cracks and fractures observed in the vicinity of the Dead Clam Field are particularly intriguing in this context (Fig. 11E; Suppl. Video 4). Sulfur-oxidizing bacterial mats occurred along some of these structures, while sediments within the nearby Dead Clam Field contained high methane and sulfide concentrations and exceptionally high AOM and sulfate reduction rates (Fig. 12). Together, these observations are consistent with spatially focused methane transport through a tectonically controlled and heterogeneous plumbing system. Similar relationships between tectonic activity and methane discharge have been observed at other active margins. Earthquakes can change fault permeability, pore-fluid pressure, and migration pathways, potentially redistributing or enhancing seafloor methane discharge (Gasperini et al., 2012; Fischer et al., 2013; Geersen et al., 2016).

Such changes in seepage can directly affect chemosynthetic communities. This connection has recently been demonstrated at Mound 12 on the Costa Rican margin, where surveys before and after a Mw 6.5 earthquake revealed substantial shifts in the locations of active seepage (Cowell et al., 2026). Symbiotic species distributions were disrupted, while mobile vesicomyid clams appeared to relocate and track newly established seepage conditions, demonstrating that tectonically induced changes in fluid flow can reorganize seep communities over short timescales. This study provides a particularly relevant modern analogue for Box-4. More generally, the strong dependence of vesicomyid communities on the magnitude and spatial distribution of methane and sulfide flux makes them sensitive to changes in subsurface fluid pathways (Tryon et al., 2002; Treude et al., 2003; Torres et al., 2002; Sahling et al., 2002).

The available evidence nevertheless does not demonstrate that the 2010 Maule earthquake caused the mortality of the Box-4 clams. The age of the shell accumulation is unknown. The ^{210}Pb profiles indicate recent sediment mixing and thus recent bioturbation (Fig. 13), which could plausibly have involved clams, but they cannot identify the organisms responsible or establish when the clam community

https://doi.org/10.5194/egusphere-2026-6926
Preprint. Discussion started: 20 November 2026
© Author(s) 2026. CC BY 4.0 License.

declined. Furthermore, methane seepage clearly preceded the earthquake, including gas flares observed in 2008 (Klaucke et al., 2012). Repeated large earthquakes may instead periodically reactivate or dilate existing fluid pathways, while seepage persists at varying intensity throughout the seismic cycle (Geersen et al., 2016).

The Dead Clam Field therefore illustrates how tectonic forcing could potentially decouple the biological appearance of a seep from its contemporary biogeochemical state. We propose that earthquake-related deformation and changes in fault permeability may have reorganized fluid pathways at Box-4, potentially disturbing an established clam community while maintaining or enhancing methane supply and AOM. However, a direct causal relationship between the 2010 Maule earthquake and clam mortality cannot be established.

3.2.5 Integration of the CMSA seeps into the surrounding deep-sea ecosystem

Although cold seeps support specialized chemosynthetic communities, their ecological influence extends well beyond seep-dependent fauna. Seep-generated hard substrates, habitat heterogeneity, chemosynthetic production, and biogenic structures can provide attachment surfaces, shelter, food, and other resources for the surrounding deep-sea community (Levin et al., 2016). This broader ecological integration is clearly expressed at the CMSA, where authigenic carbonate structures support diverse assemblages of corals, hydroids, sponges, serpulids, anemones, and other sessile fauna not restricted to methane seeps (Sellanes et al., 2008) (Fig. 4 A, B, C, H; Fig. 9 A, C, E; Fig. 11 D; Fig. 14 A, C, E). At the same time, numerous mobile organisms, including fish, Humboldt squid, octopuses, crustaceans, and echinoderms, were observed within the seep habitats (Fig. 4 G, Fig. 6 D, E, H, I; Fig 9. D, E, I; Fig. 11 E, F, H; Fig. 14 C, D, E, F). Their occurrence further illustrates the ecological continuity between the CMSA and the surrounding deep-sea community, although our observations do not establish whether individual mobile taxa were specifically attracted to seep-related resources.

The extensive carbonate structures are particularly important because their ecological function can persist beyond periods of strong methane discharge. In an otherwise predominantly sedimentary environment, carbonate boulders, crusts, and chemoherms create three-dimensional habitat, providing attachment surfaces, elevated positions, crevices, and refuges. Similar associations of background deep-sea fauna with seep carbonates have been observed elsewhere, and increasing representation of non-seep fauna as seepage declines demonstrates that the physical legacy of seepage can continue to structure benthic communities after chemosynthetic activity has diminished (Levin et al., 2016; Levin et al., 2010; Lee et al., 2025). A particularly striking example of this habitat function at the CMSA is the occurrence of skate egg capsules in protected spaces between large carbonate boulders in Box-1, indicating that the structural

https://doi.org/10.5194/egusphere-2026-6926
Preprint. Discussion started: 20 November 2026
© Author(s) 2026. CC BY 4.0 License.

complexity created by seep carbonates can provide nursery habitat for deep-sea predators (Treude et al., 2011) (Fig. 4 H).

The ecological integration of the CMSA also includes trophic connections between seep-derived production and the surrounding fauna. Stable-isotope evidence indicates that methane-derived carbon contributes to the nutrition of some non-chemosymbiotic taxa at the CMSA, although photosynthetically derived organic matter remains the dominant carbon source for most species (Zapata-Hernández et al., 2014). This demonstrates that seep-derived carbon can enter food webs beyond the characteristic chemosynthetic communities.

Previous studies indicate that the broader ecological functions of methane seeps may also extend to commercially important species. Patagonian toothfish (*Dissostichus eleginoides*) showed significantly higher catches and fishing yields at the CMSA than at a nearby control site, potentially reflecting enhanced prey availability and habitat heterogeneity associated with seep carbonates (Sellanes et al., 2012). Similar associations of commercially important fishes with methane-seep habitats have recently been documented elsewhere along the Chilean margin. At the El Quisco seep off central Chile, large numbers of the commercially important Congrio Colorado (*Genypterus chilensis*) were observed congregating within Lamellibrachia tubeworm bushes, with 46–48 individuals recorded on a single large tubeworm mound at 434–438 m water depth (Levin et al., 2025). Many individuals had tunneled into the dense tubeworm aggregation with only their heads protruding, suggesting that the three-dimensional structure created by the tubeworms may provide habitat or refuge.

The ecological influence of the CMSA seeps may also extend beyond the benthic seep habitats through the overlying water column. Clear near-bottom methane enrichment occurred in Boxes 1, 2, 4, and 8, demonstrating that a fraction of the methane supplied to these seep habitats escaped benthic consumption and entered the water column (Fig. 5, Table 3). In contrast, no distinct near-bottom enrichment was detected in Box-3 despite active methane cycling within the sediments, indicating that substantial benthic methane turnover does not necessarily result in a detectable water-column methane signal. The highest methane concentrations were generally measured by ROV-operated Niskin bottles directly above active seep habitats and substantially exceeded concentrations measured during CTD casts, demonstrating that methane enrichment can be highly localized immediately above the seafloor. This heterogeneity was particularly pronounced in Box-4, where methane concentrations determined from closely spaced CTD casts above the Dead Clam Field ranged from <10 to 167 nmol L^{-1} near the seafloor, whereas targeted ROV sampling above a sulfur-oxidizing bacterial mat reached methane concentrations of 3776 nmol L^{-1}. The large difference between targeted near-seafloor sampling and conventional CTD casts suggests that even strong but spatially restricted methane release may be missed or substantially underestimated by discrete water-column sampling. Such variability is consistent with rapid dilution and

https://doi.org/10.5194/egusphere-2026-6926
Preprint. Discussion started: 20 November 2026
© Author(s) 2026. CC BY 4.0 License.

lateral transport of seep-derived methane by bottom-water circulation, which can strongly influence both methane distributions and pelagic methane oxidation (Valentine et al., 2001; Steinle et al., 2015). Methane escaping the benthic filter can support aerobic methanotrophs in the water column, while rising gas bubbles can also transport these microorganisms from the sediment into the water, extending methane-driven microbial processes beyond the immediate seep habitat (Tavormina et al., 2010; Tavormina et al., 2008; Niemann et al., 2015; Klonicki-Ference et al., 2026; Jordan et al., 2021). Recent observations of methane oxidation and methanotrophs hundreds of meters beyond active seep zones have led to the concept of an expanded pelagic "methanosphere" surrounding cold seeps (Klonicki-Ference et al., 2026). We hypothesize that a similar methanosphere may occur at the CMSA and that dispersal of methanotrophic biomass could provide an additional pathway by which methane-derived carbon enters the surrounding deep-sea food web.

Together, these observations show that the ecological footprint of the CMSA extends well beyond its characteristic chemosynthetic communities. Seepage creates persistent three-dimensional habitat, contributes methane-derived carbon to surrounding food webs, provides refuge and nursery habitat, and releases methane into the overlying water column, potentially extending seep influence beyond the benthic habitat through a broader methanosphere. The CMSA therefore represents not an isolated chemosynthetic ecosystem, but a habitat closely connected to the surrounding deep-sea ecosystem through physical and trophic pathways, highlighting the broader ecological importance and ecosystem services of methane seeps (Thurber et al., 2014).

https://doi.org/10.5194/egusphere-2026-6926
Preprint. Discussion started: 20 November 2026
© Author(s) 2026. CC BY 4.0 License.

4. Conclusions

The Concepción Methane Seep Area represents a spatially heterogeneous and long-lived seep system in which different stages of seep development coexist in proximity. Sediment-dominated habitats with intense methane cycling and well-developed chemosynthetic communities occur alongside mature and senescent carbonate systems that retain localized active seepage. The CMSA therefore illustrates that seep succession is not necessarily a simple progression from initiation to extinction but may involve spatial and temporal shifts in methane supply and fluid pathways.

The distribution and composition of chemosynthetic communities largely reflect methane supply and the resulting biogeochemical conditions, particularly sulfide production through AOM. Community type can therefore provide an indication of relative methane flux and subsurface biogeochemical conditions, although small-scale heterogeneity in fluid flow and modification of sediment biogeochemistry by the organisms themselves can introduce local variability.

At the tectonically active central Chile margin, changes in fault permeability and fluid pathways provide a potential mechanism for repeatedly modifying methane supply and, consequently, seep communities. Periodic tectonic reactivation could potentially renew methane delivery to older seep structures before seepage ceases completely, offering one possible explanation for the absence of a clearly extinct seep among the investigated CMSA habitats. Although speculative, this possibility suggests that seep evolution at active continental margins may be closely coupled to tectonic processes rather than following a unidirectional ecological succession.

Finally, the ecological influence of the CMSA extends beyond its characteristic chemosynthetic communities. Seep-generated carbonate structures provide persistent habitat, refuge, and nursery grounds, while methane-derived carbon contributes to surrounding food webs. Methane escaping the benthic filter further extends seep influence into the overlying water column, where it can support pelagic methanotrophy and potentially disperse methane-derived microbial biomass beyond the immediate seep habitat. Together, these physical and trophic connections demonstrate that the CMSA is closely integrated into the surrounding deep-sea ecosystem and suggest that the seeps may contribute to regional biodiversity and ecosystem functioning, including by providing habitat and foraging opportunities for commercially important species.

https://doi.org/10.5194/egusphere-2026-6926
Preprint. Discussion started: 20 November 2026
© Author(s) 2026. CC BY 4.0 License.

5. Data Availability

Data are available in the PANGAEA database under the following reference and DOI:
Linke, Peter; Treude, Tina; Liebetrau, Volker; Scholz, Florian; Steeb, Philip; Geersen, Jacob; Schmidt, Mark; Sommer, Stefan; Rovelli, Lorenzo; Bryant, Lee D (2026): A comprehensive geomorphological, biogeochemical and ecological dataset from SONNE cruise SO210 off central Chile [dataset bundled publication]. PANGAEA, https://doi.org/10.1594/PANGAEA.989420

6. Video Supplement

Video 1-5 can be downloaded from the PANGEA database following these individual DOIs:
Video 1 (Box-1): https://doi.pangaea.de/10.1594/PANGAEA.997829
Video 2 (Box-2): https://doi.pangaea.de/10.1594/PANGAEA.997832
Video 3 (Box-3): https://doi.pangaea.de/10.1594/PANGAEA.997833
Video 4 (Box-4): https://doi.pangaea.de/10.1594/PANGAEA.997834
Video 5 (Box-8): https://doi.pangaea.de/10.1594/PANGAEA.997835

7. Supplement Link

8. Statement on the Use of Artificial Intelligence

Artificial intelligence (ChatGPT) was used to assist with habitat characterization (see Section 2.2.2 for methodological details), literature searches, revision of text originally drafted by the authors, and final checks of manuscript formatting and consistency. In addition, the graphical abstract (Fig. 17) was generated using ChatGPT based on materials and prompts provided by the authors and subsequently reviewed and refined by the authors to correct graphical inaccuracies.

8. Author Contribution

TT, PL, VL, and MS contributed to the conceptualization of the project, funding acquisition, and project administration. PL served as chief scientist during R/V SONNE expedition SO210 and supervised the fieldwork. All authors contributed to the investigation, data curation, and validation. TT prepared the original manuscript draft, and all co-authors except VL (deceased) contributed to its review and editing.

9. Competing Interests

Some authors are members of the editorial board of Biogeosciences.

10. Special Issue Statement

https://doi.org/10.5194/egusphere-2026-6926
Preprint. Discussion started: 20 November 2026
© Author(s) 2026. CC BY 4.0 License.

Pending

11. Acknowledgments

We dedicate this work to the memory of our dear colleague and co-author Volker Liebetrau, who sadly passed away before completion of this manuscript. We thank Erna Lange, Christine Utecht, and the GEOMAR Technology and Logistics Centre for logistical support before and during the expedition. We are grateful to Captain Lutz Mallon, the crew of R/V SONNE, the ROV Kiel 6000 team, and the scientific party for their professional collaboration and support. Technical assistance onboard was provided by Bernhard Bannert, Sergiy Cherednichenko, Sonja Kriwanek, Asmus Petersen, Wolfgang Queisser, Ralf Schwarz, and Matthias Türk. Porewater analyses were supported by Bettina Domeyer, Anke Bleyer, Regina Surberg, and Ulrike Schroller-Lomnitz, and methane analyses by Peggy Wefers and Andrea Bodenbinder. We further thank Sascha Flögel for providing the POZ-Landers. We thank Marion Liebetrau and Frank Maguhn for their support with carbonate data recovery, and Jan Fietzke for assistance with data interpretation. We also thank Carsten Schirnick for assistance with video timecoding and Nikolas Linke for editing the ROV videos. The GEOMAR data management team (Hela Mehrtens, Ulrike Schroller-Lomnitz, and Barbara Glemser) provided significant support for uploading the data on PANGAEA.

10. Financial Support

Expedition SO210 with R/V Sonne was conducted within the framework of the Collaborative Research Centre (SFB) 574 “Volatiles and Fluids in Subduction Zones” at Kiel University, funded by the Deutsche Forschungsgemeinschaft (DFG). ROV operations were supported by GEOMAR. Jacob Geersen was funded by the Cluster of Excellence “The Future Ocean” (grant CP1404), supported by the DFG within the German Excellence Initiative. Data management for SO210 (Peter Linke) was funded by the Helmholtz Association (HGF) Data Hub.

https://doi.org/10.5194/egusphere-2026-6926
Preprint. Discussion started: 20 November 2026
© Author(s) 2026. CC BY 4.0 License.

References

Abegg, F. and Linke, P.: Remotely Operated Vehicle "ROV KIEL 6000 ", Journal of large-scale research facilities JLSRF, 3, http://dx.doi.org/10.17815/jlsrf-3-160, 2017.

Angermann, D., Klotz, J., and Reigber, C.: Space-geodetic estimation of the Nazca-South America Euler vector, Earth and Planetary Science Letters, 171, 329-334, 10.1016/S0012-821X(99)00173-9, 1999.

Arrázola, J. and Acosta, A.: Conceptual representation of the life cycle of methane seep ecosystems, Marine Biology Research, 20, 380-400, https://doi.org/10.1080/17451000.2024.2392740, 2024.

Baco, A. R., Rowden, A. A., Levin, L. A., Smith, C. R., and Bowden, D. A.: Initial characterization of cold seep faunal communities on the New Zealand Hikurangi margin, Marine Geology, 272, 251-259, https://doi.org/10.1016/j.margeo.2009.06.015, 2010.

Berg, P., Røy, H., and Wiberg, P. L.: Eddy correlation flux measurements: The sediment surface area that contributes to the flux, Limnology and Oceanography, 52, 1672-1684, https://doi.org/10.4319/lo.2007.52.4.1672, 2007.

Berndt, C., Feseker, T., Treude, T., Krastel, S., Liebetrau, V., Niemann, H., Bertics, V. J., Dumke, I., Dünnbier, K., Ferré, B., Graves, C., Gross, F., Hissmann, K., Hühnerbach, V., Krause, S., Lieser, K., Schauer, J., and Steinle, L.: Temporal constraints on hydrate-controlled methane seepage off Svalbard, Science, 343, 284-287, 10.1126/science.1246298, 2014.

Biddle, J. F., Cardman, Z., Mendlovitz, H., Albert, D. B., Lloyd, K. G., Boetius, A., and Teske, A.: Anaerobic oxidation of methane at different temperature regimes in Guaymas Basin hydrothermal sediments, The ISME journal, 6, 1018-1031, 10.1038/ismej.2011.164, 2012.

Boetius, A. and Suess, E.: Hydrate Ridge: A natural laboratory for the study of microbial life fueld by methane from near-surface gas hydrates, Chem. Geol., 205, 291-310, 10.1016/j.chemgeo.2003.12.034, 2004.

Boetius, A. and Wenzhöfer, F.: Seafloor oxygen consumption fuelled by methane from cold seeps, Nature Geoscience, 6, 725, https://doi.org/10.1038/ngeo1926, 2013.

Boetius, A., Ravenschlag, K., Schubert, C. J., Rickert, D., Widdel, F., Giesecke, A., Amann, R., Jørgensen, B. B., Witte, U., and Pfannkuche, O.: A marine microbial consortium apparently mediating anaerobic oxidation of methane, Nature, 407, 623-626, https://doi.org/10.1038/35036572, 2000.

Bohrmann, G., Greinert, J., Suess, E., and Torres, M.: Authigenic carbonates from the Cascadia subduction zone and their relation to gas hydrate stability, Geology, 26, 647-650, https://doi.org/10.1130/0091-7613(1998)026<0647:ACFTCS>2.3.CO;2, 1998.

Bowden, D. A., Rowden, A. A., Thurber, A. R., Baco, A. R., Levin, L. A., and Smith, C. R.: Cold seep epifaunal communities on the Hikurangi Margin, New Zealand: composition, succession, and vulnerability to human activities, PLoS One, 8, e76869, https://doi.org/10.1371/journal.pone.0076869, 2013.

Campbell, K. A., Nelson, C. S., Alfaro, A. C., Boyd, S., Greinert, J., Nyman, S., Grosjean, E., Logan, G. A., Gregory, M. R., and Cooke, S.: Geological imprint of methane seepage on the seabed and biota of the convergent Hikurangi Margin, New Zealand: Box core and grab carbonate results, Marine Geology, 272, 285-306, https://doi.org/10.1016/j.margeo.2010.01.002, 2010.

Case, D. H., Pasulka, A. L., Marlow, J. J., Grupe, B. M., Levin, L. A., and Orphan, V. J.: Methane seep carbonates host distinct, diverse, and dynamic microbial assemblages, mBio, 6, e01348-01315, https://doi.org/10.1128/mbio.01348-15, 2015.

Cheng, H., Edwards, R. L., Hoff, J., Gallup, C. D., Richards, D., and Asmerom, Y.: The half-lives of uranium-234 and thorium-230, Chemical geology, 169, 17-33, 10.1016/S0009-2541(99)00157-6, 2000.

Cordes, E. E., Bergquist, D. C., and Fisher, C. R.: Macro-Ecology of Gulf of Mexico Cold Seeps, Ann. Rev. Marine Sci., 1, 143-168, https://doi.org/10.1146/annurev.marine.010908.163912, 2009.

https://doi.org/10.5194/egusphere-2026-6926
Preprint. Discussion started: 20 November 2026
© Author(s) 2026. CC BY 4.0 License.

Cordes, E. E., Arthur, M. A., Shea, K., Arvidson, R. S., and Fisher, C. R.: Modeling the mutualistic interactions between tubeworms and microbial consortia, PLoS Biology, 3, 1-10, https://doi.org/10.1371/journal.pbio.0030077, 2005.

Cowell, E. J., Stabbins, A. L., Cortés, J., Perez, R. C., and Cordes, E. E.: Apparent tectonic disturbance reshapes seepage and disrupts symbiotic species distributions at a Costa Rican methane seep, Frontiers in Marine Science, 13, 1900674, 10.3389/fmars.2026.1900674, 2026.

Fischer, D., Sahling, H., Nöthen, K., Bohrmann, G., Zabel, M., and Kasten, S.: Interaction between hydrocarbon seepage, chemosynthetic communities, and bottom water redox at cold seeps of the Makran accretionary prism: insights from habitat-specific pore water sampling and modeling, Biogeosciences, 9, 2013-2031, https://doi.org/10.5194/bg-9-2013-2012, 2012.

Fischer, D., Mogollón, J. M., Strasser, M., Pape, T., Bohrmann, G., Fekete, N., Spiess, V., and Kasten, S.: Subduction zone earthquake as potential trigger of submarine hydrocarbon seepage, Nature Geoscience, 6, 647-651, 10.1038/NGEO1886, 2013.

Fleischmann, S., Scholz, F., Du, J., Scholten, J., and Vance, D.: Processes controlling nickel and its isotopes in anoxic sediments of a seasonally hypoxic bay, Geochimica et Cosmochimica Acta, 391, 1-15, 10.1016/j.gca.2025.01.016, 2025.

Flögel, S. and Dullo, W.-C.: High-resolution water mass measurements around cold-water corals: a comparative test study between repeated Conductivity-Temperature-Depth (CTD) casts and continuous data acquisition of bottom waters from the West Florida Slope, Gulf of Mexico, Annalen des Naturhistorischen Museums in Wien. Serie A für Mineralogie und Petrographie, Geologie und Paläontologie, Anthropologie und Prähistorie, 209-224, http://www.jstor.org/stable/41701738, 2011.

Gasperini, L., Polonia, A., Del Bianco, F., Favali, P., Marinaro, G., and Etiope, G.: Cold seeps, active faults and the earthquake cycle along the North Anatolian Fault system in the Sea of Marmara (NW Turkey), Bollettino di Geofisica Teorica ed Applicata, 53, 371, 10.4330/bgta0082, 2012.

Geersen, J., Behrmann, J. H., Völker, D., Krastel, S., Ranero, C. R., Diaz-Naveas, J., and Weinrebe, W.: Active tectonics of the South Chilean marine fore arc (35 S–40 S), Tectonics, 30, https://doi.org/10.1029/2010TC002777, 2011.

Geersen, J., Scholz, F., Linke, P., Schmidt, M., Lange, D., Behrmann, J. H., Völker, D., and Hensen, C.: Fault zone controlled seafloor methane seepage in the rupture area of the 2010 M aule earthquake, C entral C hile, Geochemistry, Geophysics, Geosystems, 17, 4802-4813, https://doi.org/10.1002/2016GC006498, 2016.

Gieskes, J. M., Gamo, T., and Brumsack, H.: hemical methods for interstitial water analysis aboard JOIDES Resolution, *Ocean Drilling Program Technical Note*, 15, 10.2973/odp.tn.15.1991, 1991.

Goffredi, S. K., Motooka, C., Fike, D. A., Gusmão, L. C., Tilic, E., Rouse, G. W., and Rodríguez, E.: Mixotrophic chemosynthesis in a deep-sea anemone from hydrothermal vents in the Pescadero Basin, Gulf of California, BMC biology, 19, 8, https://doi.org/10.1186/s12915-020-00921-1, 2021.

Goffredi, S. K., Tilic, E., Mullin, S. W., Dawson, K. S., Keller, A., Lee, R. W., Wu, F., Levin, L. A., Rouse, G. W., and Cordes, E. E.: Methanotrophic bacterial symbionts fuel dense populations of deep-sea feather duster worms (Sabellida, Annelida) and extend the spatial influence of methane seepage, Science Advances, 6, eaay8562, https://www.science.org/doi/10.1126/sciadv.aay8562, 2020.

Grasshoff, K., Ehrhardt, M., and Kremling, K.: Methods of seawater analysis, Wiley-VCH Verlag GmbH, Weinheim, DOI: 10.1002/9783527613984, 1999.

Greinert, J., Bohrmann, G., and Suess, E.: Gas hydrate-associated carbonates and methane-venting at Hydrate Ridge: classification, distribution, and origin of authigenic lithologies, Natural gas hydrates: occurence, distibution, and detection, Am. Geophys. Union, Washington, D.C., https://doi.org/10.1029/GM124p0099, 2001.

Grevemeyer, I., Kaul, N., and Diaz-Naveas, J. L.: Geothermal evidence for fluid flow through the gas hydrate stability field off Central Chile—transient flow related to large subduction zone earthquakes?, Geophysical Journal International, 166, 461-468, https://doi.org/10.1111/j.1365-246X.2006.02940.x, 2006.

https://doi.org/10.5194/egusphere-2026-6926
Preprint. Discussion started: 20 November 2026
© Author(s) 2026. CC BY 4.0 License.

Han, X., Suess, E., Huang, Y., Wu, N., Bohrmann, G., Su, X., Eisenhauer, A., Rehder, G., and Fang, Y.: Jiulong methane reef: microbial mediation of seep carbonates in the South China Sea, Marine Geology, 249, 243-256, https://doi.org/10.1016/j.margeo.2007.11.012, 2008.

Huetten, E. and Greinert, J.: Software controlled guidance, recording and post-processing of seafloor observations by ROV and other towed devices: the software package OFOP, https://oceanrep.geomar.de/id/eprint/22342, 2008.

Ivanenkov, V. N. and Lyakhin, V. N.: Determination of total alkalinity in seawater, in: Methods of hydrochemical investigations in the ocean (in Russian), edited by: Bordovsky, O. K., and Ivanenkov, V. N., Nauka Publ. House, Moscow, 110-114, 1978.

Jeroschewski, P., Steuckart, C., and Kühl, M.: An amperometric microsensor for the determination of H2S in aquatic environments, Analytical chemistry, 68, 4351-4357, https://doi.org/10.1021/ac960091b, 1996.

Jordan, S., Gräwe, U., Treude, T., van der Lee, E., Schneider von Deimling, J., Rehder, G., and Schmale, O.: Pelagic methane sink enhanced by benthic methanotrophs ejected from a gas seep, Geophysical Research Letters, 48, e2021GL094819, https://doi.org/10.1029/2021GL094819, 2021.

Joye, S. B., Boetius, A., Orcutt, B. N., Montoya, J. P., Schulz, H. N., Erickson, M. J., and Logo, S. K.: The anaerobic oxidation of methane and sulfate reduction in sediments from Gulf of Mexico cold seeps, Chem. Geol., 205, 219-238, 10.1016/j.chemgeo.2003.12.019, 2004.

Jørgensen, B. B.: A comparison of methods for the quantification of bacterial sulphate reduction in coastal marine sediments: I. Measurements with radiotracer techniques, Geomicrobiol. J., 1, 11-27, https://doi.org/10.1080/01490457809377721, 1978.

Jørgensen, B. B., Wenzhöfer, F., Egger, M., and Glud, R. N.: Sediment oxygen consumption: Role in the global marine carbon cycle, Earth-Science Reviews, 103987, 2022.

Kallmeyer, J., Ferdelman, T. G., Weber, A., Fossing, H., and Jørgensen, B. B.: A cold chromium distillation procedure for radiolabeled sulfide applied to sulfate reduction measurements, Limnol. Oceanogr. Methods, 2, 171-180, https://doi.org/10.4319/lom.2004.2.171, 2004.

Keir, R. S., Schmale, O., Walter, M., Sültenfuß, J., Seifert, R., and Rhein, M.: Flux and dispersion of gases from the "Drachenschlund" hydrothermal vent at 8 18'S, 13 30'W on the Mid-Atlantic Ridge, Earth and Planetary Science Letters, 270, 338-348, 10.1016/j.epsl.2008.03.054, 2008.

Klaucke, I., Weinrebe, W., Linke, P., Kläschen, D., and Bialas, J.: Sidescan sonar imagery of widespread fossil and active cold seeps along the central Chilean continental margin, Geo-Marine Letters, 32, 489-499, https://doi.org/10.1007/s00367-012-0283-1, 2012.

Klonicki-Ference, E., Utter, D. R., Homola, K., Magyar, J. S., Orphan, V. J., Caress, D. W., Paduan, J. B., Levin, L., and Treude, T.: An Expanded Methanosphere: Methane Oxidation and Methanotrophs Surrounding Cold Seeps Across Oxygen Gradients on the Southern California Margin, EGUsphere, 2026, 1-51, https://doi.org/10.5194/egusphere-2026-4409, 2026.

Knittel, K. and Boetius, A.: Anaerobic oxidation of methane: progress with an unknown process, Annu. Rev. Microbiol., 63, 311-334, https://doi.org/10.1146/annurev.micro.61.080706.093130, 2009.

Krause, S. J., Liu, J., Yousavich, D. J., Robinson, D., Hoyt, D. W., Qin, Q., Wenzhöfer, F., Janssen, F., Valentine, D. L., and Treude, T.: Evidence of cryptic methane cycling and non-methanogenic methylamine consumption in the sulfate-reducing zone of sediment in the Santa Barbara Basin, California, Biogeosciences, 20, 4377-4390, https://doi.org/10.5194/bg-20-4377-2023, 2023.

Kutterolf, S., Liebetrau, V., Mörz, T., Freundt, A., Hammerich, T., and Garbe-Schönberg, D.: Lifetime and cyclicity of fluid venting at forearc mound structures determined by tephrostratigraphy and radiometric dating of authigenic carbonates, Geology, 36, 707-710, https://doi.org/10.1130/G24806A.1, 2008.

Lee, K. C., Pereira, O. S., and Levin, L. A.: Environmental drivers and dynamics of macroinvertebrate communities on carbonates at Southern California methane seeps, Marine Biology Research, 21, 401-416, https://doi.org/10.1080/17451000.2025.2569709, 2025.

https://doi.org/10.5194/egusphere-2026-6926
Preprint. Discussion started: 20 November 2026
© Author(s) 2026. CC BY 4.0 License.

Leefmann, T., Bauermeister, J., Kronz, A., Liebetrau, V., Reitner, J., and Thiel, V.: Miniaturized biosignature analysis reveals implications for the formation of cold seep carbonates at Hydrate Ridge (off Oregon, USA), Biogeosciences, 5, 731-738, https://doi.org/10.5194/bg-5-731-2008, 2008.

Levin, L. A.: Ecology of cold seep sediments: interactions of fauna with flow, chemistry and microbes, Oceanogr. and Mar. Biol.: Ann. Rev., 43, 1-46, 10.1201/9781420037449.ch1, 2005.

Levin, L. A., Mendoza, G. F., Gonzalez, J. P., Thurber, A. R., and Cordes, E. E.: Diversity of bathyal macrofauna on the northeastern Pacific margin: the influence of methane seeps and oxygen minimum zones, Mar. Ecol., 31, 94-110, https://doi.org/10.1111/j.1439-0485.2009.00335.x

Digital Object Identifier (DOI), 2010.

Levin, L. A., Soto, E., Castillo, Y., Esquete, P., and Marlow, J.: Congregation of cusk-eels (Genypterus chilensis, Ophidiiformes) at a deep-sea methane seep off Chile, Ecology, 106, e70237, 10.1002/ecy.70237, 2025.

Levin, L. A., Mendoza, G. F., Grupe, B. M., Gonzalez, J. P., Jellison, B., Rouse, G., Thurber, A. R., and Waren, A.: Biodiversity on the rocks: macrofauna inhabiting authigenic carbonate at Costa Rica methane seeps, PLoS One, 10, e0131080, https://doi.org/10.1371/journal.pone.0131080, 2015.

Levin, L. A., Baco, A. R., Bowden, D. A., Colaco, A., Cordes, E. E., Cunha, M. R., Demopoulos, A. W. J., Gobin, J., Grupe, B. M., and Le, J.: Hydrothermal vents and methane seeps: rethinking the sphere of influence, Frontiers in Marine Science, 3, 72, https://doi.org/10.3389/fmars.2016.00072, 2016.

Liebetrau, V., Eisenhauer, A., and Linke, P.: Cold seep carbonates and associated cold-water corals at the Hikurangi Margin, New Zealand: new insights into fluid pathways, growth structures and geochronology, Marine Geology, 272, 307-318, https://doi.org/10.1016/j.margeo.2010.01.003, 2010.

Liebetrau, V., Augustin, N., Kutterolf, S., Schmidt, M., Eisenhauer, A., Garbe-Schönberg, D., and Weinrebe, W.: Cold-seep-driven carbonate deposits at the Central American forearc: contrasting evolution and timing in escarpment and mound settings, International Journal of Earth Sciences, 103, 1845-1872, https://doi.org/10.1007/s00531-014-1045-2, 2014.

Lieser, K., Grevemeyer, I., Lange, D., Flueh, E., Tilmann, F., and Contreras-Reyes, E.: Splay fault activity revealed by aftershocks of the 2010 Mw 8.8 Maule earthquake, central Chile, Geology, 42, 823-826, https://doi.org/10.1130/G35848.1, 2014.

Linke, P.: FS SONNE Fahrtbericht/Cruise Report SO210 ChiFlux: Identification and investigation of fluid flux, mass wasting and sediments in the forearc of the central Chilean subduction zone, Valparaiso-Valparaiso, 23.09.-01.11. 2010, https://oceanrep.geomar.de/id/eprint/10374, 2011.

Linke, P., Schmidt, M., Rohleder, M., Al-Barakati, A., and Al-Farawati, R.: Novel online digital video and high-speed data broadcasting via standard coaxial cable onboard marine operating vessels, Marine Technology Society Journal, 49, 7-18, https://doi.org/10.4031/MTSJ.49.1.2, 2015.

Lomnitz, C.: Major earthquakes of Chile: a historical survey, 1535-1960, Seismological Research Letters, 75, 368-378, https://doi.org/10.1785/gssrl.75.3.368, 2004.

Loyd, S., Sample, J., Tripati, R., Defliese, W., Brooks, K., Hovland, M., Torres, M., Marlow, J., Hancock, L., and Martin, R.: Methane seep carbonates yield clumped isotope signatures out of equilibrium with formation temperatures, Nature Communications, 7, 12274, https://doi.org/10.1038/ncomms12274, 2016.

Luff, R. and Wallmann, K.: Fluid flow, methane fluxes, carbonate precipitation and biogeochemical turnover in gas hydrate-bearing sediments at Hydrate Ridge, Cascadia Margin: Numerical modeling and mass balances, Geochim. Cosmochim. Acta, 67, 3403-3421, 10.1016/S0016-7037(03)00127-3, 2003.

Mao, Y., Lin, T., Li, H., He, R., Ye, K., Yu, W., and He, Q.: Aerobic methane production by phytoplankton as an important methane source of aquatic ecosystems: Reconsidering the global methane budget, Science of The Total Environment, 907, 167864, 10.1016/j.scitotenv.2023.167864, 2024.

Marlow, J. J., Steele, J. A., Ziebis, W., Thurber, A. R., Levin, L. A., and Orphan, V. J.: Carbonate-hosted methanotrophy represents an unrecognized methane sink in the deep sea, Nature communications, 5, 5094, https://doi.org/10.1038/ncomms6094, 2014.

https://doi.org/10.5194/egusphere-2026-6926
Preprint. Discussion started: 20 November 2026
© Author(s) 2026. CC BY 4.0 License.

Mavromatis, V., Botz, R., Schmidt, M., Liebetrau, V., and Hensen, C.: Formation of carbonate concretions in surface sediments of two mud mounds, offshore Costa Rica: a stable isotope study, International journal of earth sciences, 103, 1831-1844, 10.1007/s00531-012-0843-7, 2014.

Mayr, M. J., Parra, S. A., Connon, S. A., Narayanan, A. K., Murali, R., Crémière, A., and Orphan, V. J.: Distinct microbial communities within and on seep carbonates support long-term anaerobic oxidation of methane and divergent pMMO diversity, The ISME Journal, 19, wraf153, https://doi.org/10.1093/ismejo/wraf153, 2025.

McGinnis, D. F., Sommer, S., Lorke, A., Glud, R. N., and Linke, P.: Quantifying tidally driven benthic oxygen exchange across permeable sediments: An aquatic eddy correlation study, Journal of Geophysical Research: Oceans, 119, 6918-6932, https://doi.org/10.1002/2014JC010303, 2014.

McGinnis, D. F., Cherednichenko, S., Sommer, S., Berg, P., Rovelli, L., Schwarz, R., Glud, R. N., and Linke, P.: Simple, robust eddy correlation amplifier for aquatic dissolved oxygen and hydrogen sulfide flux measurements, Limnology and Oceanography: Methods, 9, 340-347, https://doi.org/10.4319/lom.2011.9.340, 2011.

Melaniuk, K., Sztybor, K., Treude, T., Sommer, S., and Rasmussen, T. L.: Influence of methane seepage on isotopic signatures in living deep-sea benthic foraminifera, 79° N, Scientific Reports, 12, 1-13, https://doi.org/10.1038/s41598-022-05175-1, 2022.

Melnick, D. and Echtler, H. P.: Inversion of forearc basins in south-central Chile caused by rapid glacial age trench fill, Geology, 34, 709-712, https://doi.org/10.1130/G22440.1 2006.

Moreno, M., Rosenau, M., and Oncken, O.: 2010 Maule earthquake slip correlates with pre-seismic locking of Andean subduction zone, Nature, 467, 198-202, 10.1038/nature09349, 2010.

Muñoz, P., Lange, C. B., Gutièrrez, D., Hebbeln, D., Salamanca, M., Dezileau, L., Reyss, J., and Benninger, L.: Recent sedimentation and mass accumulation rates based on 210Pb along the Peru–Chile continental margin, Deep Sea Research Part II: Topical Studies in Oceanography, 51, 2523-2541, 10.1016/j.dsr2.2004.08.015, 2004.

Naehr, T. H., Rodriguez, N. M., Bohrmann, G., Paull, C. K., and Botz, R.: 29. Methane-drived authigenic carbonates associated with gas hydrate decomposition and fluid venting above the Blake Ridge Diapir, Proceedings of the Ocean Drilling Program, Scientific Results, 164, 285-300, 2000.

Niemann, H., Steinle, L., Blees, J., Bussmann, I., Treude, T., Krause, S., Elvert, M., and Lehmann, M. F.: Toxic effects of lab-grade butyl rubber stoppers on aerobic methane oxidation, Limn. Oceanogr. Methods, 13, 40–52, https://doi.org/10.1002/lom3.10005 Digital Object Identifier (DOI), 2015.

Niemann, H., Lösekann, T., De Beer, D., Elvert, M., Nadalig, T., Knittel, K., Aman, A., Sauter, E. J., Schlüter, M., Klages, M., Foucher, J.-P., and Boetius, A.: Novel microbial communities of the Haakon Mosby mud volcano and their role as a methane sink, Nature, 443, 854-858, https://doi.org/10.1038/nature05227, 2006.

Orphan, V. J., House, C. H., Hinrichs, K.-U., McKeegan, K. D., and De Long, E. F.: Methane-consuming Archaea revealed by directly coupled isotopic and phylogenetic analysis, Science, 293, 484-487, DOI: 10.1126/science.1061338, 2001.

Paull, C. K., Hecker, B., Commeau, R., Freeman-Lynde, R. P., Neumann, C., Corso, W. P., Golubic, S., Hook, J. E., Sikes, E., and Curray, J.: Biological communities at the Florida escarpment resemble hydrothermal vent taxa, Science, 226, 965-967, DOI: 10.1126/science.226.4677.965, 1984.

Peckmann, J., Reimer, A., Luth, U., Luth, C., Hansen, B. T., Heincke, C., Hoefs, J., and Reitner, J.: Methane-derived carbonates and authigenic pyrite from the northwestern Black Sea, Mar. Geol., 177, 129-150, https://doi.org/10.1016/S0025-3227(01)00128-1, 2001.

Quiroga, E. and Sellanes, J.: Growth and size-structure of Stegophiura sp.(Echinodermata: Ophiuroidea) on the continental slope off central Chile: a comparison between cold seep and non-seep sites, Journal of the Marine Biological Association of the United Kingdom, 89, 421-428, https://doi.org/10.1017/S0025315408002786, 2009.

Revsbech, N. P.: An oxygen microelectrode with a guard cathode, Limnol. Oceanogr., 34, 474-478, https://doi.org/10.4319/lo.1989.34.2.0474, 1989.

https://doi.org/10.5194/egusphere-2026-6926
Preprint. Discussion started: 20 November 2026
© Author(s) 2026. CC BY 4.0 License.

Sahling, H., Rickert, D., Raymond, W. L., Linke, P., and Suess, E.: Macrofaunal community structure and sulfide flux at gas hydrate deposits from the Cascadia convergent margin, NE Pacific, Mar. Ecol. Prog. Ser., 231, 121-138, https://doi.org/10.3354/meps231121, 2002.

Scholz, F., Hensen, C., Schmidt, M., and Geersen, J.: Submarine weathering of silicate minerals and the extent of pore water freshening at active continental margins, Geochimica et Cosmochimica Acta, 100, 200-216, 10.1016/j.gca.2012.09.043, 2013.

Sellanes, J., Pedraza-García, M. J., and Zapata-Hernández, G.: Do the methane seep areas constitute aggregation spots for the Patagonian toothfish (Dissostichus eleginoides) off central Chile?, Latin American Journal of Aquatic Research, 40, 980-991, 10.3856/vol40-issue4-fulltext-14, 2012.

Sellanes, J., Quiroga, E., and Neira, C.: Megafauna community structure and trophic relationships at the recently discovered Concepción Methane Seep Area, Chile, ~36°S, ICES J. Mar. Sci., 65, 1102-1111, https://doi.org/10.1093/icesjms/fsn099, 2008.

Smith, C. R., Glover, A. G., Treude, T., Higgs, N. D., and Amon, D. J.: Whale-fall ecosystems: recent insights into ecology, paleoecology, and evolution, Annual Review of Marine Science, 7, 571-596, https://doi.org/10.1146/annurev-marine-010213-135144, 2015.

Smrzka, D., Tseng, Y., Zwicker, J., Schröder-Ritzrau, A., Frank, N., Schmitt, A.-D., Pape, T., Birgel, D., Peckmann, J., Lin, S., and Bohrmann, G.: Marine carbon burial enhanced by microbial carbonate formation at hydrocarbon seeps, Communications Earth & Environment, 6, 7, https://doi.org/10.1038/s43247-024-01960-0, 2025.

Sommer, S., Linke, P., Pfannkuche, O., Niemann, H., and Treude, T.: Benthic respiration in a seep habitat dominated by dense beds of ampharetid polychaetes at the Hikurangi Margin (New Zealand), Marine Geology, 272, 223-232, https://doi.org/10.1016/j.margeo.2009.06.003, 2010.

Sommer, S., Linke, P., Pfannkuche, O., Schleicher, T., Deimling, J. S. v., Reitz, A., Haeckel, M., Flögel, S., and Hensen, C.: Seabed methane emissions and the habitat of frenulate tubeworms on the Captain Arutyunov mud volcano (Gulf of Cadiz), Marine Ecology Progress Series, 382, 69-86, https://doi.org/10.3354/meps, 2009.

Sommer, S., Pfannkuche, O., Linke, P., Luff, R., Greinert, J., Drews, M., Gubsch, S., Pieper, M., Poser, M., and Viergutz, T.: Efficiency of the benthic filter: Biological control of the emission of dissolved methane from sediments containing shallow gas hydrates at Hydrate Ridge, Glob. Biogeochem. Cycl., 20, 1-14, https://doi.org/10.1029/2004GB002389, 2006.

Stabbins, A., Goffredi, S., Gasbarro, R., Dawson, K., Magyar, J., Glazier, A., Meinert, K., Orphan, V., and Cordes, E.: Microbially mediated carbon utilization by a cold-water coral inhabiting methane seeps, Scientific Reports, 16, 9603, https://doi.org/10.1038/s41598-025-32153-0, 2026.

Steinle, L., Graves, C. A., Treude, T., Ferré, B., Biastoch, A., Bussmann, I., Berndt, C., Krastel, S., James, R. H., Behrens, E., Böning, C. W., Greinert, J., Sapart, C. J., Scheinert, M., Sommer, S., Lehmann, M. F., and Niemann, H.: Water column methanotrophy controlled by a rapid oceanographic switch, Nature Geosci., 8, 378, https://doi.org/10.1038/ngeo2420, 2015.

Suess, E.: Marine cold seeps, in: Handbook of hydrocarbon and lipid microbiology, edited by: Timmis, K. N., Springer-Verlag, Berlin Heidelberg, 187-203, https://doi.org/10.1007/978-3-540-77587-4, 2010.

Suess, E.: Marine cold seeps and their manifestations: geological control, biogeochemical criteria and environmental conditions, International journal of earth sciences, 103, 1889-1916, https://doi.org/10.1007/s00531-014-1010-0, 2014.

Suess, E.: Marine cold seeps: background and recent advances, Hydrocarbons, oils and lipids: Diversity, origin, chemistry and fate, 747-767, https://doi.org/10.1007/978-3-319-90569-3_27, 2020.

Tavormina, P. L., Ussler III, W., and Orphan, V. J.: Planktonic and sediment-associated aerobic methanotrophs in two seep systems along the North American margin, Applied and Environmental Microbiology, 74, 3985-3995, https://doi.org/10.1128/AEM.00069-08, 2008.

Tavormina, P. L., Ussler, W., Joye, S. B., Giovannoni, S. J., and Orphan, V.: Intergenic spacer length of particulate methane monooxygenases reveals distributions of microbial methane oxidizers in the mesopelagic ocean, ISME Journal, https://doi.org/10.1038/ismej.2009.155, 2010.

https://doi.org/10.5194/egusphere-2026-6926
Preprint. Discussion started: 20 November 2026
© Author(s) 2026. CC BY 4.0 License.

Teichert, B., Eisenhauer, A., Bohrmann, G., Haase-Schramm, A., Bock, B., and Linke, P.: U/Th systematics and ages of authigenic carbonates from Hydrate Ridge, Cascadia Margin: recorders of fluid flow variations, Geochimica et Cosmochimica Acta, 67, 3845-3857, 10.1016/S0016-7037(03)00128-5, 2003.

Teichert, B. M. A., Bohrmann, G., and Suess, E.: Chemoherms on Hydrate Ridge—Unique microbially-mediated carbonate build-ups growing into the water column, Palaeogeography, Palaeoclimatology, Palaeoecology, 227, 67-85, 10.1016/j.palaeo.2005.04.029, 2005.

Thurber, A. R., Sweetman, A. K., Narayanaswamy, B. E., Jones, D. O., Ingels, J., and Hansman, R.: Ecosystem function and services provided by the deep sea, Biogeosciences, 11, 3941-3963, 10.5194/bg-11-3941-2014, 2014.

Torres, M. E., McManus, J., Hammond, D., Angelis de, M. A., Heeschen, K. U., Colbert, S. L., Tryon, M. D., Brown, K. M., and Suess, E.: Fluid and chemical fluxes in and out of sediments hosting methane hydrate deposits on Hydrate Ridge, OR, I: Hydrological provinces, Earth Planet. Sci. Lett., 201, 525-540, 10.1016/S0012-821X(02)00733-1, 2002.

Treude, T., Krüger, M., Boetius, A., and Jørgensen, B. B.: Environmental control on anaerobic oxidation of methane in the gassy sediments of Eckernförde Bay (German Baltic), Limnol. Oceanogr., 50, 1771-1786, https://doi.org/10.4319/lo.2005.50.6.1771, 2005a.

Treude, T., Boetius, A., Knittel, K., Wallmann, K., and Jørgensen, B. B.: Anaerobic oxidation of methane above gas hydrates at Hydrate Ridge, NE Pacific Ocean, Mar. Ecol. Prog. Ser., 264, 1-14, https://doi.org/10.3354/meps264001 2003.

Treude, T., Kiel, S., Linke, P., Peckmann, J., and Goedert, J. L.: Elasmobranch egg capsules associated with modern and ancient cold seeps: a nursery for marine deep-water predators, Marine Ecology Progress Series, 437, 175-181, https://doi.org/10.3354/meps, 2011.

Treude, T., Niggemann, J., Kallmeyer, J., Wintersteller, P., Schubert, C. J., Boetius, A., and Jørgensen, B. B.: Anaerobic oxidation of methane in the sulfate-methane transition along the Chilean continental margin, Geochim. Cosmochim. Acta, 69, 2767-2779, 10.1016/j.gca.2005.01.002, 2005b.

Treude, T., Smith, C. R., Wenzhöfer, F., Carney, E., Bernardino, A. F., Hannides, A. K., Krüger, M., and Boetius, A.: Biogeochemistry of a deep-sea whale fall: sulfate reduction, sulfide efflux and methanogenesis, Marine Ecology Progress Series, 382, 1-21, https://doi.org/10.3354/meps, 2009.

Tryon, M. D., Brown, K. M., and Torres, M. E.: Fluid and chemical flux in and out of sediments hosting methane hydrate deposits on Hydrate Ridge, OR, II: Hydrological processes, Earth Planet. Sci. Lett., 201, 541-557, 10.1016/S0012-821X(02)00732-X, 2002.

Valentine, D. L., Blanton, D. C., Reeburgh, W. S., and Kastner, M.: Water column methane oxidation adjacent to an area of active gas hydrate dissociation, Eel River Basin, Geochim. Cosmochim. Acta, 65, 2633-2640, 10.1016/S0016-7037(01)00625-1, 2001.

Völker, D., Scholz, F., and Geersen, J.: Analysis of submarine landsliding in the rupture area of the 27 February 2010 Maule earthquake, Central Chile, Marine Geology, 288, 79-89, https://doi.org/10.1016/j.margeo.2011.08.003, 2011.

Völker, D., Weinrebe, W., Behrmann, J. H., Bialas, J., and Klaeschen, D.: Mass wasting at the base of the south central Chilean continental margin: the Reloca Slide, Advances in Geosciences, 22, 155-167, https://doi.org/10.5194/adgeo-22-155-2009, 2009.

Wallmann, K., Linke, P., Suess, E., Bohrmann, G., Sahling, H., Schlüter, M., Dählmann, A., Lammers, S., Greinert, J., and Von Mirbach, N.: Quantifying fluid flow, solute mixing, and biogeochemical turnover at cold vents of the eastern Aleutian subduction zone, Geochim. Cosmochim. Acta, 61, 5209-5219, 10.1016/S0016-7037(97)00306-2, 1997.

Whiticar, M. J.: Carbon and hydrogen isotope systematics of bacterial formation and oxidation of methane, Chem. Geol., 161, 291-314, 10.1016/S0009-2541(99)00092-3, 1999.

Wieman, S. T., Skarke, A., Beeson, J., Frates, E., Villar-Muñoz, L., Oppo, D., Youngs, S., Kapit, J., Soto, E., and Marlow, J. J.: Quantifying deep ocean methane along the central Chilean Margin, Geophysical Research Letters, 53, e2026GL124079, 10.1029/2026GL124079, 2026.

https://doi.org/10.5194/egusphere-2026-6926
Preprint. Discussion started: 20 November 2026
© Author(s) 2026. CC BY 4.0 License.

Zapata-Hernández, G., Sellanes, J., Thurber, A. R., Levin, L. A., Chazalon, F., and Linke, P.: New insights on the trophic ecology of bathyal communities from the methane seep area off Concepción, Chile (~ 36 S), Marine ecology, 35, 1-21, https://doi.org/10.1111/maec.12051, 2014.

https://doi.org/10.5194/egusphere-2026-6926
Preprint. Discussion started: 20 November 2026
© Author(s) 2026. CC BY 4.0 License.

Table 1. Station and instrument data. For OFOS and ROV, date and location represent start of the survey. For all other instruments and sampling devices the date and location of the water-column cast/seafloor deployment (CTD, MUC, GC, BIGO, PRFL, POZ, ECM, BC), respectively, the sampling by ROV (ROV-Niskin, ROV-PC) is provided. Devices deployed by ROV (ECM, BC) were recovered during the following ROV dive. For carbonate sampling details, see **Table 2**. For abbreviations of instruments see Materials and Methods section.

Station/ Instrument No.	CMSA Box No.	Sample ID	Sampling Date in 2010 (UTC-based)	Latitude	Longitude	Water Depth (m)
St. 8/OFOS-1	3		28.09.	-35.97485	-73.64180	1080
St. 9/CTD-2	3		29.09.	-35.98283	-73.63195	1050
St. 11/OFOS-2	3		30.09.	-35.97035	-73.62940	1089
St. 14-1/OFOS-3	2		02.10.	-36.46306	-73.67306	693
St. 14-2/OFOS-4	2		02.10.	-36.46558	-73.68345	707
St. 16/MUC-1	2		02.10.	-36.47072	-73.67890	700
St. 17/CTD-4	2		02.10.	-36.47052	-73.67857	700
St. 18/OFOS-5	1		02.10.	-36.39032	-73.70198	802
St. 19/OFOS-6	4		03.10.	-36.36338	-73.70837	786
St. 20/CTD-5	1		03.10.	-36.41077	-73.70335	688
St. 21/ROV-1	1		03.10.	-36.40867	-73.70295	687.8
		Niskin BB		-36.42315	-73.70133	665.8
		Niskin StBd		-36.42315	-73.70137	665.8
St. 25/ROV-2	4		04.10.	-36.365768	-73.713066	780.3
		Niskin StBd		-36.38097	-73.71281	691.5
		Niskin BB		-36.38130	-73.71246	689.5
		PC-03, -05		-36.38128	-73.71245	689.1
St. 26/CTD-6	4		05.10.	-36.38113	-73.71262	685
St. 28/CTD-7	4		05.10.	-36.37035	-73.71225	699
St. 29/GC-8	2		05.10.	-36.47050	-73.67880	707
St. 30/ROV-3	1		05.10.	-36.41998	-73.70175	674.3
		Niskin StBd		-36.41868	-73.70258	667.9
St. 35/GC-10	Reference		06.10.	-36.47100	-73.73400	1008
St. 37/ROV-4	2		06.10.	-36.46970	-73.67865	700.7
		ECM-1		-36.47055	-73.67893	703.7
		ECM-2		-36.47062	-73.67889	705.8
		Niskin StBd		-36.47367	-73.66676	685.5
		Niskin BB		-36.47287	-73.66843	686.2
St. 38/POZ-1	2		06.10.	-36.47068	-73.67897	704
St. 41/GC-13	4		07.10.	-36.38300	-73.71100	697
St. 42/ROV-5	2		07.10.	-36.46978	-73.67897	703.3
		PC-05,-07		-36.47068	-73.67880	706.8

1990

https://doi.org/10.5194/egusphere-2026-6926
Preprint. Discussion started: 20 November 2026
© Author(s) 2026. CC BY 4.0 License.

Table 1 Continued.

Station/ Instrument No.	CMSA Box No.	Sample ID	Sampling Date in 2010 (UTC-based)	Latitude	Longitude	Water Depth (m)
St. 54/MUC-2	2		13.10.	-36.47035	-73.67875	707
St. 58/PRFL-1	2		14.10.	-36.47048	-73.67878	705
St. 59/CTD-10	2		14.10.	-36.47053	-73.67858	706
St. 60/GC-18	4		14.10.	-36.36400	-73.72100	859
St. 65/CTD-11	3		15.10.	-35.98433	-73.62900	1045
St. 66/MUC-3	4		15.10.	-36.38100	-73.71300	679
St. 68/MUC-4	Reference		16.10.	-36.47100	-73.73500	1006
St. 74/ROV-6	8		17.10.	-36.44085	-73.68933	707.4
		Niskin StBd		-36.44277	-73.68980	701.2
		Niskin BB		-36.44278	-73.68977	701.6
		PC-01,-12		-36.44278	-73.68978	701.7
		PC-05,-07		-36.44330	-73.69060	706.8
St. 75/BIGO-1	2		17.10.	-36.47022	-73.67847	700
St. 76/CTD-12	8		18.10.	-36.44217	-73.68917	700
St. 78/ROV-7	1		18.10.	-36.41935	-73.70188	673.3
		Niskin StBd		-36.41900	-73.70197	677.6
		Niskin BB		-36.41872	-73.70240	673.9
St. 79/PRFL-2	2		18.10.	-36.47055	-73.67918	700
St. 84/ROV-8	4		19.10.	-36.38113	-73.71010	682.9
		ECM-1		-36.38108	-73.71225	689.4
		ECM-2		-36.38122	-73.71240	689.2
		BC-1		-36.38113	-73.71225	688.9
		Niskin BB		-36.38107	-73.71227	688.8
St. 87/CTD-13	4		20.10.	-36.38167	-73.71167	687
St. 88/ROV-9	4		20.10.	-36.38709	-73.70547	687.3
		Niskin StBd		-36.38095	-73.71017	685.1
		Niskin BB		-36.38117	-73.71025	685.3
		PC-01,-05		-36.38118	-73.70988	685.4
St. 94/POZ-2	4		22.10.	-36.38042	-73.71111	684.6
St. 95/ROV-10	1		22.10.	-36.39502	-73.70343	702.7
		Niskin BB		-36.41025	-73.70325	685.1
		Niskin StBd		-36.41047	-73.70348	685.5
St. 98/ROV-11	3		23.10.	-35.99650	-73.63863	966.2
		PC-05,-07		-35.98620	-73.63185	1007.8
		PC-01, PC-16		-35.98592	-73.63187	1008
		PC-13,-18		-35.98590	-73.63180	1008.6

1991

https://doi.org/10.5194/egusphere-2026-6926
Preprint. Discussion started: 20 November 2026
© Author(s) 2026. CC BY 4.0 License.

Table 2. U-Th isotope systematics and light stable isotope data of carbonate samples. For abbreviations of instruments see Materials and Methods section.

Station/ Instrument No.	CMSA Box No.	Sampling Date in 2010 (UTC-based)	Latitude	Longitude	Water Depth (m)	Sample ID	Sample Description [1]	U-Th Age (kys BP)	^{238}U conc. (ppm)	^{232}Th conc. (ppb)	^{230}Th/^{232}Th (dpm/dpm)	^{238}U/^{232}Th (dpm/dpm)	^{230}Th/^{234}U (dpm/dpm)	^{234}U/^{238}U (dpm/dpm)	δ^{234}U [2] initial (‰)	$\delta^{13}C_{(V\text{-}PDB)}$ (‰)	$\delta^{18}O_{(V\text{-}PDB)}$ (‰)	Carbonate Components by XRD [3] (%W)
St. 25/ROV-2	4	04.10.	-36.38163	-73.71214	683.7	P-4/16/149-11	downside, surface layer	4.7 ± 0.1	4.96 ± 0.03	11.4 ± 0.07	65	1335.72 ± 11.79	0.042 ± 0.001	1.139 ± 0.003	141 ± 2.8	-45.56 ± 0.02	3.53 ± 0.02	93% ARA
						P-4/17/150-11	downside, internal layer	5.7 ± 0.2	2.5 ± 0.01	36.8 ± 0.23	13	208.13 ± 1.76	0.051 ± 0.001	1.142 ± 0.002	144 ± 2.4	-46.40 ± 0.02	3.14 ± 0.04	80% ARA, 10% CAL
St. 64/TVG-4	3[#1]	15.10.	-35.97597	-73.63980	1022	TVG-4/1/305-11	uppermost rim	248 ± 8	1.15 ± 0.01	3.1 ± 0.08	1056	1147.20 ± 29.14	0.903 ± 0.007	1.028 ± 0.002	56 ± 1.8	-46.88 ± 0.02	5.26 ± 0.03	96% ARA
						TVG-4/2/306-11	white area of hanging layer	232 ± 7	2.73 ± 0.01	10.7 ± 0.07	743	783.57 ± 6.68	0.893 ± 0.008	1.060 ± 0.003	116 ± 3.1	-48.28 ± 0.01	4.86 ± 0.03	94% ARA
						TVG-4/3/307-11	upper white line of laminated pack	437 ± 53	1.81 ± 0.01	0.8 ± 0.01	6705	6703.18 ± 68.64	0.987 ± 0.009	1.014 ± 0.002	47 ± 1.8	-49.24 ± 0.03	4.85 ± 0.04	95% ARA
						TVG-4/4/308-11	lower white line of laminated pack beneath 3	189 ± 4	2.65 ± 0.01	3.1 ± 0.02	2238	2587.66 ± 21.24	0.830 ± 0.007	1.041 ± 0.002	71 ± 2.3	-50.85 ± 0.02	5.24 ± 0.03	94% ARA
						TVG-4/5/309-11	white line beneath "clay"	530 ± 175	0.41 ± 0.00	1.42 ± 0.01	903	874.22 ± 757	1.004 ± 0.008	1.029 ± 0.002	128 ± 2.2	-50.34 ± 0.01	3.97 ± 0.02	90% ARA
						TVG-4/6/310-11	bottom network	313 ± 18	0.52 ± 0.00	1.44 ± 0.01	1059	1100.46 ± 12.94	0.948 ± 0.009	1.015 ± 0.002	37 ± 2.4	-51.41 ± 0.03	4.74 ± 0.01	n.d.
						TVG-4/7/311-11	soft filling (diatom clay) above 5	173 ± 9	6.29 ± 0.04	1498 ± 9.69	12	12.87 ± 0.12	0.805 ± 0.017	1.058 ± 0.002	95 ± 2.4	-51.29 ± 0.01	5.60 ± 0.03	n.d.
St. 69/TVG-5	1	16.10.	-36.41862	-73.70305	670	P-5/18/151-11	disperse network	168 ± 4	8.77 ± 0.05	820 ± 4.80	30	32.79 ± 0.27	0.802 ± 0.009	1.111 ± 0.003	179 ± 2.8	-38.08 ± 0.01	4.33 ± 0.04	76% ARA, 6.6% CAL
						P-5/19/152-11	pore volume filling	69 ± 1	4.75 ± 0.04	105 ± 0.85	74	138.37 ± 1.61	0.472 ± 0.006	1.123 ± 0.002	150 ± 1.7	-41.73 ± 0.01	4.26 ± 0.03	62% ARA, 12% DOL, 11% CAL
						TVG-5/1/301-11	upper rim	82 ± 1	4.02 ± 0.02	0.88 ± 0.01	8250	13966.32 ± 138.83	0.532 ± 0.004	1.111 ± 0.002	140 ± 1.7	-33.59 ± 0.01	4.05 ± 0.03	97% ARA
						TVG-5/2/302-11	central layer	85 ± 1	4.51 ± 0.02	4.89 ± 0.03	1724	2829.60 ± 23.30	0.548 ± 0.004	1.112 ± 0.002	142 ± 2.3	-36.00 ± 0.01	4.18 ± 0.01	93% ARA
						TVG-5/3/303-11	lower vein	59 ± 1	2.89 ± 0.02	2.98 ± 0.02	1400	2966.55 ± 23.80	0.422 ± 0.003	1.119 ± 0.002	140 ± 2.1	-35.26 ± 0.02	4.44 ± 0.03	96% ARA
						TVG-5/4/304-11	center area	50 ± 1	3.91 ± 0.02	19.2 ± 0.38	257	624.41 ± 13.03	0.368 ± 0.008	1.116 ± 0.003	133 ± 3.1	-39.74 ± 0.02	4.50 ± 0.02	92% ARA
St. 74/ROV-6	8	17.10.	-36.44285	-73.68980	701.6	P2+ spec/139-11-3	lowest level of structure	n.d.	n.d.	n.d.	n.d.	n.d.	n.d.	n.d.	n.d.	-46.03 ± 0.02	5.78 ± 0.07	29% ARA, 21% CAL, 18% DOL
St. 78/ROV-7	1	18.10.	-36.41880	-73.70232	676.7	P9/28/155-11	pore volume filling	95 ± 3	12.34 ± 0.07	1320 ± 8.15	19	28.61 ± 0.25	0.590 ± 0.009	1.107 ± 0.003	140 ± 3.0	-40.53 ± 0.02	3.76 ± 0.04	68% ARA
						P9/5/156-11	disperse vein system	91 ± 2	4.45 ± 0.03	109 ± 1.05	82	125.66 ± 1.51	0.573 ± 0.007	1.128 ± 0.002	166 ± 2.1	-44.55 ± 0.01	3.67 ± 0.05	n.d.
St. 78/ROV-7	1	18.10.	-36.41865	-73.70310	667.0	P1/3/144-11	outer white	63 ± 1	6.07 ± 0.04	14 ± 0.10	667	1326.15 ± 12.73	0.445 ± 0.004	1.130 ± 0.004	156 ± 4.3	-35.88 ± 0.02	4.66 ± 0.03	75% ARA, 7.2% DOL, 3.7% CAL
						P1/4/145-11	rose	50 ± 1	6.61 ± 0.05	6.12 ± 0.05	1370	3311.85 ± 36.36	0.371 ± 0.004	1.122 ± 0.006	140 ± 5.8	-39.66 ± 0.02	4.39 ± 0.03	88% ARA, 5.9% DOL, 3.9% CAL
						P1/5/146-11	inner white	54 ± 2	5.55 ± 0.11	2.61 ± 0.06	2872	6526.01 ± 188.65	0.395 ± 0.011	1.115 ± 0.003	134 ± 3.5	-33.91 ± 0.01	4.61 ± 0.04	79% ARA, 7.5% DOL, 4.7% CAL
						P1/7/147-11	innermost white	74 ± 1	2.88 ± 0.02	2.77 ± 0.02	1762	3188.92 ± 33.98	0.496 ± 0.005	1.113 ± 0.003	139 ± 3.1	-46.08 ± 0.02	4.43 ± 0.02	80% ARA, 9.2% DOL, 6.7% CAL
						P1/8/148-11	innermost dark	85 ± 2	6.5 ± 0.04	660 ± 3.80	19	30.25 ± 0.26	0.547 ± 0.008	1.104 ± 0.005	132 ± 4.8	-43.95 ± 0.02	-13.50 ± 0.03	79% ARA, 3.1% CAL
St. 78/ROV-7	1	18.10.	-36.42282	-73.70184	660.6	P7/22/154-11	massive aragonite vein filling	145 ± 5	5.26 ± 0.05	341 ± 5.93	40	47.34 ± 0.96	0.750 ± 0.012	1.130 ± 0.002	196 ± 1.8	-37.78 ± 0.01	4.55 ± 0.04	66% ARA, 14% CAL
St. 78/ROV-7	1	18.10.	-36.42427	-73.70198	675.8	P6/20/153-11	massive aragonite vein filling	61 ± 1	3.58 ± 0.02	22.5 ± 0.16	243	488.77 ± 4.49	0.434 ± 0.004	1.143 ± 0.002	171 ± 2.3	-43.37 ± 0.01	4.61 ± 0.03	81% ARA, 8.9% CAL
St. 95/ROV-10	1	22.10.	-36.41047	-73.70348	685.5	P+1/2/140-11	solid center layer	52 ± 1	8.46 ± 0.09	56 ± 0.59	201	466.91 ± 6.99	0.384 ± 0.006	1.119 ± 0.002	138 ± 2.0	-43.41 ± 0.01	4.43 ± 0.02	38% ARA, 19% DOL, 16% CAL
						P+1/3/141-11	loosely packed granulate	58 ± 1	13.8 ± 0.08	764 ± 5.80	26.8	55.37 ± 0.55	0.417 ± 0.006	1.126 ± 0.003	149 ± 3.1	-44.57 ± 0.02	0.68 ± 0.03	88% ARA
St. 98/ROV-11	3[#1]	23.10.	-35.98590	-73.63185	1008	P0/1/142-11	seepage opening, soft carbonate	180 ± 28	0.91 ± 0.01	710 ± 32.43	4.61	3.95 ± 0.18	0.832 ± 0.053	1.173 ± 0.002	287 ± 2.7	-40.91 ± 0.04	4.75 ± 0.04	72% DOL
						P0/2/143-11	seepage opening, hard carbonate	n.d.	n.d.	n.d.	n.d.	n.d.	n.d.	n.d.	n.d.	-35.87 ± 0.01	7.64 ± 0.04	72% DOL, 8.2% ARA, 5.2% LAN

Uncertainties presented on 2 sigma level. n.d. = not determined

Note 1: For sample photos with more details see Suppl. Material 3

Note 2: ($^{234}U/^{238}U$ act. ratio at zero age -1) * 1000 at time (t = U/Th-age). Measured $^{234}U/^{238}U$ back-calculated for ^{234}U decay since carbonate precipitation, based on the individual U/Th ingrowth age and half-lives measured by Cheng et al. (2000). $\delta^{234}U(t)$ of Roshok-1 isochron approaches based on isoplot 3.75 calculation.

Note 3: ARA = aragonite ($CaCO_3$), CAL = calcite ($CaCO_3$), DOL = dolomite ($CaMg(CO_3)_2$, LAN = lansfordite ($MgCO_3$). Other minerals included in the analyses (data not shown): silicon (Si), quartz (SiO_2), albite ($NaAlSi_3O_8$), diesporе ($AlO(OH)$), halite (NaCl).

Note 4: maximum U/Th-derived ages in Box-3 uncertain due to potential open system alteration

https://doi.org/10.5194/egusphere-2026-6926
Preprint. Discussion started: 20 November 2026
© Author(s) 2026. CC BY 4.0 License.

Table 3. Carbon isotopic signatures of methane with corresponding methane concentrations. Water samples were collected by ROV-Niskin approximately 1 m above the seafloor. Sediment samples were collected from gravity corer, multicorer, and ROV push cores. For abbreviations of instruments see Materials and Methods section. n.a. = not applicable

Station/ Instrument No.	CMSA Box No.	ROV Sampling Device	Water or Sediment Depth	CH_4	$\delta^{13}C_{(V\text{-}PDB)}$	Comment
Water Samples			(m)	(nmol L^{-1})	(‰)	
St. 25/ROV-2	4	Niskin BB	689.1	1985	-59.3	collected above clam field
St. 30/ROV-3	1	Niskin StBd	667.9	174	-61.7	collected above creviche
St. 37/ROV-4	2	Niskin StBd	685.5	235	-60.5	collected above black sediment spot
		Niskin BB	686.2	126	-58.5	collected above black sediment spot
St. 74/ROV-6	8	Niskin StBd	701.2	63	-57.8	collected above mat
		Niskin BB	701.2	52	-57.0	collected above mat
St. 78/ROV-7	1	Niskin StBd	677.6	341	-59.7	collected above clams and tubeworms
		Niskin BB	673.9	587	-63.8	collected above mat
St. 84/ROV-8	4	Niskin BB	688.8	412	-59.5	collected over crack in seafloor
St. 88/ROV-9	4	Niskin StBd	685.1	30	-58.3	collected on a rim over a crack in seafloor
St. 95/ROV-10	1	Niskin StBd	685.5	502	-62.7	collected above active seep orifice
Sediment Samples			(cm)	(mmol L^{-1})	(‰)	
St. 16/MUC-1	2	n.a.	19	1.59	-85.6	collected in black sediment spot
St. 41/GC-13	4	n.a.	2.5	0.02	-60.4	dead clam field
			27.5	0.68	-70.3	
			57.5	3.54	-62.6	
			86.5	0.71	-60.4	
St. 54/MUC-2	2	n.a.	15	0.21	-78.4	brown surface, sub-surface black layer
St. 60/GC-18	4	n.a.	42	2.22	-79.9	dead clam field
			122	9.63	-63.6	
			202	3.89	-64.9	
			282	1.93	-66.7	
			472	2.53	-65.1	
			572	0.95	-64.6	
St.98/ROV-11	3	PC-16	16	0.39	-67.2	collected in tubeworm field
St.98/ROV-11	3	PC-5	15	6.86	-65.0	collected in mat
St.98/ROV-11	3	PC-13	14	5.21	-68.6	collected in clam field

Table 4. Benthic O_2 uptake at Box-2 and Box-4.
BIGO = benthic lander system equipped with two chambers (CH-1 and CH-2); PRFL = profiler lander with O_2 microsensors; ECM = eddy covariance module; BC = ROV-operated benthic chamber. Chamber-based measurements represent total oxygen uptake (TOU), profiler measurements represent diffusive oxygen uptake (DOU), and eddy covariance measurements represent turbulent oxygen uptake.

	O_2 uptake (mmol m^{-2} d^{-1})	
Instrument	**Box 2**	**Box 4**
BIGO-1, Ch-1	16.4	
BIGO-1, CH-2	9.1	
PRFL-1	8.4 ± 4.3	
PRFL-2	4.1 ± 2.5	
ROV-4, ECM	9.1 ± 5.0	
ROV-9, BC		38.9
ROV-8, ECM		6.3 ± 1.1

https://doi.org/10.5194/egusphere-2026-6926
Preprint. Discussion started: 20 November 2026
© Author(s) 2026. CC BY 4.0 License.

Table 5. Comparisons of major parameters between Boxes. n.d. = not determined in this box, N/A = not a relevant feature in this box.

Parameter	Box-1	Box-2	Box-3	Box-4	Box-8[b]
Methane seep carbonates age range (ky BP)	50-168	N/A	173-530[a]	4.7-5.7	n.d.
Max ROV Niskin CH_4 (nM)	587	235	n.d.	3776	63
Max CTD Niskin CH_4 (nM)	35 (@671 m)	66 (@694 m)	14 (@794 m)	169 (@679 m)	40 (@604 m)
Max sediment CH_4 (mM)	N/A	98	9.5	9.6	7.1
Max sediment sulfide (mM)	N/A	18	15	17	15
Max sediment methane oxidation (nmol cm^{-3} d^{-1})	N/A	832 (likely AOM)	461 (likely MOx)	865 (likely AOM)	132 (likely AOM)
Max sediment sulfate reduction (nmol cm^{-3} d^{-1})	N/A	774	68	1946	1258
Sediment oxygen utilization range (µmol m^{-2} d^{-2})	N/A	4.1 (DOU) - 16. 4 (TOU)	n.d.	6.3 (ECM) - 39 (DOU)	n.d.
Chemosynthetic key organisms (abundance in brackets)	Lamellibrachia-type tubeworms (high), clams (low), sulfur-oxidizing bacteria mats (low)	sulfur-oxidizing bacteria mats (medium), clams (low)	Lamellibrachia-type tubeworms (medium), clams (medium), sulfur-oxidizing bacteria mats (low-medium)	Lamellibrachia-type tubeworms (medium), frenulate-type tubeworms (low), clams (high), sulfur-oxidizing bacteria mats (medium)	Lamellibrachia-type tubeworms (medium), clams (medium), sulfur-oxidizing bacteria mats (medium)
Carbonate-associated organisms	soft corals, hydroids, sponges, squat lobster, brittle stars	N/A	serpulid worms, soft corals, hydroids, songes, anamones, brittle/basket stars	hydroids, soft corals, anenomes, sponges, scleractinian corals	soft corals, hydroids, sponges, brittle/basket stars
Sediment vs Carbonate coverage	carbonate (massiv) dominated	sediment dominated	mix of sediment and massive carbonates	sediment with some carbonate nodules	mix of sediment and carbonate plates
Seep life cycle suggested after Arrázola & Acosta (2024)	Senescence to Extinction	Birth to Youth	Senescence	Youth	Maturity

[a]maximum U/Th-derived ages uncertain due to potential open system alteration, [b]Box-8 video surveys and quantity of samples where likely too restricted to provide a representative characterizations.

https://doi.org/10.5194/egusphere-2026-6926
Preprint. Discussion started: 20 November 2026
© Author(s) 2026. CC BY 4.0 License.

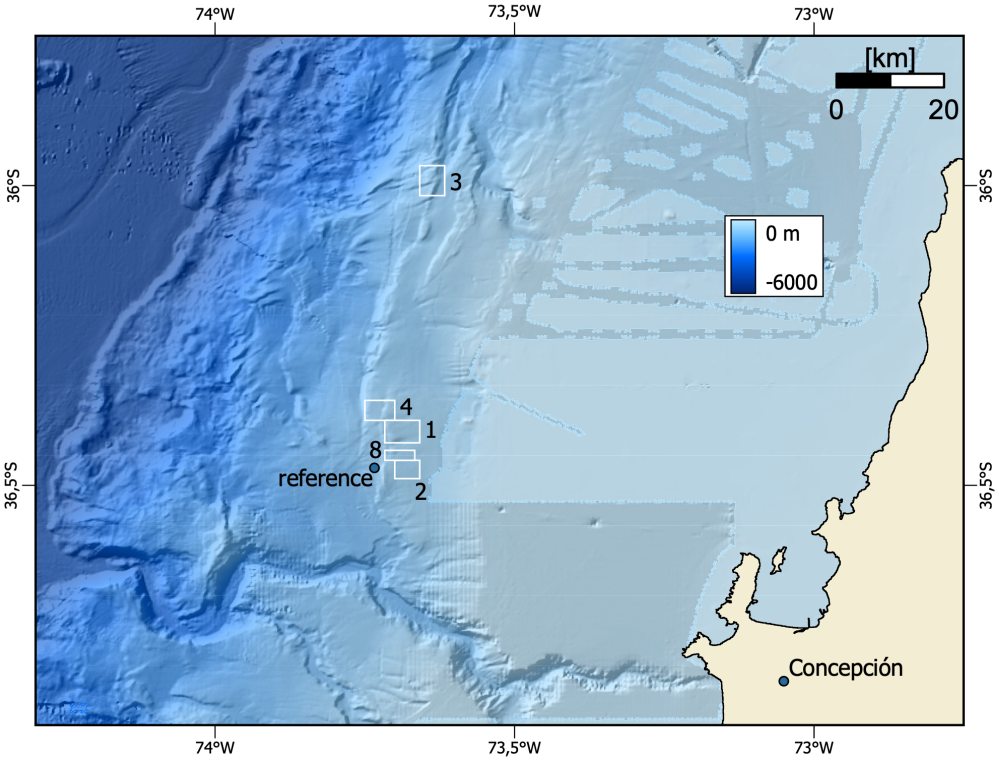


Figure 1. Bathymetric overview map of the CMSA with investigated areas (Boxes and reference site) indicated.

https://doi.org/10.5194/egusphere-2026-6926
Preprint. Discussion started: 20 November 2026
© Author(s) 2026. CC BY 4.0 License.

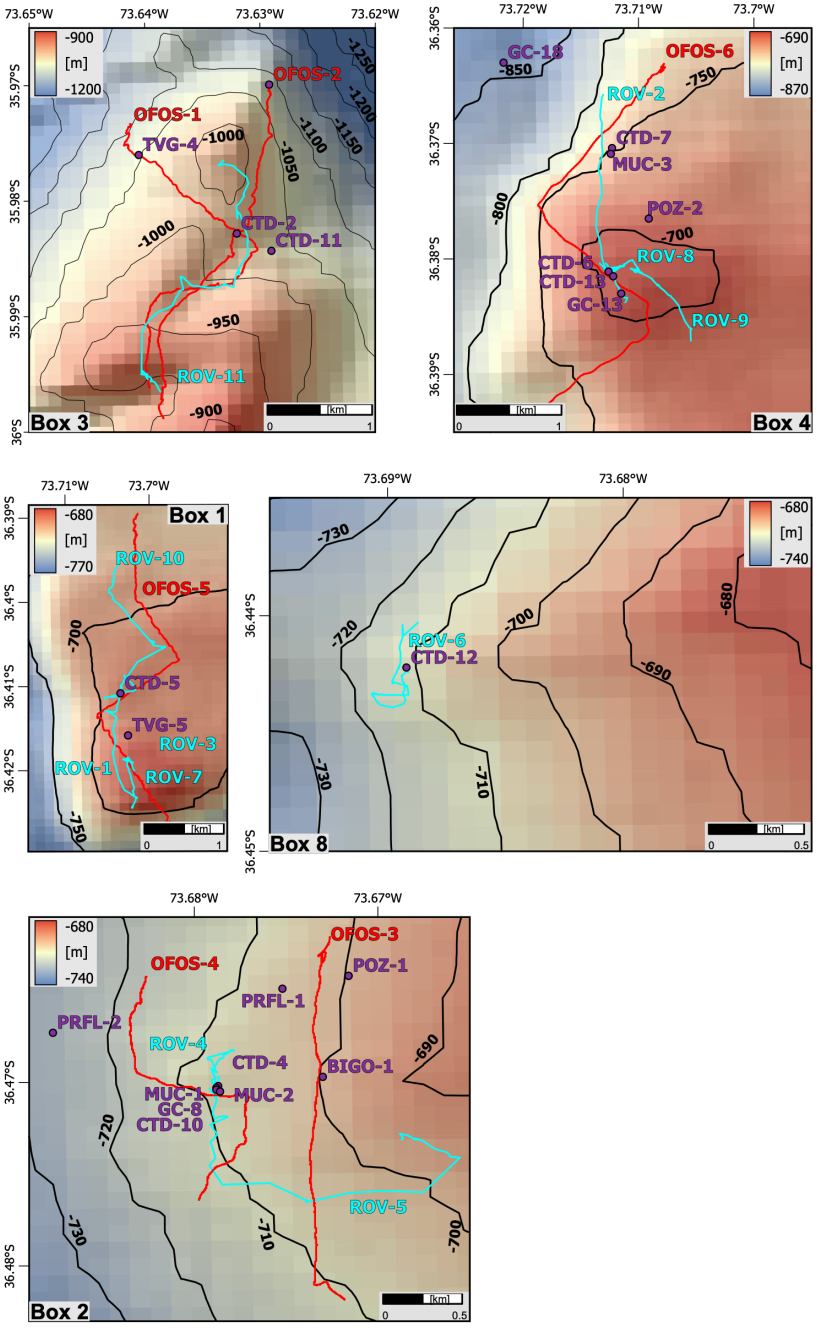


Figure 2. Bathymetric maps of the investigated areas within the CMSA. Box numbers are provided in the corners of the maps. For abbreviations see Materials and Methods.

https://doi.org/10.5194/egusphere-2026-6926
Preprint. Discussion started: 20 November 2026
© Author(s) 2026. CC BY 4.0 License.

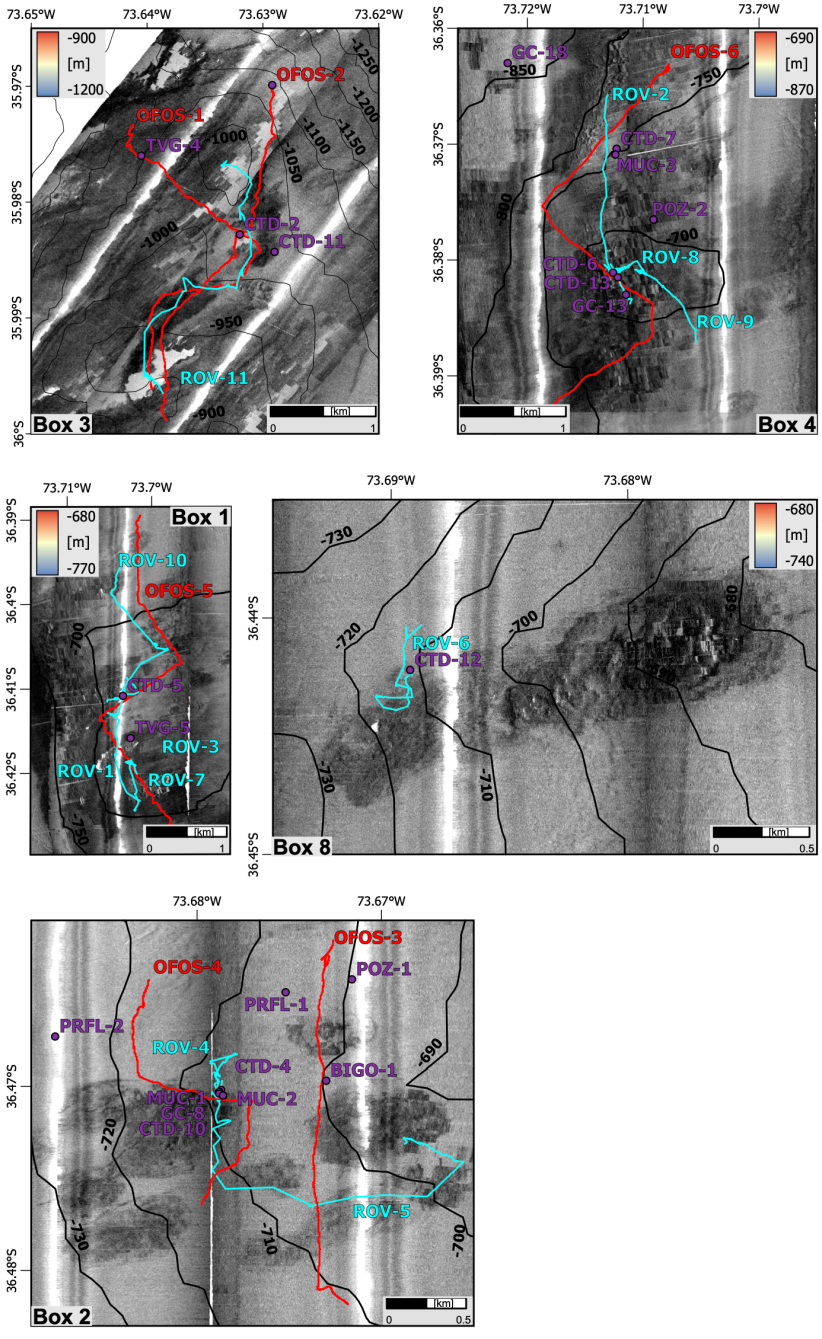


Figure 3. Back scatter maps of the investigated areas within the CMSA. Box numbers are provided in the corners of the maps. For abbreviations see Materials and Methods.

https://doi.org/10.5194/egusphere-2026-6926
Preprint. Discussion started: 20 November 2026
© Author(s) 2026. CC BY 4.0 License.

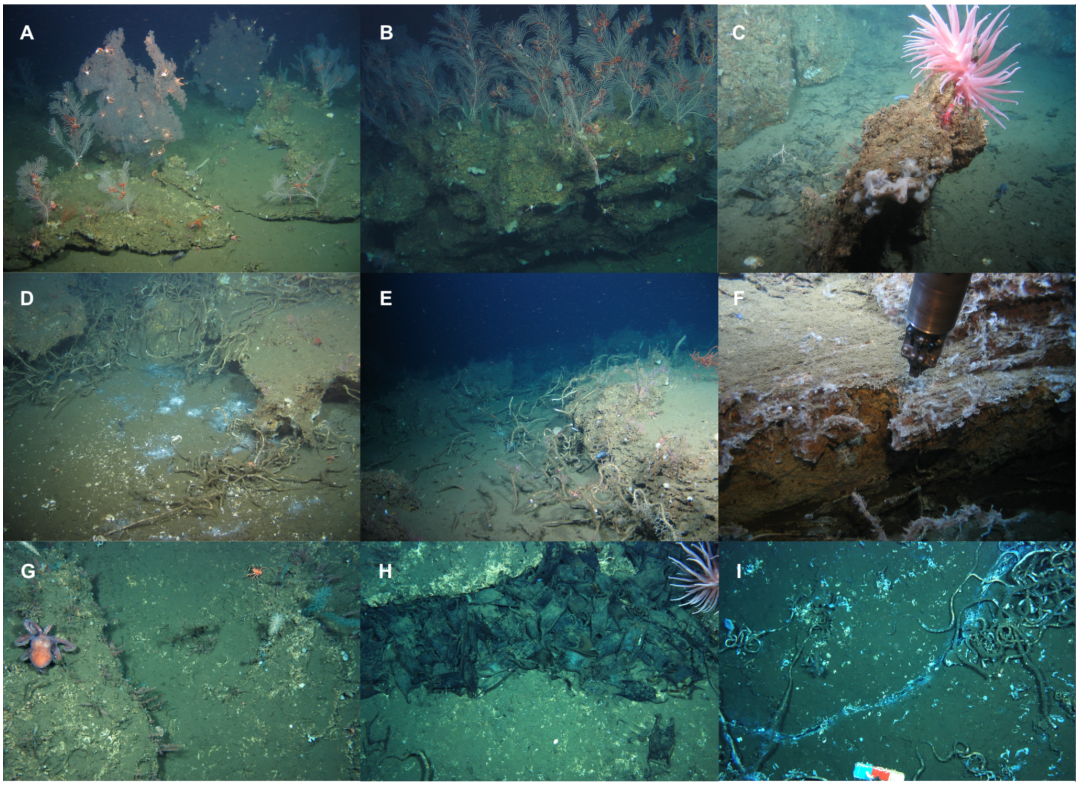


Figure 4. Seafloor habitat characteristics frequently observed in Box-1. (A-F) High-definition photos taken by the remotely operated vehicle (ROV) Kiel 6000. (G-I) Photos taken by the OFOS (Ocean Floor Observation System). OFOS weight (blue/red/white) length 20 cm. Laser distance (red dots) 50 cm. Photo H was previously published in Treude et al. 2011.

https://doi.org/10.5194/egusphere-2026-6926
Preprint. Discussion started: 20 November 2026
© Author(s) 2026. CC BY 4.0 License.

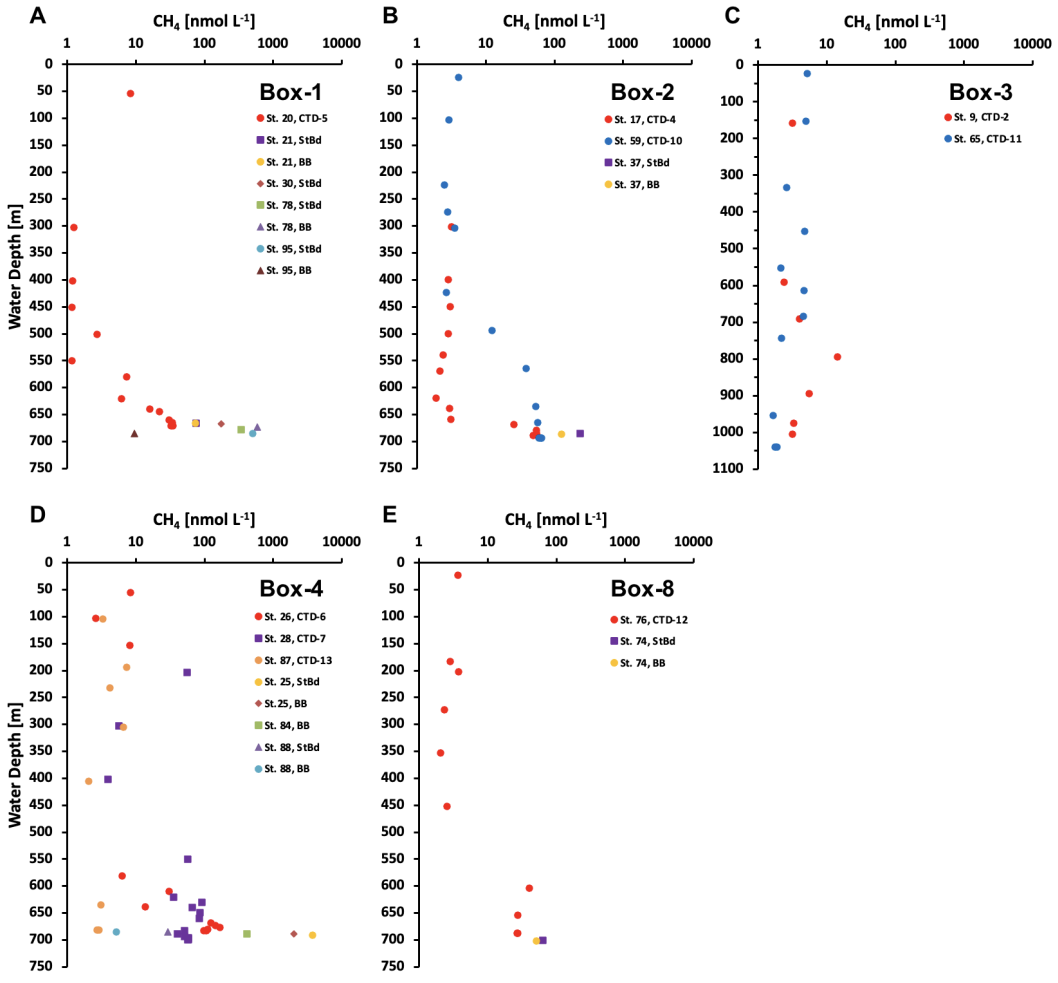


Figure 5. Water column methane concentrations at Box-1 (A), -2 (B), -3 (C), -4 (D), and -8 (E). Note the logarithmic scale of the x-axes (CH_4 concentration) and the different y-axis scale (water depth) for Box-3. CTD = vertical CTD/Rosette casts, StBd (starboard) and BB (portside) are ROV Niskin bottles. For more station details see Table 1.

https://doi.org/10.5194/egusphere-2026-6926
Preprint. Discussion started: 20 November 2026
© Author(s) 2026. CC BY 4.0 License.

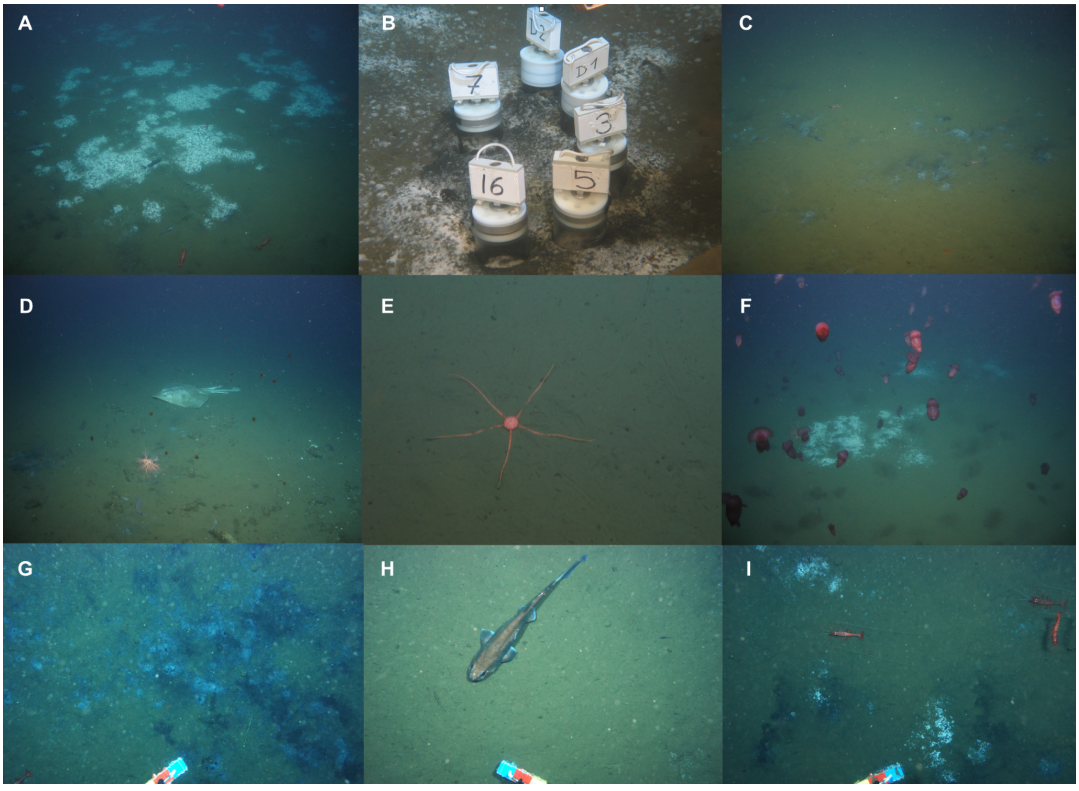


Figure 6. Seafloor habitat characteristics frequently observed in Box-2. (A-F) High-definition photos taken by the remotely operated vehicle (ROV) Kiel 6000. (G-I) Photos taken by the OFOS (Ocean Floor Observation System). OFOS weight (blue/red/white) length 20 cm. Laser distance (red dots) 50 cm.

https://doi.org/10.5194/egusphere-2026-6926
Preprint. Discussion started: 20 November 2026
© Author(s) 2026. CC BY 4.0 License.

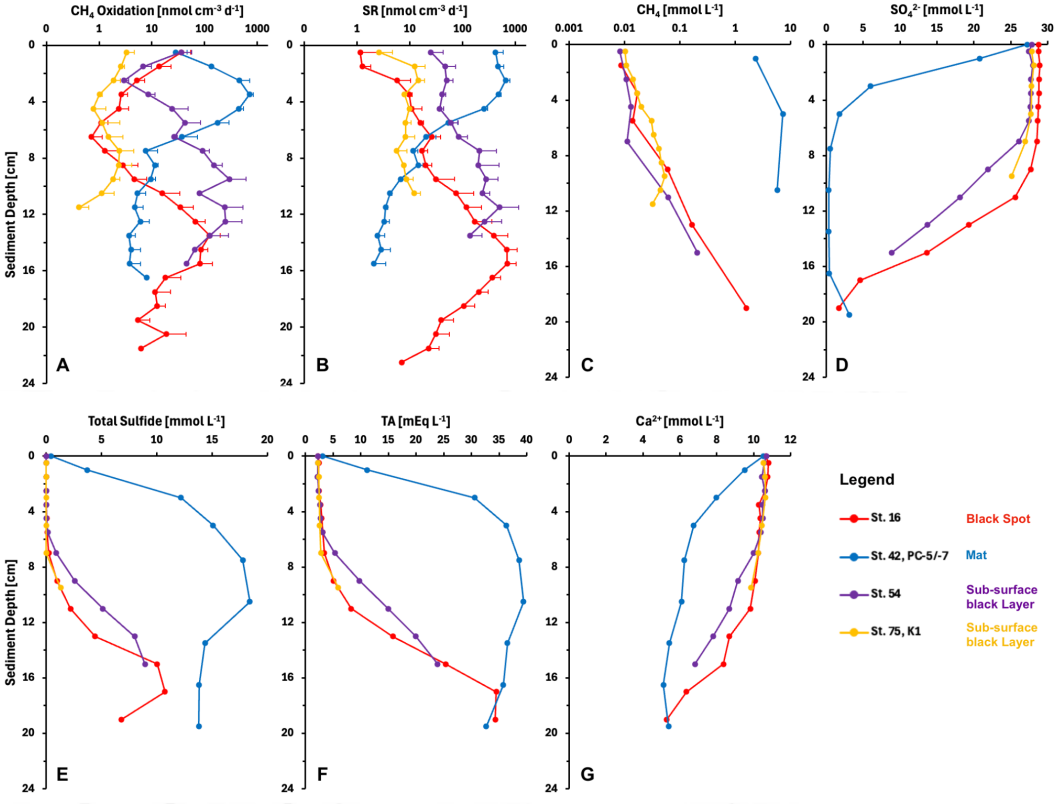


Figure 7. Sediment biogeochemical data from ROV push cores (St. 42), multicorer cores (St. 16 and 54), and BIGO lander chamber cores (St. 75) collected in Box-2: (A) mean methane (CH_4) oxidation rate with positive standard deviation (n = 3), (B) mean sulfate reduction (SR) rate with positive standard deviation (n = 3), (C) sediment methane (CH_4) concentration, (D-G) porewater concentrations of sulfate (SO_4^{2-}), total sulfide, total alkalinity (TA), and calcium ions (Ca^{2+}), respectively. For each instrument deployment, rates (A&B) and geochemical parameters (C-G) were determined in separate replicate cores. For rates, three replicate (R1-3) subcores were collected per parameter from the main core. From the ROV deployment, PC-5 was used for geochemistry and PC-7 for rates. "St." = station, "PC" = push core, "K" = BIGO chamber, "Black Spot" = black sediment surface, "Mat" = sediment covered by sulfur bacteria mat, "Sub-surface black Layer" = black sediment below an oxidized (brown) surface sediment. For more station details see Table 1.

https://doi.org/10.5194/egusphere-2026-6926
Preprint. Discussion started: 20 November 2026
© Author(s) 2026. CC BY 4.0 License.

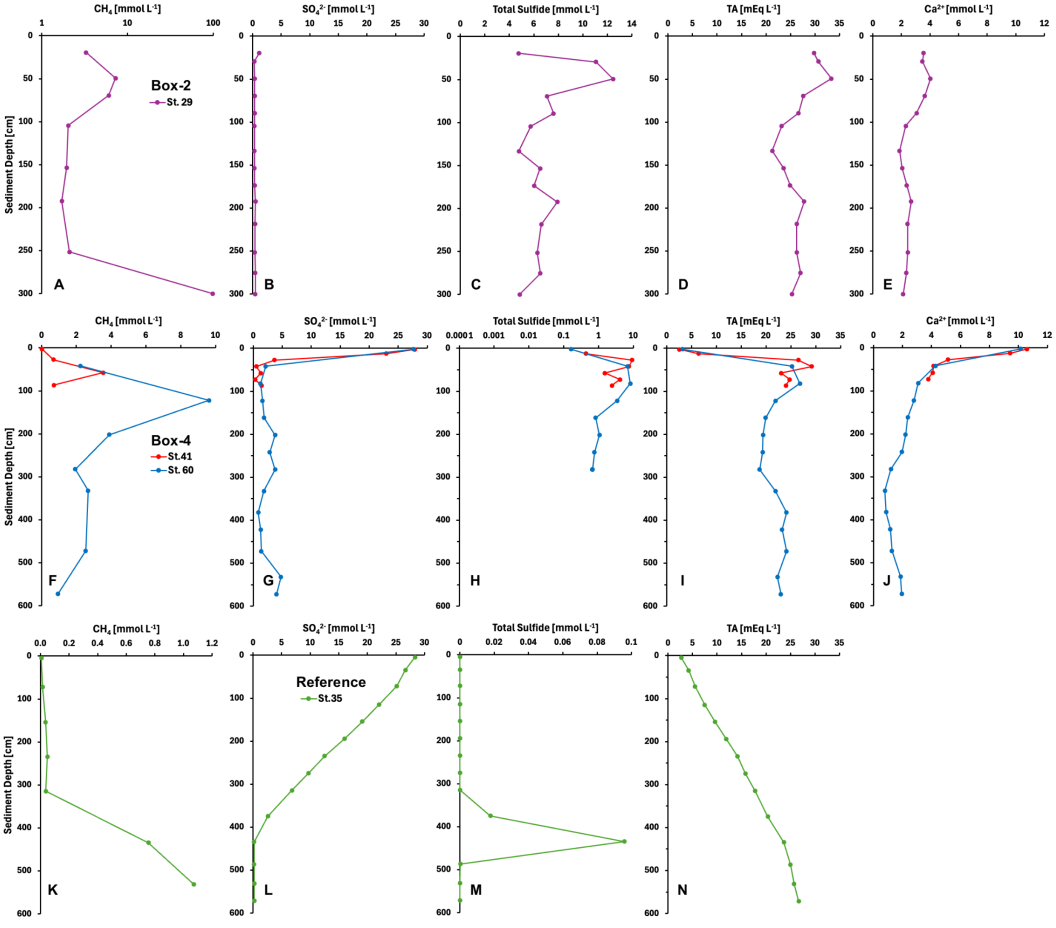


Figure 8. Sediment geochemical data from gravity corers collected at Box-2 (St. 29, A-E), Box-4 (St. 41 and 60; F-J) and the Reference site (St. 35, K-N): (A/F) sediment methane (CH_4) concentration, (B/G/K)) porewater concentrations of sulfate (SO_4^{2-}), (C/H/L) total sullfide, (D/I/M) alkalinity (TA), and (E/J) calcium ions (Ca^{2+}), respectively. Box-4 cores were both taken within the Dead Clam Field. The Reference site had no indications of seepage based on geophysical data. No microbial turnover rates (methane oxidation, sulfate reduction) were determined at any sites. No methane and calcium ion concentrations were determined for the Reference site. For more station details see Table 1.

https://doi.org/10.5194/egusphere-2026-6926
Preprint. Discussion started: 20 November 2026
© Author(s) 2026. CC BY 4.0 License.

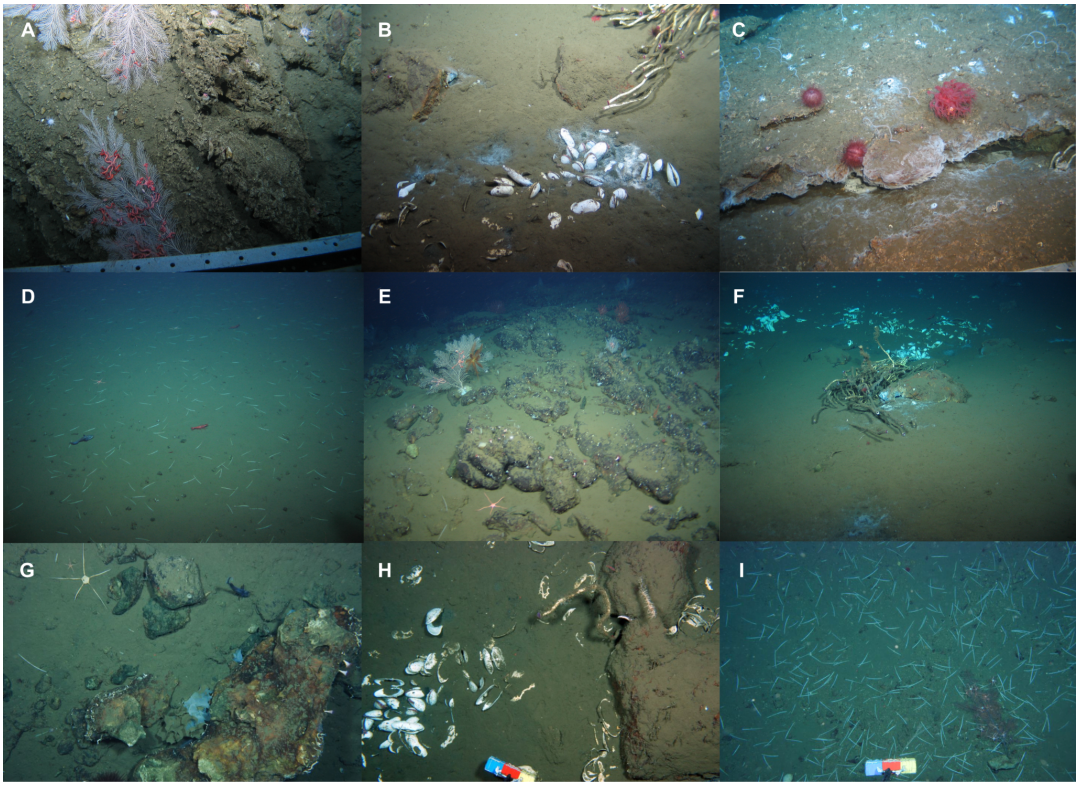


Figure 9. Seafloor habitat characteristics frequently observed in Box-3. (A-F) High-definition photos taken by the remotely operated vehicle (ROV) Kiel 6000. (G-I) Photos taken by the OFOS (Ocean Floor Observation System). OFOS weight (blue/red/white) length 20 cm. Laser distance (red dots) 50 cm.

https://doi.org/10.5194/egusphere-2026-6926
Preprint. Discussion started: 20 November 2026
© Author(s) 2026. CC BY 4.0 License.

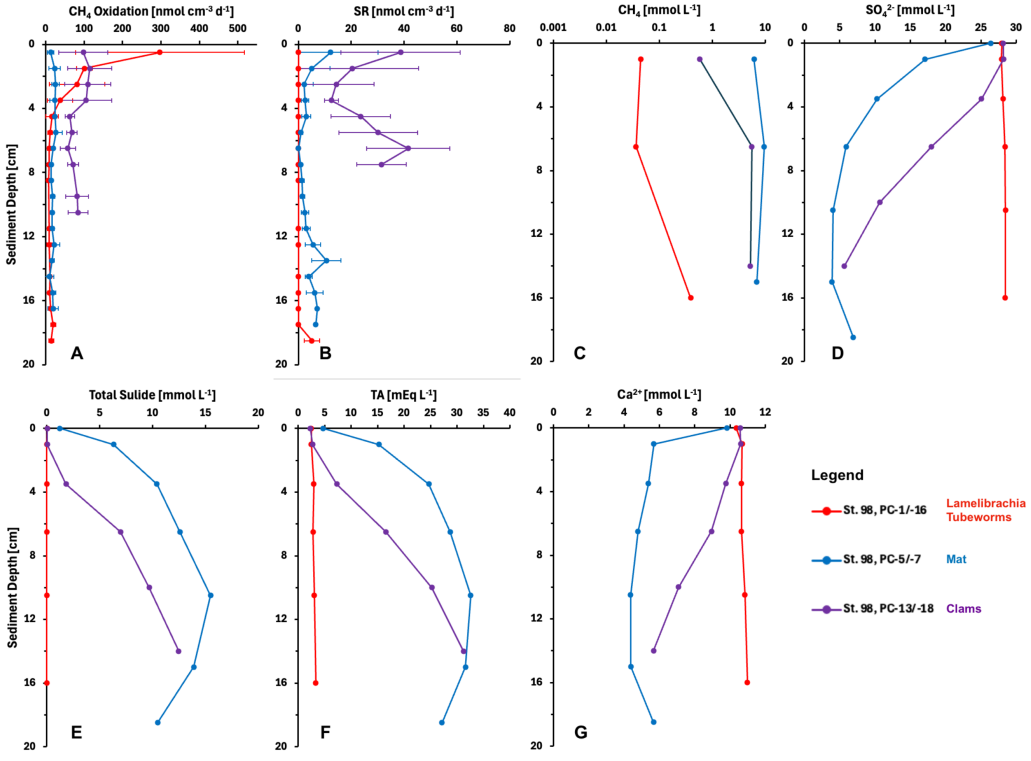


Figure 10. Sediment biogeochemical data from ROV push cores (PC) collected in Box-3: (A) mean methane (CH_4) oxidation rate with standard deviation (n = 3), (B) mean sulfate reduction (SR) rate with standard deviation (n = 3), (C) sediment methane (CH_4) concentration, (D-G) porewater concentrations of sulfate (SO_4^{2-}), total sulfide, total alkalinity (TA), and calcium ions (Ca^{2+}), respectively. At each ROV site, two replicate pushcores were collected for geochemistry (PC-16, -5, -13) and rates (PC-1, -7, 18), respectively. For rates, three replicate (R1-3) subcores were collected per parameter from the main core. Note the different x-axes in (A) and (B) and the logarithmic scale of the x-axis in (C). "Vestiment. Tubeworms" = sediment collected close to tubes of chemosymbiotic *Lamellibrachia* sp. worms, "Mat" = sediment covered by sulfur bacteria mat, "Clams" = sediment with chemosymbiotic clams. For more station details see Table 1.

https://doi.org/10.5194/egusphere-2026-6926
Preprint. Discussion started: 20 November 2026
© Author(s) 2026. CC BY 4.0 License.

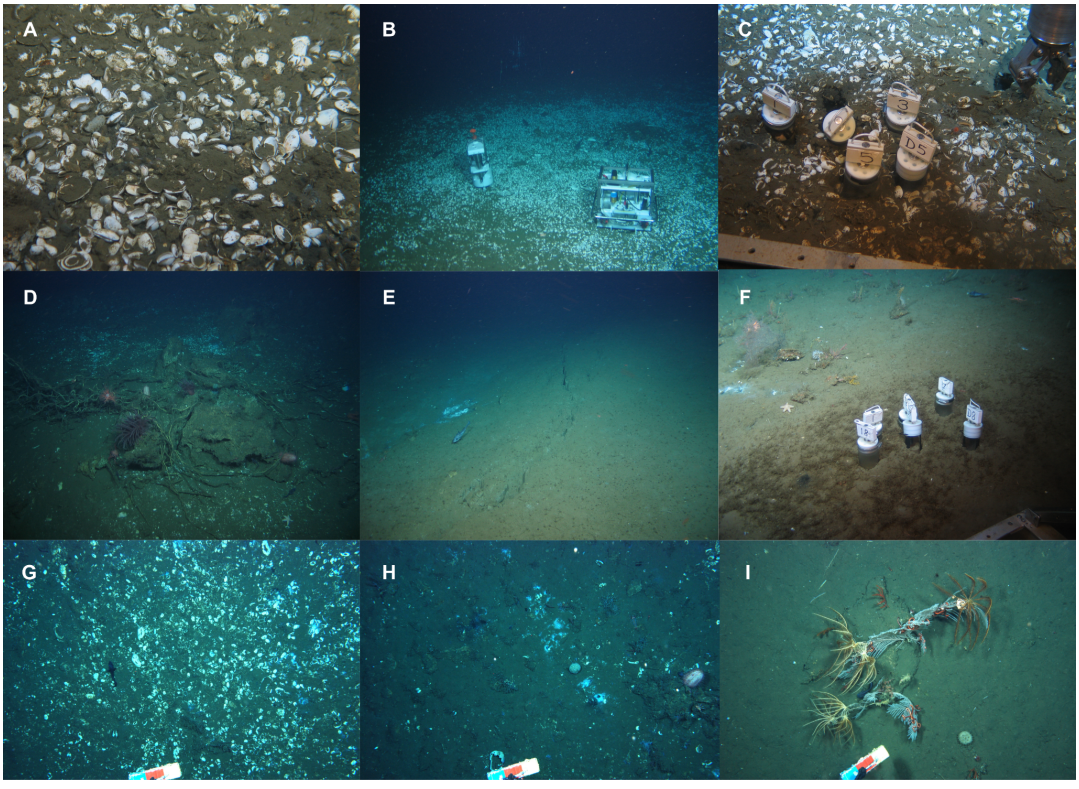


Figure 11. Seafloor habitat characteristics frequently observed in Box-4. (A-F) High-definition photos taken by the remotely operated vehicle (ROV) Kiel 6000. (G-I) Photos taken by the OFOS (Ocean Floor Observation System). OFOS weight (blue/red/white) length 20 cm. Laser distance (red dots) 50 cm.

https://doi.org/10.5194/egusphere-2026-6926
Preprint. Discussion started: 20 November 2026
© Author(s) 2026. CC BY 4.0 License.

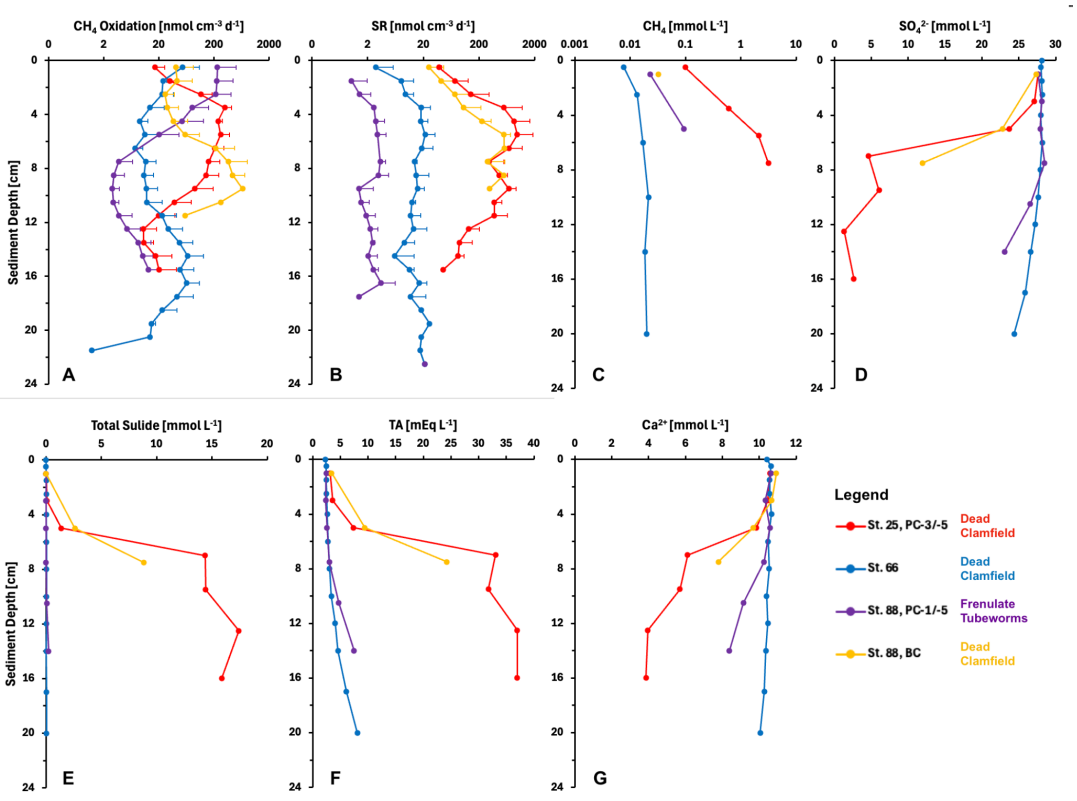


Figure 12. Sediment biogeochemical data from ROV push cores (St. 25 and 28), multicorer cores (St. 66), and benthic chamber cores (St. 88) collected in Box-4: (A) mean methane (CH_4) oxidation rate with positive standard deviation (N = 3), (B) mean sulfate reduction (SR) rate with positive standard deviation (N = 3), (C) sediment methane (CH_4) concentration, (D-G) porewater concentrations of sulfate (SO_4^{2-}), total sulfide, total alkalinity (TA), and calcium ions (Ca^{2+}), respectively. For each instrument deployment, rates (A&B) and geochemical parameters (C-G) were determined in separate replicate cores. At each ROV site, two replicate pushcores were collected for geochemistry (PC-5 and -1) and rates (PC-3 and -5), respectively. For rates, three replicate (R1-3) subcores were collected per parameter from the main core. Note the logarithmic scale of the x-axis in (A-C). "St." = station, "PC" = push core, "BC" = benthic chamber, "Dead Clamfield" = large sediment pit with apparently dead chemosymbiotic clams (open shells), "Frenulate Tubeworms" = sediment collected within a field of chemosymbiotic frenulate tubeworms. For more station details see Table 1.

https://doi.org/10.5194/egusphere-2026-6926
Preprint. Discussion started: 20 November 2026
© Author(s) 2026. CC BY 4.0 License.

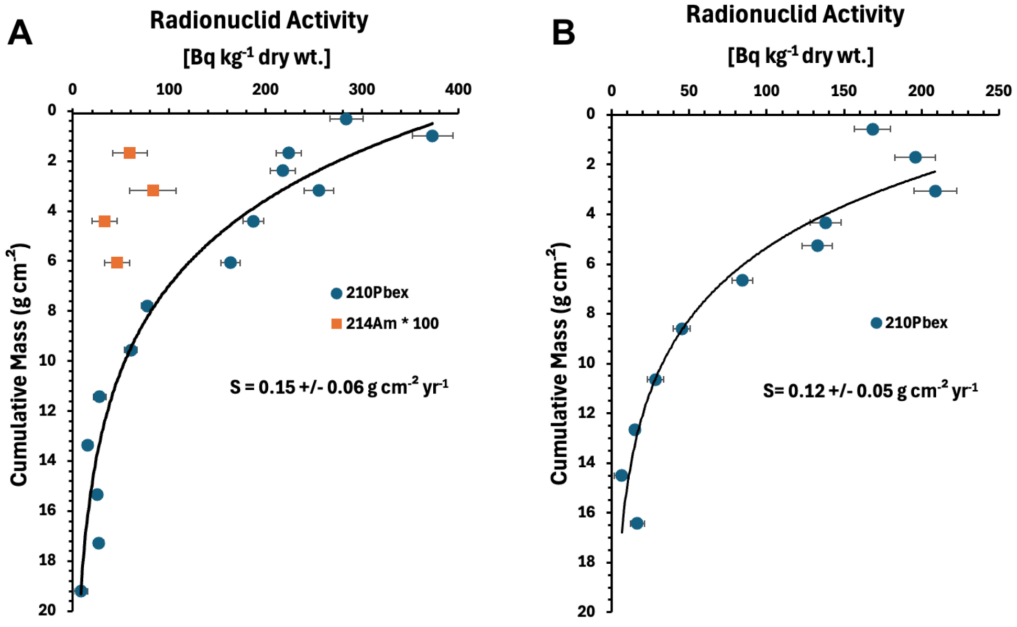


Figure 13. $^{210}Pb_{ex}$ profiles of sediment cores investigated in the *Dead Clam Field* at Box-4 (A: St 66, MUC-3, B: St 25, PC-5) with derived sedimentations rates and ^{241}Am distribution (only A).

https://doi.org/10.5194/egusphere-2026-6926
Preprint. Discussion started: 20 November 2026
© Author(s) 2026. CC BY 4.0 License.

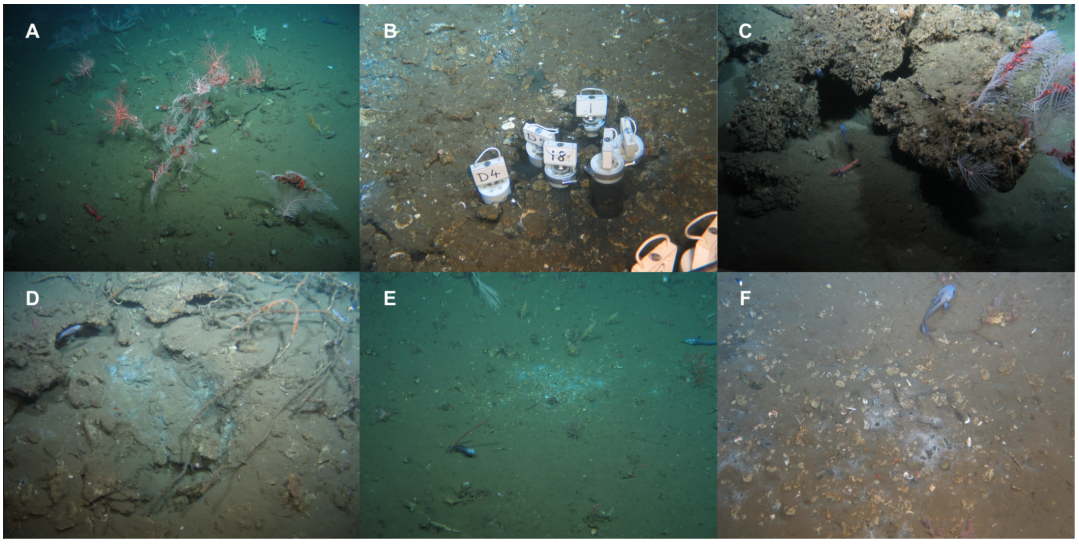


Figure 14. Seafloor habitat characteristics frequently observed in Box-8. High-definition photos taken by the remotely operated vehicle (ROV) Kiel 6000.

https://doi.org/10.5194/egusphere-2026-6926
Preprint. Discussion started: 20 November 2026
© Author(s) 2026. CC BY 4.0 License.

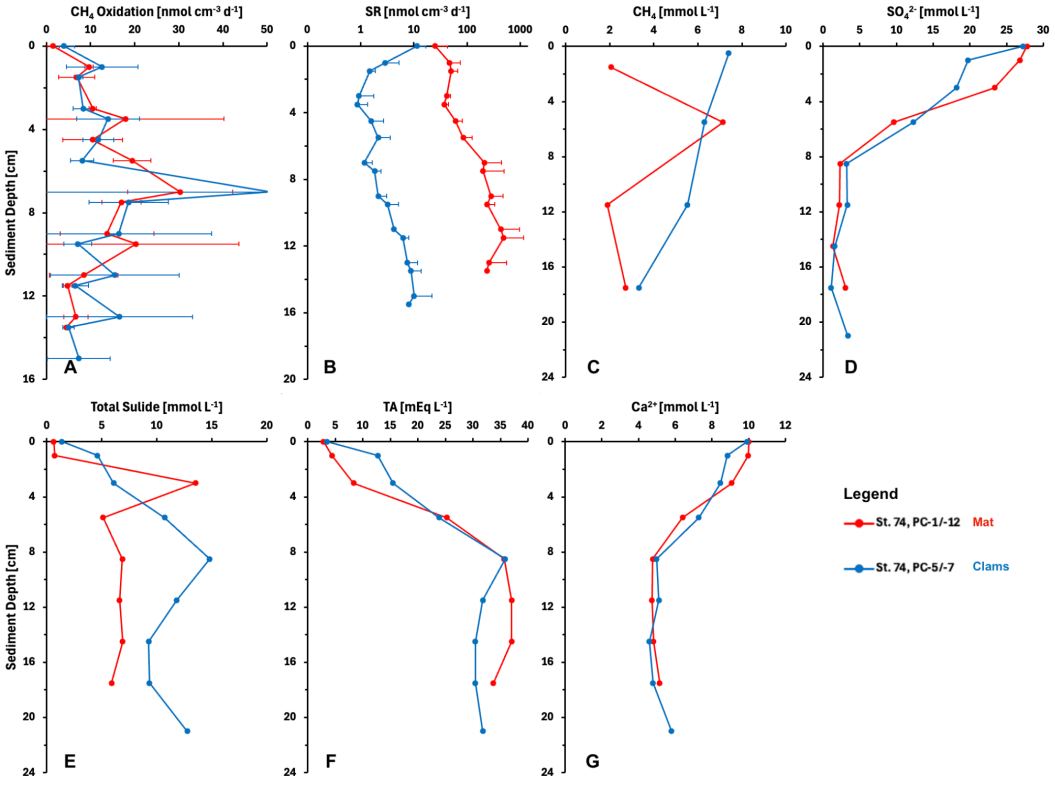


Figure 15. Sediment biogeochemical data from ROV push cores (PC) collected in Box-8: (A) mean methane (CH_4) oxidation rate with standard deviation (N = 3), (B) mean sulfate reduction (SR) rate with positive standard deviation (N = 3), (C) sediment methane (CH_4) concentration, (D-G) porewater concentrations of sulfate (SO_4^{2-}), total sulfide, total alkalinity (TA), and calcium ions (Ca^{2+}), respectively. At each ROV site, two replicate pushcores were collected for geochemistry (PC-12 and -5) and rates (PC-1 and -7), respectively. For rates, three replicate (R1-3) subcores were collected per parameter from the main core. Note the logarithmic scale of the x-axis in (B). "Mat" = sediment covered by sulfur bacteria mat, "Clams" = sediment with chemosymbiotic clams. For more station details see Table 1.

https://doi.org/10.5194/egusphere-2026-6926
Preprint. Discussion started: 20 November 2026
© Author(s) 2026. CC BY 4.0 License.

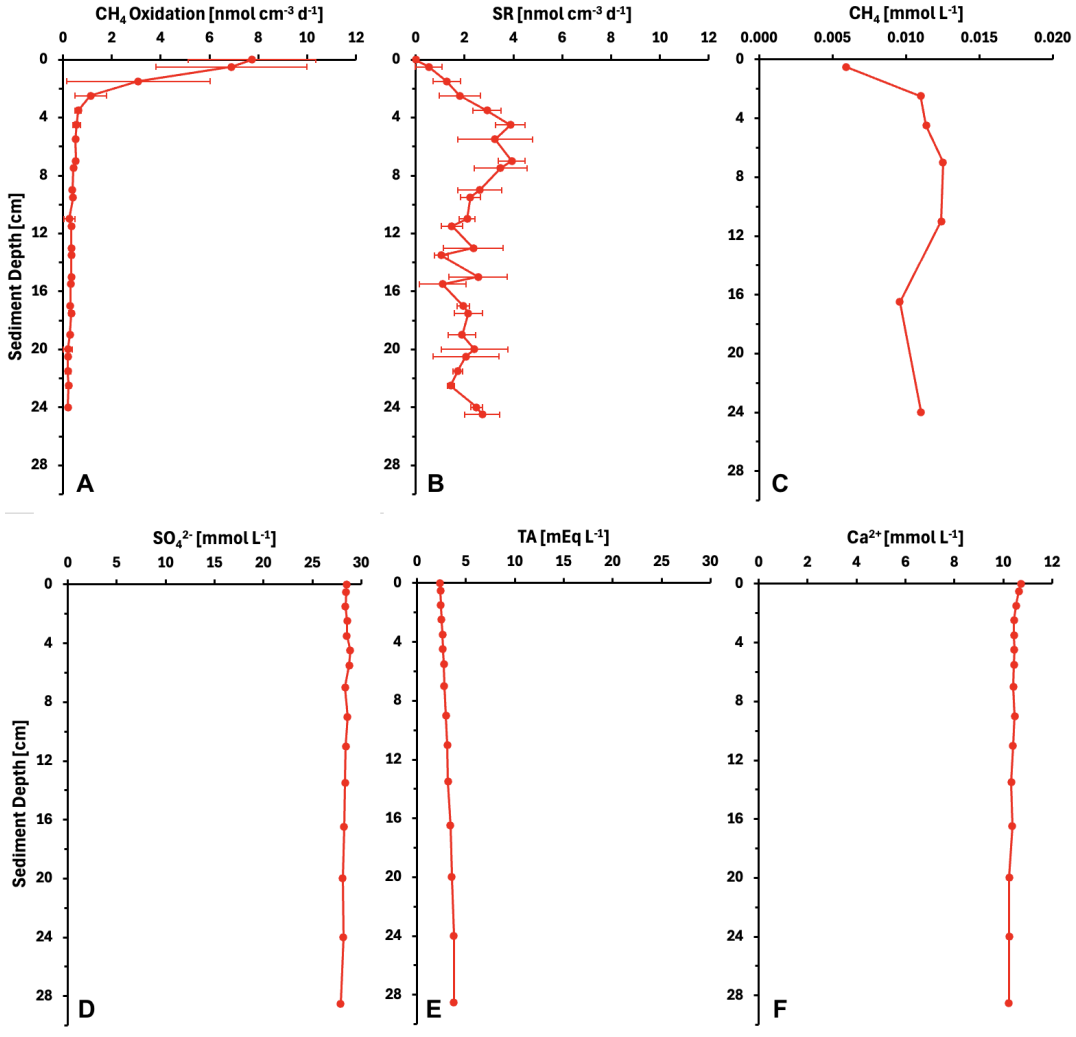


Figure 16. Sediment biogeochemical data from multicorer cores (Station 68) collected at the Reference site: (A) mean methane (CH_4) oxidation rate (n = 3), (B) mean sulfate reduction (SR) rate (n= 3), (C) sediment methane (CH_4) concentration, (D-F) porewater concentrations of sulfate (SO_4^{2-}), total alkalinity (TA), and calcium ions (Ca^{2+}), respectively. Total sulfide was determined but not detected in the porewater. For rates, three replicate subcores were collected per parameter from the main core (circle, square and triangle symbols). The Reference site had no indications of seepage based on geophysical data. For more station details see Table 1.

https://doi.org/10.5194/egusphere-2026-6926
Preprint. Discussion started: 20 November 2026
© Author(s) 2026. CC BY 4.0 License.

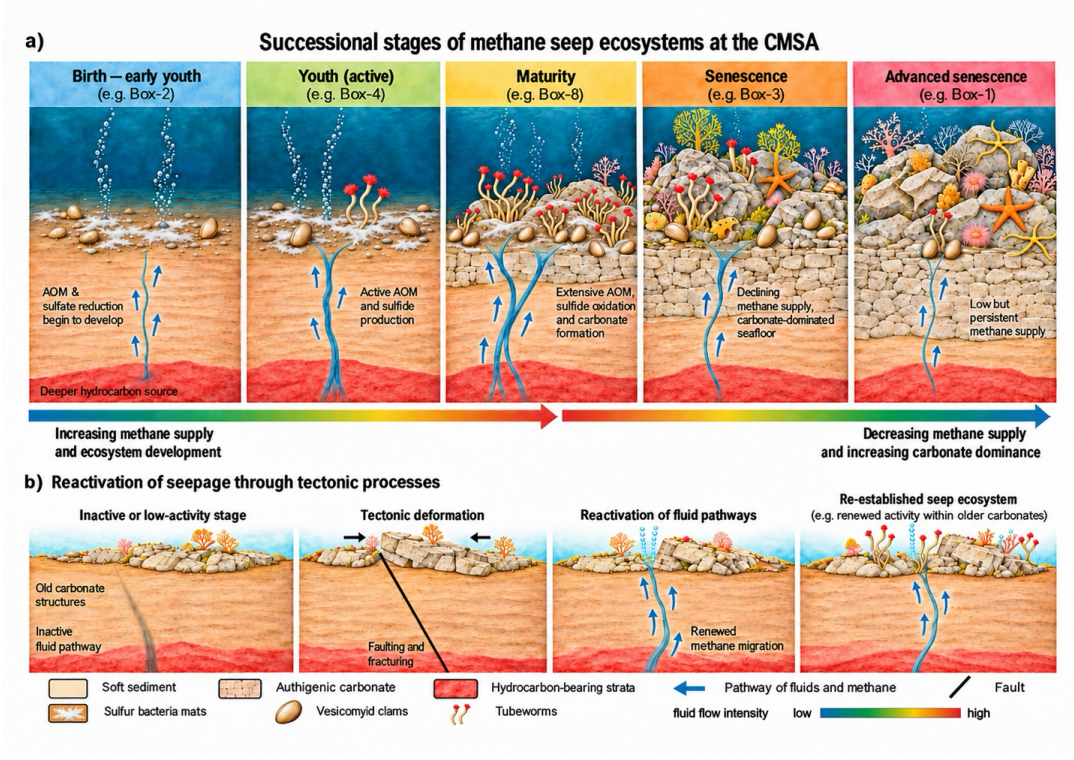


Figure 17 (and Graphical Abstract). Conceptual model of methane seep development and potential tectonic reactivation at the Concepción Methane Seep Area (CMSA) off central Chile. a) Dominant ecological and biogeochemical states represented by the investigated habitats: birth–early youth (Box-2), active youth (Box-4), maturity (Box-8; tentative assignment), senescence (Box-3), and advanced senescence (Box-1), interpreted within the successional framework of Arrázola and Acosta (2024). Increasing methane supply supports anaerobic oxidation of methane (AOM) coupled to sulfate reduction, generating sulfide that sustains sulfur-oxidizing bacterial mats and chemosymbiotic vesicomyid clams and tubeworms. AOM also increases alkalinity, promoting authigenic carbonate precipitation. As methane supply declines or becomes spatially restricted, carbonate structures increasingly dominate the habitat and provide habitat to local fauna such as soft corals, hydroids, sponges, anemones, and echinoderms, while localized seepage sustains remnant chemosynthetic communities. Advanced senescence therefore does not imply complete cessation of seepage. These habitats constitute a spatial mosaic rather than a demonstrated chronological or irreversible sequence; pathway widths indicate conceptual relative transport intensity, not measured fluxes. **b)** Proposed reactivation mechanism in which tectonic deformation, faulting, and fracturing reopen fluid pathways through older seep deposits, enabling renewed methane migration and establishment of seep communities among pre-existing carbonates. This

https://doi.org/10.5194/egusphere-2026-6926
Preprint. Discussion started: 20 November 2026
© Author(s) 2026. CC BY 4.0 License.

mechanism illustrates a potential response to tectonic forcing rather than a demonstrated history of an individual CMSA site. Organisms, carbonate thicknesses, and subsurface structures are schematic and not to scale. The graph was generated using ChatGPT based on prompts provided by the authors.